

Exploring the Mechanome with Optical Tweezers and Single Molecule Fluorescence

by

Ricardo R. Brau

B.S. Mechanical Engineering
Massachusetts Institute of Technology, 2001

M.Eng. Biomedical Engineering
Massachusetts Institute of Technology, 2002

Submitted to the Department of Biological Engineering in
Partial Fulfillment of the Requirements for the Degree of

Doctor of Philosophy in Bioengineering

at the

Massachusetts Institute of Technology

[February 2008]
September 2007

© 2007 Massachusetts Institute of Technology
All rights reserved

Signature of Author

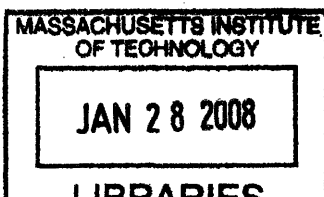
.....
Department of Biological Engineering
September 18, 2007

Certified by

.....
Matthew J. Lang
Keck Assistant Professor of Biological and Mechanical Engineering
Supervisor

Accepted by

.....
Alan J. Grodzinsky
Professor of Electrical, Mechanical, and Biological Engineering
Graduate Program Committee Chair

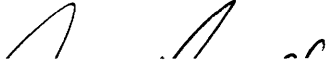


ARCHIVES

This Doctoral Thesis has been examined by the following Thesis Committee:



Tania A. Baker, Ph.D.
E.C. Whitehead Professor of Biology
Howard Hughes Medical Institute Investigator
Massachusetts Institute of Technology



Alan J. Grodzinsky, Ph.D.
Thesis Committee Chair
Professor of Electrical, Mechanical, and Biological Engineering
Massachusetts Institute of Technology

Matthew J. Lang, Ph.D.
Thesis Supervisor
Keck Assistant Professor of Biological and Mechanical Engineering
Massachusetts Institute of Technology



Paul Matsudaira, Ph.D.
Professor of Biology and Biological Engineering
Member, Whitehead Institute for Biomedical Research
Massachusetts Institute of Technology

Robert T. Sauer, Ph.D.
Salvador E. Luria Professor of Biology
Massachusetts Institute of Technology

Exploring the Mechanome with Optical Tweezers and Single Molecule Fluorescence

by

Ricardo R. Brau

Submitted to the Department of Biological Engineering
on September 18, 2007 in Partial Fulfillment of the
Requirements for the Degree of
Doctor of Philosophy in Bioengineering

ABSTRACT

The combination of optical tweezers and single molecule fluorescence into an instrument capable of making combined, coincident measurements adds an observable dimension that allows for the examination of the localized effects of applied forces on biological systems. This technological advance had remained elusive due to the accelerated photobleaching of fluorophores in the presence of the high photon flux of the optical trap. This problem was circumvented by alternately modulating the trapping and fluorescence excitation laser beams, a technique named IOFF. Results show that our solution extends the longevity of Cy3 fluorophores by a factor of 20 without compromising the stiffness of the optical trap. This versatile arrangement can be extended to other fluorophores and was applied to unzip a 15 base pair region of dsDNA and to induce reversible conformational changes in a dsDNA hairpin labeled with a FRET pair.

Next, this work developed an immobilization strategy and two single molecule assays for the ClpX ATPase, an enzyme capable of unfolding substrates that have been targeted for proteolytic degradation. In the first assay, which employs single molecule fluorescence, ClpX was found to unfold and translocate pre-engaged GFP substrates with a time constant of 22 s at saturating ATP concentrations, a rate that is 8-fold faster than bulk measurements clouded by binding and unbinding events. The second assay measured the strength of the ClpX-substrate interaction with optical tweezers. Results show that ClpX holds on to its substrates with forces on the order of 55 pN regardless of the nature and concentration of the nucleotide in solution.

Finally, optical tweezers were used to characterize the rheological properties of methylcellulose and polarized cells, to quantify the mechanical properties of bacteriophage, and to measure the forces generated by a cellular actin spring.

Thesis Supervisor: Matthew J. Lang

Title: Keck Assistant Professor of Mechanical and Biological Engineering

To Lara, Cristina, Mom, and Dad

Acknowledgements

Writing the acknowledgements section is a true trip down memory lane – making it one of the hardest ones to write. As I write these words, I am looking back 10 years to when I first arrived to MIT as a freshman, not knowing what the future had in store for me. As I am readying myself to say goodbye to this wonderful place, I realize how much I have learned and how much more I still have to learn. Nevertheless, I am taking with me memories and friendships that are simply irreplaceable. As such, I would like to extend my gratitude to those individuals that helped make MIT such a wonderful experience for me, with emphasis on the last 5 years of graduate school.

I want to thank my advisor, Matt Lang, for giving me a chance in his laboratory. I knew that I wanted to work in the field of single molecule biophysics from the time I saw him give a talk on kinesin almost 6 years ago. When I joined the lab, I could not tell a PSD from a SAPD, but Matt taught me how to build a high-end instrument with the patience of a saint, particularly when it came to aligning those troublesome AODs. In addition to being a good friend and a fantastic mentor who is always full of innovative ideas, Matt has established a culture of open collaboration and camaraderie in the lab that encouraged me to explore many research interests.

I also want to thank my thesis committee for their support and encouragement. Bob Sauer and Tania Baker were instrumental in the development of the ClpX single molecule assays, without them and their suggestions I do not know where this project would have gone. Paul Matsudaira and Alan Grodzinsky's expertise on the interplay of forces and biology was critical for many aspects of this work. It has been a true pleasure to work with them.

This work would not have been possible without the contribution of many collaborators. In particular, I want to thank Jorge Ferrer and Peter Tarsa for their help in the construction and development of the combined optical tweezers and single molecule fluorescence instrument. I also want to recognize the role of Andreas Martin, who made many of the proteins employed for the ClpX experiments and is one of the most brilliant scientists that I have ever worked with. I was also fortunate enough to work with a number of talented UROPs, and their efforts should not go unnoticed. In particular, I want to thank Phillip Samayoa, who helped develop the optical tweezers assay for ClpX. Throughout the years, I have had the opportunity of engaging in a number of very rewarding collaborations that have taught me much about science and people. As such, I would like to thank the following collaborators: Winston Timp and Dave Quinn for help with the microfluidics setup, Mariya Barch and Yelena Freyzon for developing the molecular force sensor, Judith Su, Jennifer Shin and Barney Tam for giving me the chance to do some cell-based work, Mo Khalil for introducing me to the wonderful world of phage, Mike Murrell for computational advice, and Joey Davis, Jon Kenniston, and Elizabeth Oakes for their help and support with ClpX. Finally, I want to acknowledge the Department of Biological Engineering, the Lemelson Foundation, and the MIT/NIGMS Biotechnology Training Program for financial support.

The current and former members of the Lang Lab, Carlos Castro, Dave Appleyard, Ding Fangyuan, Enrico Ferrari, Jorge Ferrer, Mo Khalil, Olga Parkin, Peter Lee, Peter Tarsa, Valeria Garbin, and all the UROPs, deserve a big thank you for their everyday support. It has been great fun to exchange ideas and argue with you about the really unimportant things in life. I will make sure to come back a couple of times a week so that we can have our lunch outings to Anna's Taqueria or Border India. In addition, I want to acknowledge the rest of the folks who also helped make the 2nd floor of 500 Technology Square my second home (or is it the first?). Coming to work during the past 5 years has been a pleasure because of all of you. I am sorry that I may have tortured many of you with my ice chewing.

I have been incredibly blessed with many great friendships: some have been forged during my time at Cambridge while others find their roots in high school. Even though it would be impossible to list them all here, I want to thank those of you who have stayed true during all this time. Thanks for keeping me grounded and balanced and for reminding me that life is more fun when you spend it with your friends.

To my family, it has been hard being away from you throughout all this years, but I am sure that at some point we will all converge once again. I will never forget the countless "When are you going to finish?" questions and the look on your faces when my response was "years". To my grandmas, I have never met two people who are more independent and free-spirited than you – I can only wish that I become more like you as I get older. To my grandpas, thanks for teaching me to love baseball and dominos and to always express what is on my mind. To my sister Cristina, of whom I couldn't be prouder, thanks for checking in on me from time to time to make sure that I was not living in the lab. To Mom and Dad, I can only imagine the number of sacrifices that you have made so that Cristina and I never lacked anything growing up. I will probably never be able to repay you, but thanks for showing me the value of hard work. Everything that I have ever achieved is simply a reflection of you; I owe you so much.

Last, but definitely not least, I would like to thank my wonderful and beautiful wife Lara. More than anyone, you have shared the graduate student experience with me. You have endured the highs and the lows, the whole emotional journey. I want to thank you for your love, smile, and unconditional support. Thanks for putting up with all those late nights and weekends in the lab and, more importantly, thanks for giving me a reason to go home. I cannot imagine having gone through this journey without you.

RRB

Cambridge, MA
September, 2007

Table of Contents

List of Figures	13
List of Tables	15
Chapter I: Background and Significance	17
Scope: The Mechanome	18
The ClpX ATPase	20
Protein Unfolding and Degradation in vivo	21
ClpX and the ClpXP Protease	22
Substrate Recognition	23
Structure and Function	24
Substrate Denaturation, Translocation, and Degradation.....	26
ATP Binding, Hydrolysis, and Force Generation	29
Optical Tweezers	32
Instrumentation and Physical Principles.....	33
Calibrating an Optical Trap.....	36
Single Molecule Fluorescence	38
Physicochemical Principles	39
Technology.....	42
Chapter II: Interlaced Force-Fluorescence Spectroscopy	45
Introduction	46
Materials and Methods.....	51
Instrument Design	51
Single Molecule Fluorescence	54
dsDNA Unzipping Assay	55
Hairpin Opening and Closing Assay.....	56
Results.....	57
Optimal Modulation Frequency	57
Fluorophore Longevity.....	60
Combined Measurement.....	64
Watching Conformational Changes with FRET	66
Discussion.....	68
Trap Stiffness and Modulation.....	68
Trap-Dependent Photobleaching Reduction	69
Modulation, Optical Tweezers, and Single Molecule Fluorescence.....	70

Chapter III: Using Single Molecule Fluorescence to Probe the ClpX- Substrate Interaction.....	75
Introduction	76
Materials and Methods.....	79
Results	81
Functionality of Biotinylated ClpX.....	81
Single Molecule Fluorescence Assay.....	82
Fluorescence Detection and Longevity	84
Buffer Exchange.....	87
Nucleotide Dependence	89
Discussion.....	94
Chapter IV: Using Optical Tweezers to Probe the ClpX-Substrate Interaction.....	99
Introduction	100
Materials and Methods.....	103
Results	106
Single Molecule Force Spectroscopy Assay	106
Force-Induced Unbinding	109
Rupture Force Distributions and Modeling	111
Discussion.....	119
Chapter V: Passive Microrheology with Optical Tweezers	125
Introduction	126
Instrumentation	129
Results and Discussion.....	129
Stokes Drag and Index of Refraction Considerations.....	129
Theoretical Considerations.....	135
Methylcellulose.....	138
Conclusions	143
Chapter VI: Exploring the Mechanome	147
IOFF Improves Fluorophore Longevity	148
Single M13 Bacteriophage Tethering and Stretching.....	153
Intracellular Mechanical Variances in Polarized Cells.....	158
The Force of an Actin Spring	164
Appendix I: Protocols.....	169
Appendix II: MATLAB Code	201
References	213

List of Figures

Figure 1.1 Crystal structure of the ClpX ATPase from <i>H. pylori</i>	26
Figure 1.2 Model for the degradation of native proteins by the ClpXP protease	29
Figure 1.3 Ray optics depiction of the optical trapping phenomenon.....	35
Figure 1.4 Two-dimensional position calibration of an optically trapped bead	38
Figure 1.5 Sample Jablonski diagram.....	41
Figure 2.1 Optical layout of the instrument combining optical tweezers and single molecule fluorescence	52
Figure 2.2 Effect of modulation on the integrity of an optical trap	60
Figure 2.3 Cy3 single molecule fluorescence	63
Figure 2.4 Combined measurement using the interlaced modulation technique.....	65
Figure 2.5 Watching force-induced conformational changes with FRET.....	67
Figure 3.1 ATPase rates for wild type and biotinylated ClpX hexamers.....	82
Figure 3.2 Single molecule fluorescence assay for ClpX.....	84
Figure 3.3 Detecting individual fluorescence molecules	85
Figure 3.4 Reducing the photobleaching rate of Cy3 labeled substrates immobilized on anti-His antibody coated surfaces.....	87
Figure 3.5 Buffer exchange in a PDMS-based flow cell	89
Figure 3.6 Single molecule fluorescence decay rates for the ClpX-substrate interaction in the presence of ATP _γ S	92
Figure 3.7 Single molecule fluorescence decay rates for the ClpX-substrate interaction in the presence of ATP.....	93
Figure 4.1 Single molecule force spectroscopy assay for ClpX	108
Figure 4.2 Sample ClpX-substrate unbinding curve.....	111

Figure 4.3 Rupture force probability density distributions for the ClpX-substrate interaction	117
Figure 5.1 Viscosity of different water-glycerol mixtures as determined with optical tweezers using the Stokes method	132
Figure 5.2 Index of refraction effects on optical trap stiffness	134
Figure 5.3 Properties of methylcellulose solutions	143
Figure 6.1 Effects of IOFF on the photobleaching decay rate of different fluorophores	152
Figure 6.2 Single M13 bacteriophage stretching.....	156
Figure 6.3 Optical tweezers schematic	161
Figure 6.4 Positioning a magnetic bead with an optical trap on the leading edge of a polarized cell	162
Figure 6.5 Rheological variances in polarized cells	163
Figure 6.6 The acrosome reaction in <i>Limulus</i> sperm	166

List of Tables

Table 1.1 Common single molecule dyes and their photophysical properties	44
Table 3.1 Summary of results for single molecule fluorescence decay rates for the ClpX-substrate interaction.....	93
Table 4.1 p-values for the rupture force and loading rate populations for unbinding events of the ClpX-substrate interaction at different nucleotide conditions	113
Table 4.2 Summary of results for single molecule force spectroscopy measurements of the ClpX-substrate interaction.....	119
Table 5.1 Refractive indices for glycerol and methylcellulose solutions.	134

Chapter I

Background and Significance

Abstract

This thesis is mostly concerned with improving our understanding of the mechanome, the interplay between mechanics and biology, at the single molecule level. In order to do this, we have developed instrument platforms with optical tweezers and single molecule fluorescence capabilities to perform single molecule experimentation. In addition, these two mainstay techniques have been combined into a single functional instrument, called IOFF, capable of exerting forces on biological systems while using fluorescence reporting to gain information about structural or conformational states, as described in Chapter II. Next, we developed two single molecule assays to study the mechanistic behavior of the ClpX ATPase, a molecular motor capable of unfolding other proteins. The first one, described in Chapter III, employs single molecule fluorescence to measure the time of engagement between ClpX and its substrates. The second assay, described in Chapter IV, uses optical tweezers to measure the forces governing the interactions between ClpX and its substrates. Chapter V communicates the use of optical tweezers instrumentation to measure the rheological properties of methylcellulose, a thickening agent commonly used to slow down the dynamics of

biological systems. Finally, Chapter VI presents novel applications for the developed instrument platforms. First, however, this chapter introduces the ClpX ATPase as well as single molecule fluorescence and optical tweezers technology.

Scope: The Mechanome

The bulk of this thesis is concerned with the application and measurement of forces in biological systems at the molecular scale. As such, this work seeks to make a contribution to our understanding of the mechanome. Stemming from the fields of genomics, proteomics, and glycomics, mechanomics aims to understand the role that mechanical forces play in biological systems. It has long been known that living systems can exert forces on their environment. This is most clear at the organism level, where humans can use their muscles to move objects. Not as obvious, though, is the fact that organisms can also react to external loads. The best of example of this is the role that gravity plays on human physiology. Bones evolved to constantly be under a gravitational load. If such a load is removed, as is the case for astronauts spending much time in space, their bone mass is usually reduced. Thus, not only can organisms exert loads, but they are affected by them as well. This interplay between forces and biology is the very definition of the mechanome.

To further illustrate the importance of mechanics in biology, let's consider the role that forces play in cellular physiology. Many cells such as fibroblasts can exert forces on substrates by contracting their bodies (Freyman, et al, 2001). This process is mostly driven by acto-myosin interactions and plays important roles in migration and wound

healing, among others (Alberts, 2002). Cells are also capable of sensing external loads that are being applied on them. Furthermore, such loads are critical for their health, as evidenced by the atrophy and loss of mass in infrequently used muscles. The mechanisms by which cells convert mechanical stimuli into biochemical signals that affect their physiology are collectively known as mechanotransduction. This process is at the core of the mechanome and has been recently captured by the activation of the Src kinase in HUVEC cells in response to forces exerted on their membranes (Wang, et al, 2005). Mechanotransduction has also been observed in the alignment of endothelial cells parallel external shear stresses (Alberts, 2002), which can trigger the activation of integrin receptors as well (Tzima, et al, 2001). It is believed that external forces are capable of altering the shape of membrane-bound proteins like channels or receptors, leaving them in conformational states that are more or less likely to bind extracellular ligands. Once these ligands bind, they can trigger biochemical signal cascades that ultimately affect the physiology of the cell (Alberts, 2002). Thus, cells are in constant interaction with their environments, and are capable of using force as a feedback mechanism.

Perhaps the role that mechanics play in biology can be most appreciated at the nanometer length scale. It is in this realm that molecular motors are found and conformational changes regulate many protein interactions and functions. Molecular motors are, almost by definition, mechanical entities. One only needs to picture how kinesin walks along a microtubule track while hauling a cargo vesicle to visualize the importance that mechanics play on this system. First, there is the coordination of the

kinesin heads in a much debated arrangement that ultimately leads to overall movement and processivity (Block, 2007). Second, there is the consumption of energy and its conversion from potential energy stored in ATP into local conformational changes that manifest themselves in the power strokes that ultimately generate motion (Block, 2007). Finally, there is the drag experienced by the cargo vesicle, which works against the reaction coordinate of the enzyme. Even though this mechanochemical coupling is not well understood, it is clear that it is cyclical, driven by ATP, and ubiquitous in all molecular motor systems studied to date, which include the well-studied kinesin, myosin, and dynein family of motors. In addition, ATP-dependent mechanics at the molecular length scale have been observed for RNA polymerase (Abbondanzieri, et al, 2005a), DNA helicase (Dumont, et al, 2006), and the ϕ 29 bacteriophage (Smith, et al, 2001), among others. This wide range of enzymes, each with its own distinct biological function, exemplify the importance of forces and mechanics in molecular biology.

The ClpX ATPase

Members of the AAA+ (ATPases associated with diverse cellular activities plus) superfamily of proteins play crucial roles in nearly every major cellular process (Alberts, 1998; Neuwald, et al, 1999). These ATPases can convert chemical energy into mechanical work that is usually manifested as biological function. Cellular activities such as proteolysis, protein folding, membrane trafficking, cytoskeletal regulation, organelle biogenesis, DNA replication, intracellular motility, differentiation, mitosis, and many others are driven by protein domain or subdomain conformational changes resulting from the hydrolysis of ATP (Dougan, et al, 2002; Vale, 2000). However, very little is

understood about the principles that govern this mechanochemical coupling. Improved understanding of this process could lead to the design and development of highly efficient biological machines and cures for disorders such as Parkinson's disease and ciliary dyskinesia (Ogura and Wilkinson, 2001; Weibezahn, et al, 2004), among others. This section will introduce a bacterial ATPase, ClpX, and will review the current literature related to the mechanisms by which it interacts with its substrates.

Protein Unfolding and Degradation in vivo

Cellular homeostasis and optimal metabolic activities inside cells are maintained by a series of tightly regulated and controlled processes that can unfold proteins, dismantle protein multimers, and solubilize aggregates (Gottesman, et al, 1997; Squires and Squires, 1992). Protein integrity is commonly compromised during periods of stress, such as exposure to high temperatures or excessive protein synthesis (Gottesman, 1996). In addition, abnormal and non-functional proteins may also arise due to spontaneous denaturation, biosynthetic errors, inadvertent aggregation, and accumulative mutations (Porankiewicz, et al, 1999). Many proteins with compromised integrities are degraded by members of the Clp/Hsp100 group of chaperones, an AAA+ ATPase subfamily, in both eukaryotes and prokaryotes. Protein degradation is achieved by proteases capable of cleaving the bonds of targeted proteins. In bacteria, many of these proteases have been shown to be composed of two independent components, an ATPase and peptidase, that when bound together possess proteolytic activity (Schirmer, et al, 1996). The ATPase is responsible for unfolding the targeted protein and that the peptidase performs the actual degradation. The peptidase, however,

operates in an energy independent manner and will only degrade small linear polypeptides in the absence of the ATPase (Woo, et al, 1989). Thus, it relies heavily on the ATPase's unfolding abilities to play its part (Feng and Gierasch, 1998).

A particular ATPase, ClpX, has been shown to work in tandem with the peptidase ClpP to form the cytosolic protease ClpXP. Even though ClpX has been the subject of much experimentation at the ensemble level, fundamental questions about its mechanism of action remain unanswered. Preliminary results suggest that ClpX may unfold proteins by applying mechanical forces on its substrate. However, evidence of this has not been directly observed. It is believed that experiments at the single molecule level using the sensitivity of optical tweezers and single molecule fluorescence can help elucidate some of the mysteries surrounding ClpX.

ClpX and the ClpXP Protease

ClpX was first discovered in 1993 in an attempt to identify all proteases capable of degrading the bacteriophage λ O-DNA replication protein in *Escherichia coli* (*E. coli*) (Wojtkowiak, et al, 1993). The discovery of the ClpXP protease was somewhat controversial because the peptidase ClpP had already been implicated in the ClpAP protease. Further studies revealed that both the ClpA and ClpX ATPases are capable of binding ClpP to form a particular protease (Gottesman, et al, 1993). As mentioned above, ClpP cannot degrade proteins on its own; therefore, it is believed that it is the role of its partner ATPase to selectively bind substrates and prepare them for degradation. This hypothesis received recent support when electron microscopy

revealed ClpAP and ClpXP proteases to be composed of ClpP and either ATPase stacked on top or below of it (Ortega, et al, 2004). Other studies were able to visualize that the translocation of substrates through the ClpXP protease starts at ClpX and ends in ClpP (Ortega, et al, 2000). The same series of studies showed that ClpP can bind ATPases in a 1:2 stoichiometry independently of the nature of the ATPase. Both ClpA and ClpX can selectively bind to different substrates, suggesting that the roles of these Clp (caseinolytic proteases) ATPases in protein degradation processes are complementary rather than competitive. Until recently, the number of ClpX specific substrates, besides λ O, was limited to four additional phage or plasmid proteins and three E. coli proteins (Flynn, et al, 2003; Gottesman, 1996).

Substrate Recognition

A proteomic analysis of more than 50 E. coli transcription factors, metabolic enzymes, and proteins involved in the starvation and oxidative stress responses revealed that ClpX can specifically interact with at least 5 different motifs (Flynn, et al, 2003). Three of these recognition sequences are located in the N-terminus of proteins and the other two are located in the C-terminus. One of these latter sequences is the well known *ssrA* tag, which is cotranslationally added to the C-terminal of proteins in stalled ribosomes (Keiler, et al, 1996). This eleven amino acid sequence, NH₂-AANDENYALAA-COOH (in one-letter amino acid designations), is encoded by a small metabolically stable RNA known as 10Sa RNA. Disruption of the gene encoding the 10Sa RNA does not result in *ssrA* C-terminal modifications of proteins and can alter the growth kinetics of cells (Oh

and Apirion, 1991; Tu, et al, 1995). It seems that the *ssrA* tagging system is critical for preserving protein integrity inside cells.

Structure and Function

A functional ClpX protein is actually a hexamer of 6 ClpX monomers whose oligomerization is facilitated by nucleotide binding. ClpX monomers have a molecular weight of 45 kDa and are composed of an N-terminus ATPase domain and a C-terminus SSD (sensor and substrate discrimination) domain (Ogura and Wilkinson, 2001; Wojtkowiak, et al, 1993). The ATPase domain is characterized by the traditional Walker A and B motifs capable of binding and hydrolyzing ATP (Neuwald, et al, 1999; Walker, et al, 1982). Interestingly, ATP can only be bound by hexameric ClpX as the nucleotide binding site is located at the interface between two adjacent ClpX subunits. In addition, ClpX monomers contain a hydrophobic tripeptide sequence, IGF, that is responsible for binding ClpX to ClpP (Kim, et al, 2001). ClpX from *E. coli* also contains a Cys cluster domain that is known to interact with the SspB adaptor protein, which facilitates the delivery of substrates to the enzyme (Kim and Kim, 2003).

Attempts at crystallizing ClpX proteins from various bacteria resulted in the crystal structure of ClpX from *Helicobacter pylori* (*H. pylori*) (Figure 1.1). ClpX hexamers resemble a donut with outside and inside diameters of approximately 140 and 30 Å, respectively, and a thickness of about 70 Å (Kim and Kim, 2003; Singh, et al, 2001). Loops containing the hydrophobic tripeptide IGF, which mediates binding to ClpP, can be seen coming out of the ring-like structure, parallel to the its main axis. These loops

help align the main axis of ClpX with that of ClpP, a multimeric protein itself resembling two rings stacked against each other, and have been implicated in the regulation of the communication between ClpX and ClpP (Joshi, et al, 2004). Structurally, it seems that polypeptides denatured by ClpX are fed axially into the ClpP cavity where they are ultimately degraded. It is believed that the amino acids lining up ClpX's central pore are responsible for the denaturation and translocation of substrates. Mutational substitutions of these amino acids have led to ClpXP proteases with severe defects in the degradation of *ssrA*-tagged substrates (Siddiqui, et al, 2004). It is plausible that these amino acids are responsible for engaging *ssrA*-tagged substrates and pulling on them by undergoing conformational changes leading to power strokes upon the hydrolysis of ATP. Mutations in the RKH loops of ClpX, which line around the ClpX pore and can be found on the ClpX face opposite to the IGF loops where ClpP docks, can result in a 100-fold reduction in its affinity for *ssrA*-tagged substrates (Farrell, et al, 2007). Interestingly, the same mutation resulted in a 3-fold increase in specificity for λ O-tagged substrates (Farrell, et al, 2007). These results highlight the complicated machinery by which ClpX engages its substrates.



Figure 1.1 Crystal structure of the ClpX ATPase from *H. pylori*. (A) Ribbon diagram of the crystal structure (PDB code 1UM8) of a ClpX monomer reveals the C-terminal SSD domain (green), the N-terminus ATPase domain (blue), and the IGF loop (red, stick model). The ATP binding site is highlighted by the presence of an ADP molecule (magenta, stick model). (B) Ribbon diagram of a ClpX hexamer reconstruction. The same color scheme used for the monomer in A is used. The IGF loops of all the monomers (red) are aligned such that they come out of the page. The N and C terminus of a single monomer are highlighted. Crystal structure representations were adapted from Kim and Kim, 2003.

Substrate Denaturation, Translocation, and Degradation

The discovery of the *ssrA* tag allows for the possibility of transforming proteins originally orthogonal to ClpX into actual substrates. This has facilitated much experimentation involving ClpX. A particular protein that has been appropriately modified at its C-terminal and extensively used to study ClpX is the green fluorescent protein (GFP). Ensemble experiments using GFP have been very popular because the fluorescence emitted by the substrate can be easily tracked as a function of time and related to the

properties of ClpX. Experiments in which ClpX was added to a solution of *ssrA*-GFP and ATP were able to see the fluorescent counts of the solution decrease exponentially as a function of time (Singh, et al, 2000). Loss of function (fluorescence) is typically experienced when GFP molecules are unfolded or degraded, as would be expected in the presence of a protease like ClpXP. Interestingly, fluorescence counts from the *ssrA*-GFP solution did not reach undetectable limits in the presence of ClpX (concentration of ClpX was lower than that of *ssrA*-GFP). Instead, the fluorescence readout decreased exponentially until reaching a plateau whose value was dependent on the amount of ClpX added to the solution. Since GFP can refold spontaneously once it has been unfolded, these results suggests that ClpX is engaged in a cycle in which it binds *ssrA* tagged GFP, unfolds it (loss of fluorescence), and finally releases the unfolded GFP polypeptide. This cycle is disrupted in the presence of ClpP or in the presence of a GroEL trap (Singh, et al, 2000). In these cases, fluorescent counts exponentially decrease to baseline levels and no recovery is observed. These results confirm the chaperone activity of ClpX and highlight its functional independence from ClpP. It is worth noting, however, that *ssrA*-GFP seems to be denatured faster by ClpX in the presence of an inactive ClpP mutant than in its absence (Singh, et al, 2000).

Other proteins that have been studied using the *ssrA*-tagging methodology include the P22 Arc repressor, the I27 domain of titin, and RNase-H* (Burton, et al, 2001; Kenniston, et al, 2003; Kenniston, et al, 2004). Of these, the I27 domain of titin (referred to from now on as I27) is the most interesting to us because it has been expressed and purified in folded and unfolded stable states and its unfolding has been mechanically

characterized with atomic force microscopy (AFM) and molecular dynamic simulations (Fowler, et al, 2002; Rief, et al, 1997). In addition, folded and unfolded I27 has been degraded by ClpXP (Kenniston, et al, 2003). Results have revealed that ClpXP binds both folded and unfolded ssrA-tagged I27 with an affinity of about 1 μM . Similar affinity values have been reported for ssrA-tagged GFP, P22 Arc, and RNase-H* (Burton, et al, 2001; Kenniston, et al, 2004; Kim, et al, 2000). These results suggest that the interaction between ClpXP and its ssrA-tagged substrates is independent of the nature of the substrate.

The same set of experiments revealed that each ClpXP molecule can degrade the unfolded domains much faster than the folded ones, at rates of 4 and 0.25 min^{-1} , respectively. The difference in the rate of folded and unfolded I27 domains that are degraded by ClpXP suggests that the mechanical denaturation of the folded domains is a rate-limiting step in the degradation reaction. Several reports support a model for protein denaturation by ClpX in which the global thermodynamic stability of the substrate plays a very small role in resisting unfolding (Burton, et al, 2001; Kenniston, et al, 2003; Kenniston, et al, 2004). Instead, it has been suggested that the local thermodynamic stability of the domains proximal to the C-terminal ssrA tag determine a substrate's ability to resist denaturation. Once these local folds are unfolded, the overall thermodynamic energy barrier resisting denaturation is dramatically reduced and the rest of the protein is exposed (Kenniston, et al, 2003). A current model for substrate denaturation and proteolysis by ClpXP proposes that the first step in the reaction is substrate recognition and binding (Figure 1.2). This is followed by the mechanical

denaturation of the substrate. Finally, the unfolded polypeptide is translocated across the ClpX pore and into the ClpP proteolytic cavity (Kenniston, et al, 2003). The remaining degradation and peptide fragment-release steps are usually ignored or compounded into the translocation kinetics. A reason for this is that ClpP is an ATP independent serine protease and its proteolytic steps have been reported to be much faster than unfolding and translocation (Gottesman, 1996; Ortega, et al, 2002).

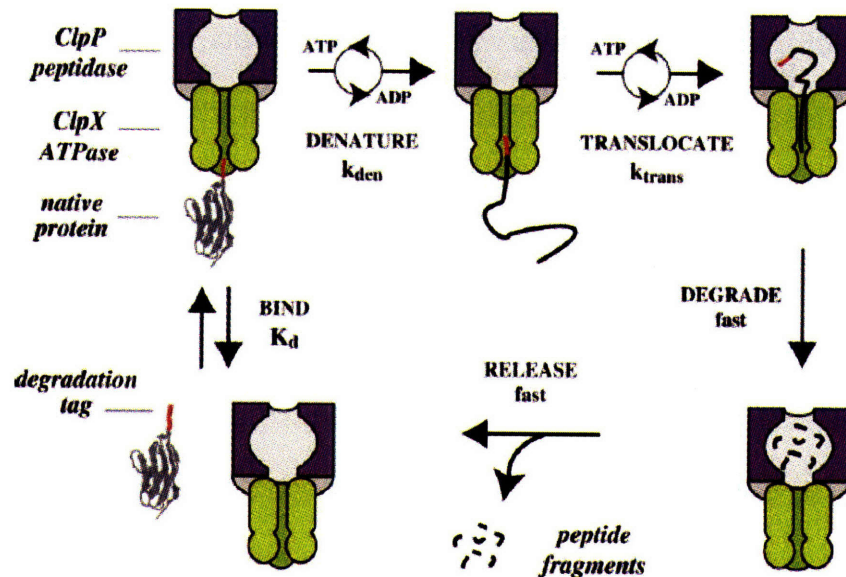


Figure 1.2 Model for the degradation of native proteins by the ClpXP protease. In the first step of the cycle, ClpX recognizes ssrA-tagged substrates and reversibly binds them. It then proceeds to denature the substrate in an ATP-dependent manner. Upon unfolding, ClpX uses ATP to translocate the substrate into the cavity of the ClpP, where it undergoes fast degradation and release of the resulting peptide fragments. Diagram was adapted from Kenniston, et al, 2003.

ATP Binding, Hydrolysis, and Force Generation

There has been some debate about the mechanism by which ClpX converts energy resulting from ATP hydrolysis into the mechanical energy required to unfold and

translocate substrates. Even though there are six identical subunits in a ClpX hexamer, there is substantial evidence indicating different behavior among the subunits. Recent results suggest that only 3 or 4 of the ClpX monomers are capable of binding ATP at any given time (Hersch, et al, 2005). Furthermore, half of these sites appear to release ATP quickly while the other half releases it slowly (Hersch, et al, 2005). In addition, hexamers of covalently linked ClpX monomers with active or inactive functionalities have shown that diverse geometric arrangements support substrate degradation (Martin, et al, 2005). Indeed, hexamers with only a single active subunit are capable of degrading substrates (Martin, et al, 2005). In fact, the degradation capability of a hexamer increases with the number of active subunits in the hexamer, but is independent of the relative locations of the active subunits (Martin, et al, 2005). Taken together, these results rule out a model of concerted hydrolysis in which all or a fraction of subunits simultaneously hydrolyze ATP. They also disfavor sequential hydrolysis in which hydrolysis in one subunit leads to hydrolysis in an adjacent subunit and so on. It seems that the most likely mechanism is one in which hydrolysis is probabilistic rather than predetermined.

Further experiments involving ClpXP and the unfolded I27 system revealed that ClpXP hydrolyzes about 600 ATP molecules per minute during translocation (Kenniston, et al, 2003). An analysis of folded I27 domains with different thermodynamic stabilities revealed that the ATP hydrolysis rate during denaturation was constant (150 min^{-1}) and independent of substrate stability (Kenniston, et al, 2003). This suggests substrate dissociation from ClpX after engagement, slippage between the substrate and ClpX's

mechanical actuator, or both. Nucleotide hydrolysis experiments have also revealed that ClpX is continuously hydrolyzing ATP at a rate of 140 molecules per minute in the absence of a substrate (Burton, et al, 2003). Interestingly, ClpXP hydrolyzes ATP at a rate of 60 min^{-1} in the same conditions. It is believed that ClpP may stabilize ClpX, resulting in ClpX requiring less energy to remain functional. The ClpXP ATP hydrolysis rate increases dramatically to about 280 min^{-1} in the presence of *ssrA*-tagged GFP, which suggests that the substrate binding increases the energy demands of ClpX. However, no degradation of such substrate was observed when an ATP analog, ATP γ S (adenosine 5'-O-(3-thiotriphosphate)), was employed as the main fuel source even though both nucleotides exhibit similar affinities towards ClpX (Burton, et al, 2003). In contrast, ClpXP did degrade *ssrA*-tagged Arc in the presence of ATP γ S. Another experiment showed that ClpX was capable of translocating acid denatured *ssrA*-GFP with ATP or ATP γ S as fuel sources, although at rates exhibiting a 20-fold difference (Burton, et al, 2003). Finally, ATP γ S fueled ClpXP was observed to be able to degrade *ssrA*-P22 (Burton, et al, 2003). Perhaps, the hydrolysis of ATP γ S is slow enough such that partially unfolded substrates are capable of refolding before the next hydrolysis event and subsequent power stroke take place. This suggests that the refolding kinetics of the substrate may limit ClpX's unfolding capabilities.

None of the above experiments have been able to address the question as to what forces ClpX is capable of exerting on its substrates. It is widely believed that this ATPase must be capable of pulling on its substrate's C-terminals with a force of at least 150 pN, the force observed to unfold I27 in AFM experiments (Rief, et al, 1997).

However, the pulling geometry in these experiments differs greatly from that associated with ClpX. Forces applied with an AFM are biaxial (two constrained ends); therefore, molecules are in tension throughout. Forces applied by ClpX are local to the region of contact between ClpX and the substrate. It is the equivalent of trying to pull a knot through a small hole versus trying to pull the knot apart by pulling on its two ends. These very different scenarios will undoubtedly result in different forces necessary to undo a knot or protein.

Optical Tweezers

Since their initial demonstration (Ashkin, 1970; Ashkin and Dziedzic, 1971), optical tweezers have been widely adopted to noninvasively explore the effects of mechanical forces on biological systems at the molecular and cellular length scales. In particular, optical tweezers have been used to study the mechanics of polymers and biopolymers (Furst and Gast, 1999; Smith, et al, 1996; Wang, et al, 1997), filamentous phage (Khalil, et al, 2007), and cellular membranes (Raucher and Sheetz, 2000), the processivity of molecular motors (Abbondanzieri, et al, 2005a; Asbury, et al, 2003; Mehta, et al, 1999), protein folding and unfolding (Cecconi, et al, 2005), and the strength of receptor-ligand interactions (Litvinov, et al, 2005), among others (Grier, 2003). Other applications include the manipulation of individual viruses, bacteria, organelles, and even complete cells (Ashkin and Dziedzic, 1987; Ashkin, et al, 1987).

Optical tweezers offer unprecedented control over trapped particles, as position and force resolutions on the order of nanometers and picoNewtons, respectively, are

common in practice. Furthermore, for displacements smaller than ~ 100 nm, optical traps behave as Hookean springs, allowing the trap to be characterized by a single parameter, its stiffness, which relates the position of the trapped object, usually a spherical bead, to the force being exerted on it. For these reasons, optical tweezers can be used as an active or passive instrument. In the passive case, it simply monitors the position of the bead as a function time, which can then be used to infer the rheological properties of surrounding media (Addas, et al, 2004) or to track the motion of molecular motors (Neuman, et al, 2003). In the active case, it is used to force conformational changes in proteins or molecules to occur by lowering the energetic barrier of such transitions (Cecconi, et al, 2005; Liphardt, et al, 2001). Thus, optical tweezers are extremely versatile tools that can be used to address a host of biophysical and biological phenomena. For a review of optical trapping please refer elsewhere (Neuman and Block, 2004; Svoboda and Block, 1994a).

Instrumentation and Physical Principles

Stable trapping is commonly achieved by using a high numerical aperture objective to tightly focus an infrared laser beam to a diffraction limited spot. The interaction of the focused beam with freely diffusing dielectric particles gives rise to two forces: a scattering force and a gradient or restoring force. The scattering force is destabilizing and pushes objects along the direction of the incident light, while the gradient force, resulting from refraction (Ashkin, 1992) and the induction of dipoles in dielectric materials (Jackson, 1999), pulls particles toward the high intensity focus of the laser beam. Thus, the stability of the trapping phenomenon hinges on the dominance of the

restoring force over the scattering force. This condition necessitates a very steep gradient in light and can be met by employing a trapping laser with a TEM₀₀ or Gaussian mode (Figure 1.3). In fact, the forces experienced by the trapped particle are proportional to the derivative of the gradient of the light. Thus, when the trapped particle is in the center of the trap, it experiences an average force of zero piconewtons.

However, the force increases linearly as the particle is pulled towards away from the center of the trap until displacements on the order of 100 nm. If the trapping laser beam does not have a symmetrical mode, stable trapping can not be achieved (Figure 1.3).

As a rule of thumb, optical tweezers can trap polystyrene beads with diameters of 1 μm with a stiffness of 0.1 pN/nm for every 100 mW of trapping laser power delivered to the specimen plane. In practice, optical tweezers are used to exert forces on the order of 10 pN; however, they have been used to exert forces on the order of 100 pN in particular arrangements (Maier, et al, 2002; Mills, et al, 2004).

Optical tweezers instruments are typically built around inverted microscope platforms, which are heavily modified to improve their mechanical stability and robustness. In addition, they are usually equipped with Nomarski optics and a piezo-electric stage with nanometer resolution that compliments the position capabilities of the trap and is commonly employed in force clamp applications (Lang, et al, 2002; Visscher, et al, 1999). The trap is commonly steered by placing a Keplerian telescope upstream the trapping laser path relative to the objective. However, to achieve finer and faster trap steering, acousto-optic deflectors (AODs) are placed upstream the Keplerian telescope at the back focal plane of the optical system. The AODs add much flexibility to the

optical trapping system as they translate the position of the trap in the specimen plane at rates as high as 50 kHz and can be used in time sharing applications where a single trapping laser is scanned among different locations to form multiple traps (Visscher, et al, 1996). Finally, most advanced optical tweezers employ a secondary laser for the independent detection of the position of the trapped microsphere relative to the center of the trap. After interacting with the trapped bead, the scattered detection laser is spectrally isolated and imaged on a position sensitive device for back focal plane detection (Gittes and Schmidt, 1998; Visscher, et al, 1996). An optical layout for a high-end optical tweezers instrument is presented in Chapter II (Figure 2.1).

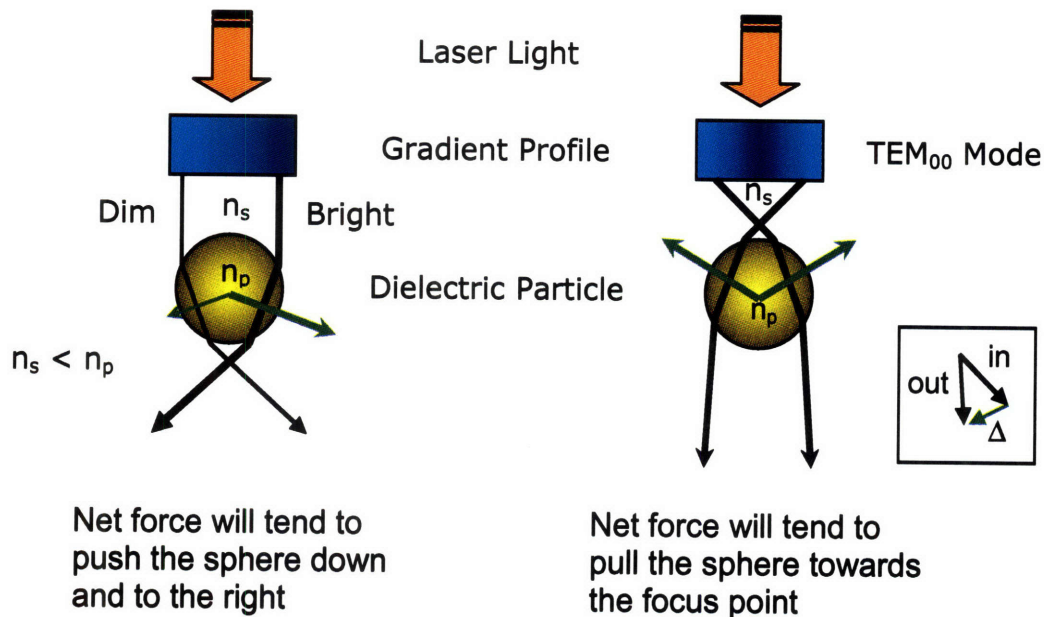


Figure 1.3 Ray optics depiction of the optical trapping phenomenon. When a dielectric particle with an index of refraction larger than the index refraction of the surrounding medium encounters the focused trapping laser, it refracts the rays of the beam and is attracted to the point of highest intensity. (left) Unstable trapping is achieved when a beam of light with an intensity gradient increasing from left to right is employed. (right) Stable trapping is achieved when a Gaussian beam is employed. In both cases the particle is attracted towards the focal point of the laser beam. (inset) Refraction of light by the particles changes the direction of the light, which gives rise to the gradient force.

Calibrating an Optical Trap

Quantitative optical tweezers applications require accurate position calibration. Not only is the force exerted on a trapped particle proportional to its displacement from the center of the trap, but, under no external loads, the motion of the trapped particle can be related to the stiffness of the trap. For traps whose position can be controlled with AODs, the position of the trap in the specimen plane can be determined by moving a trapped particle and taking images at each position. The bead position records can then be calibrated against a Ronchi ruler or a series of image records of a surface-bound bead moved at predetermined steps with a piezo stage. Once the position of the trap has been calibrated in the specimen plane, it can be used to determine the position response of the detector. When a stationary detection laser is employed, this is easily done by raster scanning a trapped bead across the detection zone and recording the corresponding signals. The detector response will be linear for small displacements along both lateral dimensions. However, it becomes nonlinear at large displacements, making it hard to calibrate the outer edges of the trap (Figure 1.4). In fact, for most optical tweezers applications, data is only recorded while the bead is within the linear portion of the curve, which is commonly approximated with a fifth-order polynomial.

Once the relationship between bead position and detector response has been established, it can be used to determine the stiffness of the optical trap, which can be influenced by the numerical aperture of the objective used, the diameter and height above the surface of the bead trapped bead, and the amount of trapping laser power

delivered to the specimen plane (Berg-Sorensen and Flyvbjerg, 2004; Neuman and Block, 2004; Svoboda and Block, 1994a). There are three methods that are commonly used to characterize the stiffness of the trap. The first method relies on moving the fluid around a trapped bead at different velocities and measuring the corresponding bead displacements. The trap stiffness can then be computed by establishing a force balance between the Stokes drag imparted on the trapped bead by the moving fluid and the restoring force of the trap. This method is the slowest, but it allows for the best characterization of the outer edge of the trap. However, it requires an automated piezo stage that can reproducibly move at high velocities, which can make stiff traps hard to characterize. The second stiffness calibration method assumes that the trap behaves like a harmonic potential and relates the positional variance of a bead in a stationary trap to the thermal energy of the medium. This method is very simple, but care should be taken when employing it as low frequency drift and other noise sources will increase the variance of bead position, leading to an underestimation of the trap stiffness. The final stiffness calibration method takes the one-sided power spectral density of a bead position trace and fits it to a Lorentzian function, which is characterized by a corner frequency parameter that is proportional to the trap stiffness. This method provides the most information about the behavior of the optical trap in the least amount of time, reveals the presence of noise invisible to the other methods, and can be used to monitor local heating caused by the absorption of light by the trap (Abbondanzieri, et al, 2005b; Peterman, et al, 2003). These calibration methods are reviewed in Chapter V and elsewhere (Neuman and Block, 2004; Svoboda and Block, 1994a).

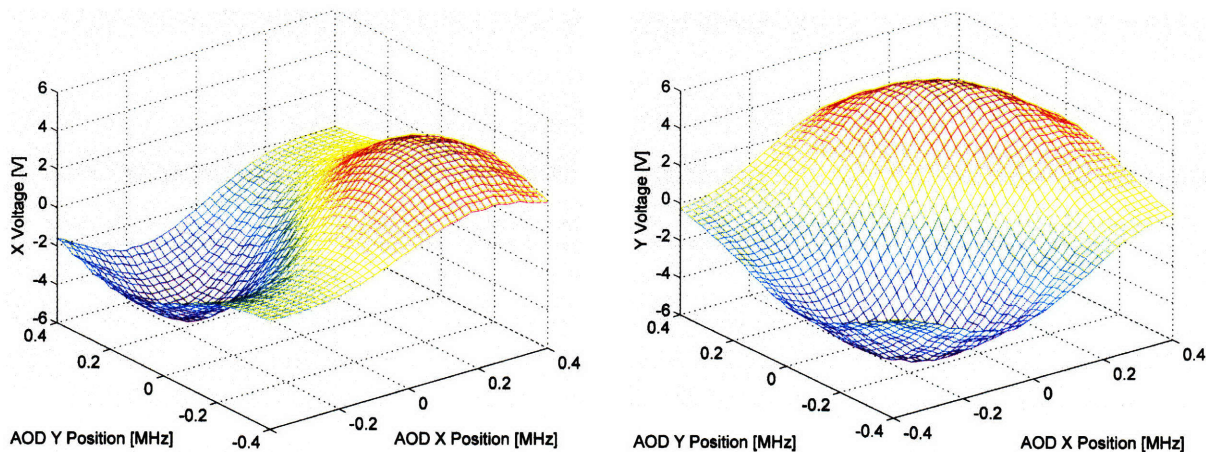


Figure 1.4 Two-dimensional position calibration of an optically trapped bead. (left) X and (right) Y voltage signals from a position sensitive device were recorded as a trapped bead was raster scanned across the detection zone. For small displacements, the dependence of voltage signal on position is linear, but at larger displacements, the dependence becomes highly nonlinear. One AOD MHz unit corresponds to approximately one micron of movement in the relative position of the trap.

Single Molecule Fluorescence

Even though fluorescence is extensively used in imaging and detection at the bulk scale (Kim, et al, 2003), it has been increasingly finding applications at the single molecule level (Weiss, 1999). Single molecule fluorescence, unlike bulk fluorescence techniques, provides information about the particular behavior of an individual molecule, not the average behavior of the population. Thus, it can be used to reveal heterogeneities or microstates, and to quantify and measure nonequilibrium behavior under equilibrium conditions, as is the case in enzymatic reactions (Chen, et al, 2003), protein folding (Schuler, 2005), and mechanochemical coupling in molecular motors (Peterman, et al, 2004).

One of the first applications of single molecule fluorescence monitored the binding and hydrolysis of dye-labeled ATP by individual surface-immobilized myosin molecules (Funatsu, et al, 1995). Since then, the processive movement of kinesin-GFP fusion proteins has been observed along fluorescent microtubules (Pierce, et al, 1997; Vale, et al, 1996) and the heads of myosin V have been labeled with different fluorophores, revealing that they take alternating steps (Warshaw, et al, 2005). Other applications of single molecule fluorescence include monitoring the dynamics of RecA filaments along ssDNA (Joo, et al, 2006), the enzymatic degradation of substrates by lysozyme (Chen, et al, 2003), the catalysis and folding of ribozymes (Zhuang, et al, 2000), the trafficking of viruses in cells (Lakadamyali, et al, 2003), the assembly of telomerase (Stone, et al, 2007), and the sliding of glycosylase enzymes on dsDNA (Blainey, et al, 2006). Even though all of these experiments have been carried out in vitro, in vivo single molecule fluorescence applications have started to emerge (Elf, et al, 2007). Finally, the power of single molecule fluorescence has been harnessed to make sub-diffraction optical observations at the nanometer length scale (Rust, et al, 2006; Yildiz, et al, 2003).

Physicochemical Principles

Fluorescence is a luminescent process in which the molecular absorption of photons leads to the emission of photons with a longer wavelength by the same molecule. This distinction between the absorbed and the emitted photons is known as Stokes shift and implies that there is a loss of energy during the fluorescent process. In fact, the absorption of a photon by a fluorophore leads to an electronic transition consisting of the promotion of an electron from its ground or resting state, S_0 , to an excited singlet

state, S_1 , whose energy level is typically too high for it to be spontaneously populated by thermal energy. Following the absorption of light, a process that takes on the order of a few femtoseconds (Lakowicz, 2006), the excited electron will rapidly relax to the lowest vibrational level of the excited singlet state. This process is known as vibronic relaxation and lasts on the order of picoseconds (Bernath, 2005). Then, the excited electron will return to the ground state and release its stored energy in the form of fluorescence light. Since energy was lost during vibronic relaxation at the excited singlet state, the emitted photon has less energy, and a longer wavelength, than the absorbed photon. It is worth noting that since the fluorescence lifetime of the electron is on the order of nanoseconds, vibronic relaxation is typically complete prior to emission (Lakowicz, 2006). These fluorescence processes are typically captured in a Jablonski diagram, which is presented below (Figure 1.5).

Electrons in an excited singlet state can also undergo intersystem crossing to reach an excited triplet state (Figure 1.5). Once in the triplet state, fluorescence emission via a return to the ground state is also possible and is termed phosphorescence. However, it is generally shifted to longer wavelengths and is characterized by time constants on the order of microseconds or longer (Lakowicz, 2006). This characteristic has been exploited for commercial applications as is the case for glow in the dark toys. The triplet state also presents practical complications as it is more reactive than the excited singlet state and can lead to irreversible photobleaching, which is the photochemical destruction of the fluorophore. The exact photobleaching mechanism is not well

understood, but it is correlated with excitation laser power and to the presence of molecular oxygen in buffers (Rasnik, et al, 2007).

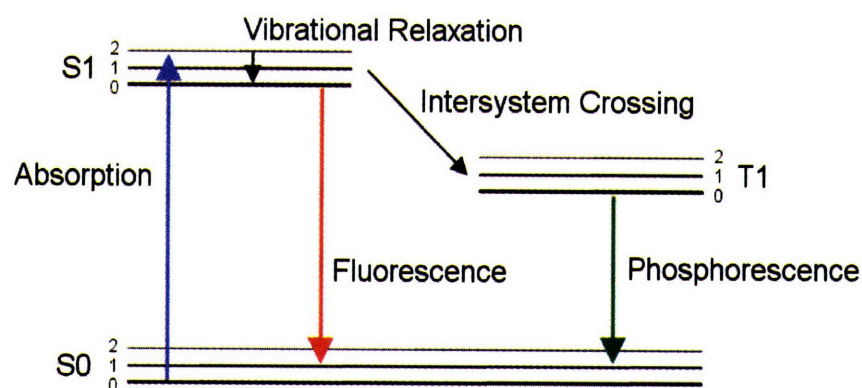


Figure 1.5 Sample Jablonski diagram. Electrons lying in the ground state, S_0 , can be excited to the singlet state, S_1 , via the absorption of photons. The excited electron will then rapidly undergo vibrational relaxation to the lowest energy of the singlet state before returning to the ground state and releasing its stored energy in the form of fluorescent light. Alternatively, excited electrons can undergo intersystem crossing to populate the molecule's triplet state, T_1 , where they can return to the ground state via phosphorescence.

In addition to being influenced by their environment, fluorophores can also interact with neighboring fluorophores via both radiative and non-radiative processes requiring the presence of a donor and an acceptor. In radiative energy transfer, the donor fluorophore emits photons that are absorbed by the acceptor, which then proceeds to emit photons of its own (Valeur, 2002). This type of interaction is solely dependent on the spectral overlap between the donor and the acceptor and has been used to measure the thickness of thin fluid films (Hidrovo, et al, 2004). In contrast, non-radiative transfer occurs without the exchange of photons, although there needs to be spectral overlap between the donor and the acceptor as well (Valeur, 2002). Of the different examples of non-radiative transfer interactions, Forster resonance energy transfer (FRET) is the

most important for biological applications. FRET requires a long range dipole-dipole interaction between the donor and acceptor and can be used to measure distances on the order of a few nanometers (Valeur, 2002). The distance over which FRET occurs is called the Forster radius, and is particular for every donor and acceptor pair, although typically in the range of 5 nm. FRET is often referred to as a molecular ruler because the amount of energy transfer is dependent on the distance between the donor and the acceptor. At short distances on the order of 1 nm, FRET efficiency or transfer is high, and at large distances on the order of 10 nm, FRET efficiency is low. This behavior is ideal for the study of the conformational changes of biomolecules (Weiss, 1999).

Technology

The advent of single molecule fluorescence is the result of major technological advancements. The first of these is the development of total internal reflection fluorescence (TIRF) techniques, which significantly improve the imaging signal-to-noise by eliminating background fluorescence sources not present in the focal plane. This is achieved by exciting fluorophores dissolved in a medium, such as water, proximal to a surface with a high index of refraction, such as glass. The mismatch in index of refraction can be exploited to create an evanescent wave that decays on the order of the wavelength of the exciting light by using total internal reflection at the interface between the two media (Hecht, 2002). The first demonstration of such technique for a biological application employed prism-side TIRF to monitor the absorption of dye-labeled proteins on a surface (Burghardt and Axelrod, 1981). Since then, objective-side TIRF techniques have been developed that avoid having to image the specimen plane

through the bulk of the sample (Tokunaga, et al, 1997). Since the specimen plane is now proximal to the objective, this allows for the use of objectives with higher numerical apertures, which is always ideal when dealing with fluorophores whose emission cone is on the order of 200 nm. In addition, objective-side TIRF makes use of a more compact instrument design that leaves the chamber face opposite to the objective free for other applications.

A second major technological advancement is the development of electron multiplying charge-coupled devices (EMCCD) that are better suited for the detection of low light level sources like fluorophores and faint stars than traditional CCDs. A third technological advancement is the development of extremely bright fluorophores that can be easily conjugated to target molecules via different attachment chemistries (Table 1.1). These dyes are characterized by high extinction coefficients and quantum yields, which are measures of a fluorophore's ability to absorb photons and to convert them into emitted ones, respectively. These fluorophores are still plagued by photobleaching, one of the biggest problems in single molecule fluorescence experiments, but their longevities can be typically extended by using appropriate buffers and oxygen scavenging systems (Rasnik, et al, 2007). A novel kind of fluorophore known as a quantum dot has been introduced to the single fluorescence community and offers unparalleled brightness and photostability. However, its attachment chemistries are not well developed and it suffers from blinking problems, in addition to being larger than traditional organic dyes (Hohng and Ha, 2004). Finally, the green fluorescent protein (GFP) and its derivatives compliment the plethora of synthetic fluorophores available

(Table 1.1). Of course, GFP has the advantage of being genetically encodable in any gene, but it is extremely dim and photobleaches faster than most fluorophores.

Dye	Typical Excitation Laser Line [nm]	Absorbance Maximum [nm]	Emission Maximum [nm]	Extinction Coefficient [$M^{-1} cm^{-1}$]
Alexa488	488	495	519	71,000
GFP	488	488	509	61,000
Alexa532	532	532	554	81,000
Alexa555	532	555	565	150,000
Cy3	532	550	570	150,000
TMR	532	550	573	95,000
Cy5	635	649	694	250,000
Alexa647	635	650	665	239,000

Table 1.1 Common single molecule dyes and their spectral properties. The extinction coefficients correspond to the maximum absorbance wavelength of the dye. With the exception of GFP, all the dyes in the table are synthetic.

Chapter II

Interlaced Force-Fluorescence Spectroscopy

(This chapter was adapted from Brau, et al, 2006 and Tarsa, et al, 2007)

Abstract

Combining optical tweezers with single molecule fluorescence offers a powerful technique to study the biophysical properties of single proteins and molecules. However, such integration into a combined, coincident arrangement has been severely limited by the dramatic reduction in fluorescence longevity of common dyes under simultaneous exposure to the trapping and fluorescence excitation beams. We present a novel approach to overcome this problem by alternately modulating the optical trap and excitation beams to prevent simultaneous exposure of the fluorescent dye. We demonstrate the dramatic reduction of trap-induced photobleaching effects on the common single molecule fluorescence dye Cy3, which is highly susceptible to this destructive pathway. The extension in characteristic fluorophore longevity, a 20-fold improvement when compared to simultaneous exposure to both beams, prolongs the fluorescence emission to several tens of seconds in a combined, coincident measurement. Furthermore, we show that this scheme, interlaced optical force-fluorescence, does not compromise the trap stiffness or single molecule fluorescence sensitivity at sufficiently high modulation frequencies. Such improvement permits the

simultaneous measurement of the mechanical state of a system with optical tweezers and the localization of molecular changes with single molecule fluorescence, as demonstrated by mechanically unzipping a 15-basepair DNA segment labeled with Cy3 and by using a Cy3-Alexa647 FRET pair to monitor the force-induced conformational changes of a DNA hairpin.

Introduction

Significant advances in single molecule techniques and their application to biological systems have provided new insight into the mechanistic behavior of single proteins and other biological molecules (Ha, 2001; Vale and Milligan, 2000; Weiss, 1999). Two such techniques, single molecule fluorescence spectroscopy and optical tweezers force spectroscopy, permit the direct observation of energetic heterogeneities and conformational differences within populations that may be otherwise lost in the inherent averaging of bulk measurements. Optical tweezers force spectroscopy yields quantitative information about the mechanical forces involved in interactions at the single molecule level (Neuman and Block, 2004), and single molecule fluorescence reports on binding interactions and provides insight into the structural and conformational states of proteins (Kapanidis and Weiss, 2002). Although these two experimental approaches independently provide different perspectives from which to approach biological problems, their combination results in a powerful tool for the analysis of molecular motors, protein–protein and protein–DNA interactions, biomolecular conformational changes, and mechanotransduction pathways (Ishijima and Yanagida, 2001; Lang, et al, 2003; Wallace, et al, 2003; Wang, et al, 2005;

Weitzman, 2003). In this report, we describe a novel technique that dramatically improves both the practicality and versatility of such an arrangement by eliminating a dominant photobleaching pathway that results from the exposure of excited-state fluorophores to the high photon flux of optical tweezers (van Dijk, et al, 2004). This technique, in which the trapping and fluorescence excitation beams are alternately modulated, allows for the seamless integration of optical trapping and single molecule fluorescence without compromising trap stiffness or fluorescence sensitivity.

Optical tweezers force spectroscopy has been widely adopted for exploration of the effects of mechanical forces on single molecule systems (Neuman and Block, 2004). The high force and position sensitivity that facilitates such measurements, typically on the order of piconewtons and nanometers, respectively, is achieved by trapping and manipulating a dielectric particle within a tightly focused laser beam. In most instances, the trapped particle is tethered in close proximity to a biological specimen and can be used to noninvasively measure the mechanics of single molecules and their binding interactions (Bustamante, et al, 2003; Greenleaf, et al, 2005; Koch and Wang, 2003; Miyata, et al, 1996; Pant, et al, 2005). In addition, optical tweezers have found particular applicability for studying the mechanical properties of molecular motors, such as kinesin, myosin, RNA polymerase, and others (Asbury, et al, 2003; Rief, et al, 2000; Shaevitz, et al, 2003; Smith, et al, 2001).

Although optical tweezers force experiments are critical to understanding the molecular underpinnings of a variety of biological processes, the combination of this technique

with single molecule fluorescence spectroscopy further extends its versatility. By incorporating direct reporting through a fluorescent label, single molecule fluorescence provides an added observable dimension that allows the examination of the localized effects of applied forces on the system of interest (Wallace, et al, 2003; Weitzman, 2003). In addition, single-molecule FRET spectroscopy can provide complementary information about dynamic structural properties, including environment, orientation, and proximity, with comparable spatial resolution (Ha, et al, 1996). However, despite technological advances that have made single molecule fluorescence more accessible (Pierce, et al, 1997), a practical approach for its integration with optical tweezers has remained elusive due to the destructive photobleaching effects that are caused by the trapping beam (Lang, et al, 2003; van Dijk, et al, 2004).

Several approaches pioneered the development of instruments that simultaneously combine these two techniques. For example, dual-beam optical trap configurations have been employed to separately study the motility of Cy3-labeled RNA polymerase along double-stranded DNA (dsDNA) and the mechanochemical interactions between myosin and actin filaments (Harada, et al, 1999; Ishijima, et al, 1998). These assay geometry arrangements require either filamentous proteins or dsDNA to be suspended between the two independent optical traps, limiting its adoption for experimental systems demanding coincident trapping and fluorescence. Such a design was later demonstrated using an efficient optical trap configuration in combination with objective-side fluorescence illumination, high-performance optical filters, and a judicious choice of a fluorescent marker that is not heavily susceptible to trap induced photobleaching

(Lang, et al, 2003; Lang, et al, 2004). This apparatus, which used fluorescence to confirm the mechanical unzipping and shearing of tetramethylrhodamine (TMR)–labeled dsDNA, incorporates a fluorescence excitation laser and single molecule fluorescence detection equipment that can be easily interfaced with optical tweezers instrumentation. Unfortunately, neither method directly addresses the recently quantified phenomenon of trap-induced photobleaching, a process to which TMR exhibits very little susceptibility. Furthermore, TMR is not a popular single molecule dye because of its relatively low quantum yield and extinction coefficient and because its conjugation to proteins can lead to a considerable loss of fluorescence (Panchuk-Voloshina, et al, 1999). Even if these limitations could be generally overcome at the single molecule level, complicated experimental schemes involving multiple fluorophores, such as FRET, will necessarily employ dyes other than TMR.

Current approaches are impractical with popular single molecule dyes, such as Cy3 and Alexa555, because their fluorescence longevity is severely reduced by over an order of magnitude when employed in a combined, coincident arrangement (van Dijk, et al, 2004). In this report, we present a temporally based solution that extends the longevity of such fluorophores in the presence of a high-intensity optical trap by alternately modulating the trapping and fluorescence excitation beams. This technique, which we term interlaced optical force-fluorescence (IOFF), requires only minor modification of conventional optical tweezers arrangements and does not compromise trap integrity. We further demonstrate the effectiveness of this approach using Cy3, a commonly employed single molecule dye that is highly susceptible to trap-dependent

photobleaching (van Dijk, et al, 2004), to show dramatic improvement in single molecule fluorophore longevity in the presence of a trapping laser. Cy3 is an exceptionally bright dye, and, to our knowledge, this is the first instance in which Cy3 has been used in a combined, coincident optical tweezers and single molecule fluorescence arrangement. Furthermore, we effectively combine the two techniques for the mechanical unzipping of a Cy3-labeled 15-bp dsDNA. This model system confirms the nominal effects of laser modulation on trap stiffness and represents a significant step in extending the versatility of IOFF.

To further display the power of IOFF, we show that optical modulation of the trapping and fluorescence lasers can be adapted to extend the emission times of FRET-paired labels without otherwise affecting their photophysical properties. To demonstrate this technique, we describe the first combination of optical tweezers force microscopy with the single molecule FRET detection of a novel force-sensing molecule into a single, integrated method capable of actively controlling molecular structure while simultaneously monitoring the conformational state of a single DNA hairpin molecule. Such a technique may be applicable to a range of fluorophores and molecular geometries and opens the possibility for the exploration of more advanced systems, such as real-time binding kinetics or catalytic conformational changes.

Materials and Methods

Instrument Design

The combined optical tweezers and single molecule fluorescence instrument (Figure 2.1) is based on a heavily modified inverted microscope (Nikon, Melville, NY) and is similar to previously proven arrangements (Lang, et al, 2002; Lang, et al, 2004). This device combines separate lasers for optical trapping (1064 nm; Coherent, Santa Clara, CA), position detection (975 nm; Corning Lasertron, Bedford, MA), and fluorescence excitation (532 nm; World Star Tech, Toronto, ON) through a base that has improved mechanical stability, incorporated Nomarski optics, and a piezoelectric stage (Physik Instrumente, Auburn, MA). In addition, the arrangement includes a pair of computer controlled acousto-optic deflectors (AODs; IntraAction, Bellwood, IL), which permit precise steering of the trapping beam in two dimensions, and remote-controlled flipper mirrors and shutters, which facilitate rapid switching between bright-field imaging (CCD camera; DAGE-MTI, Michigan City, IN) and high-sensitivity fluorescence detectors.

Both the trapping and detection lasers are guided into the microscope objective (100X, 1.40 numerical aperture, oil infrared; Nikon, Melville, NY) via a dichroic mirror (Chroma Technology, Rockingham, VT) that reflects only near-infrared light. The diameter of the trapping laser beam is adjusted with a telescope to slightly overfill the objective pupil to ensure high efficiency trapping. After passing through the microscope condenser lens, the detection beam is spectrally isolated (Andover, Salem, NH) from the trapping beam and imaged on a position-sensitive device (PSD; Pacific Silicon, Westlake Village, CA) for back focal plane detection (Gittes and Schmidt, 1998; Visscher, et al, 1996). This

optical tweezers arrangement was calibrated using previously described procedures (Lang, et al, 2002; Neuman and Block, 2004) and was found to be capable of trapping 500-nm-radius polystyrene beads with a stiffness of ~ 0.1 pN/nm per 100 mW of unmodulated trapping laser power.

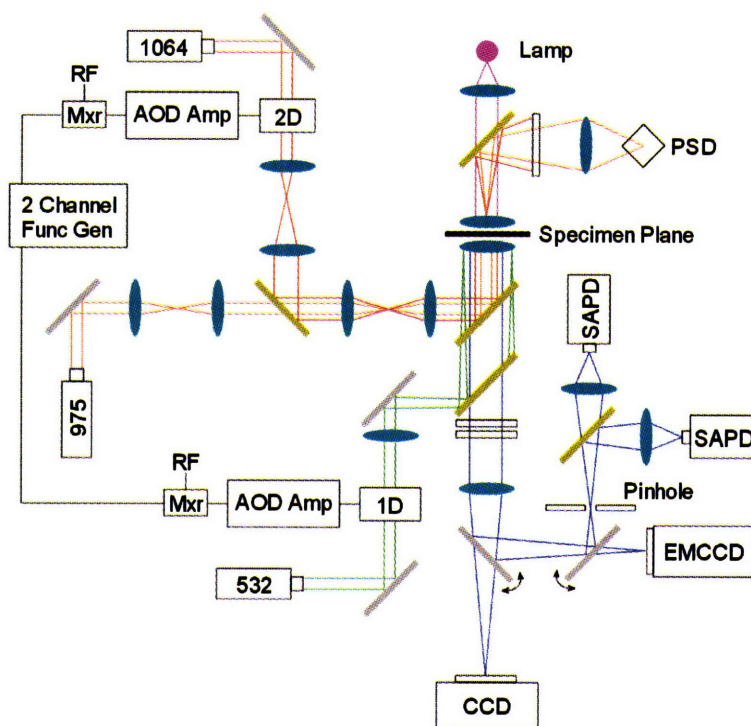


Figure 2.1 Optical layout of the instrument combining optical tweezers and single molecule fluorescence. All lenses, including the objective and condenser, are displayed as light-blue ovals. Filters, mirrors, and dichroics are represented as white, silver, and gold-filled rectangles, respectively. Trapping (red) and detection (orange) lasers, 1064 and 975 nm, respectively, are guided into the objective and focused on the specimen plane to form an optical trap. The position of the trapped particle is monitored by spectrally isolating and imaging the detection laser on a PSD. Total internal fluorescence excitation, supplied by a 532-nm laser (green), is focused near the back pupil of the objective. Bright-field illumination is provided by a mercury arc lamp (magenta), and images (blue) are collected by a CCD camera. Fluorescence images (blue) are collected by an electron multiplying CCD (EMCCD), and single molecule fluorescence counts are spatially filtered through a pinhole and acquired by a pair of silicone avalanche photodiodes (SAPD). The trapping and excitation lasers are modulated by AODs controlled with an electronic mixer (Mxr) that combines a preamplified radio frequency AOD drive signal with a square wave generated in a function generator.

In addition to these force capabilities, the microscope is outfitted for objective-side total internal reflection fluorescence excitation and single molecule emission detection. The excitation laser, which is controlled by an independent AOD (IntraAction), is guided through a customized optomechanical system that replaces the microscope's fluorescence turret. This modification, which allows for focusing and off-axis translation of the excitation laser along the back focal plane of the objective, is set directly below the trap-steering dichroic mirror. It consists of a filter cube (532-nm dichroic and 540-nm long-pass filter; Chroma Technology) and a KG5 filter (Schott Glass, Elmsford, NY) to reflect the excitation light into the sample, transmit fluorescence emission, and efficiently block scattered or reflected light from the excitation, trapping, and detection lasers. Transmitted fluorescence signals are imaged with either an EMCCD intensified camera (Andor Technology, South Windsor, CT) or a pair of photon-counting silicon avalanche photodiode (SAPD; PerkinElmer, Wellesley, MA). The fluorescence emission collected on the SAPDs passes through a pinhole (ThorLabs, Newton, NJ) conjugate with the specimen plane for the spatial signal isolation from background and bead scattering signals and a 628-nm dichroic mirror (Chroma Technology) for similar spectral separation.

To quickly modulate the intensities of both the trapping and excitation lasers, electronic mixers (Mini-Circuits, Brooklyn, NY) multiply both preamplification AOD radio frequency signals with a square wave signal from a two-channel function generator (Tektronix, Richardson, TX). This technique is similar to a recently demonstrated fluorescence

sorting method (Kapanidis, et al, 2004) and to other trap modulation schemes (Kapanidis, et al, 2004; Lee, et al, 2005; Visscher, et al, 1996). In essence, it temporally turns the trapping and excitation lasers on or off, allowing for their in-phase (IP) or out-of-phase (OP) synchronization. For all the experiments described in this chapter, the fluorescence excitation and trapping lasers were further modulated with a duty cycle of 30% and 50% and set to an average postmodulated power of 250 μ W and 100 mW, respectively. In the OP condition, the pulses of the trapping and excitation lasers are aligned such that there is a 2- μ s dark period in between pulses, as verified by a single photodiode (ThorLabs). The duration of the fluorescence excitation and trapping laser pulses are 10 and 6 μ sec, respectively. For the IP condition, the phase of the trapping laser was shifted by 180°, placing the fluorescence excitation pulse squarely in the middle of the trapping laser pulse (see Figure 3, insets). Custom software (LabView; National Instruments, Austin, TX) acquired all signals through a 16-bit A/D board (National Instruments) and automated all instrument components.

Single Molecule Fluorescence

Flow cells were prepared as previously described (Neuman, et al, 2003). To prepare single molecule samples, flow cells were filled with 20 μ M antidigoxigenin polyclonal antibody (Roche Applied Science, Indianapolis, IN), incubated for 30 min, and washed with 200 μ L of Tris buffer (20 mM Tris, pH 7.5, 6 mM NaCl, 1.7 mM MgCl₂, and 10% glycerol). They were then filled with 40 μ L of 25 pM fluorescent DNA complexes (Operon Biotechnologies, Huntsville, AL) (oligo 1: 5'-Cy3-CCACTCTAGG-Dig-3'; oligo 2: 5'-CCTAGAGTGG-Biotin-3'), which were annealed in TE buffer (pH 8.0; Integrated

DNA Technologies, Coralville, IA) and designed to be similar to those used in other single molecule fluorescence studies (Ha, et al, 2002). After a 15-min incubation, unbound complexes were washed with 200 μ L of fluorescence buffer (Tris buffer, 120 nM catalase (Calbiochem, San Diego, CA), 25 mM β -D(+) glucose (Calbiochem), 1.8 μ M glucose oxidase (Calbiochem), 1% β -mercapto-ethanol (VWR, West Chester, PA), degassed for 30 min in a desiccator). All incubations took place in a humidity chamber at room temperature.

Single, immobilized Cy3-labeled molecules were visualized on the EMCCD camera for \sim 1 s, and isolated fluorophores were chosen and, using the piezo stage, repositioned for pinhole imaging on the SAPD. Fluorescence was collected until a discrete single bleaching step was observed to return count levels to background. After photobleaching, the signal was monitored for at least 30 s to ensure that the fluorophore did not undergo an intermediate dark state electronic transition as observed in some samples. Even though a similar blinking behavior has been previously described (Hoogenboom, et al, 2005), we were careful to exclude them from the analysis because they would introduce unacceptable ambiguity in experiments employing combined, coincident optical tweezers and single molecule fluorescence. All signals were acquired at 20 Hz and were analyzed using MATLAB (The MathWorks, Natick, MA).

dsDNA Unzipping Assay

The dsDNA unzipping assay was prepared as described previously with minor modifications (Lang, et al, 2004). These include using Cy3 as a fluorescence reporter

and replacing the final wash step with 200 μ L of fluorescence buffer containing 0.15 mg/mL bovine serum albumin. Once identified, tethers were precisely located to the pinhole collection zone using the position sensing system in the instrument device. This assay provides a convenient system in which to use Cy3 in a combined, coincident optical tweezers and single molecule fluorescence arrangement.

Hairpin Opening and Closing Assay

A digoxigenin-labeled segment of single-stranded DNA with a 44-base self-complementary internal sequence (digoxigenin-ATGATGGTAGATGATGTATTGTTGTTTCGCCGCGGGCCGGCGCGGGTTTTCCGCGCGCCGGCCCGCGGCGTTTGTGGA GCTGAGATGAGATGGTACTG; Integrated DNA Technologies, Coralville, IA (USA); detailed in reference (Woodside, et al, 2006)) was annealed at its ends to oligonucleotides labeled with Cy3 (Cy3-CAACAATACATCATCTAC CATCATC; Integrated DNA Technologies) and Alexa 647 (GGATCCAGTACCATCTCATCTCAGCT CCACAlexa 647; Integrated DNA Technologies). This complex was then phosphorylated at its 5' end with polynucleotide kinase (New England Biolabs, Ipswich, MA (USA)) and ligated with T4 ligase (New England Biolabs) to a biotinylated 1007-base-pair segment of double-stranded DNA (PABX4T-fimbrin; primer 1: biotin-CAAATC ATCTGTTTCATTGAAACCTGACATG, primer 2: GATCC-abasic-ATGGATGAGATGGC TACCACTCAGATTTCC; Integrated DNA Technologies). Low concentrations of hairpin complexes were incubated with 750 nm avidin-coated polystyrene beads (Bangs Laboratories, Fishers, IN) and immobilized on an antidigoxigenin (Roche Applied Science, Indianapolis, IN)-coated glass coverslip (Corning Life Sciences, Inc., Acton,

MA). Other assay conditions and force-fluorescence instrumentation were as described above.

Results

Optimal Modulation Frequency

When trapped with a modulated laser, the thermally driven motion of a bead is determined by the properties of the focused trapping beam and the bead itself. It is also affected by the frequency and duty cycle at which the trapping laser is modulated, suggesting that the principal effect of modulation is to alter the stiffness of a trap at a given power. These effects have been previously explored for the stable trapping of multiple particles with a single time-shared trap (Visscher, et al, 1996) or with holographic optical tweezers (Curtis, et al, 2002). Here, we further explore these effects on the force-exerting capabilities of the trap to determine optimal modulation conditions.

Thermal effects become apparent when the position of a trapped bead is monitored as a function of time for different modulation frequencies (Figure 2.2). At low frequencies, the trapped bead is allowed to diffuse through a large volume of space, whereas at higher frequencies, the trap constrains its motion to a reduced space. To quantify the effect of modulation on the optical tweezers capabilities, the stiffness of the trap was monitored as a function of modulation frequency for different trapping powers. Trap stiffness, k_x , was measured using the equipartition theorem to relate the mean-squared

displacement of a trapped bead, $\langle x^2 \rangle$, to the thermal energy in the system, $k_b T$, such that $\frac{1}{2}k_x \langle x^2 \rangle = \frac{1}{2}k_b T$.

For a set of modulation frequencies ranging from 100 Hz to 50 kHz, the stiffness of the trap increased monotonically with frequency under constant laser trap power and modulation duty cycle. A similar behavior was also observed when the stiffness of the trap was determined with the Stokes drag and power spectrum calibration methods (results not shown). For each trapping power, the modulated stiffness values were normalized by the measured stiffness for an unmodulated trap (Figure 2.2). The resulting trends resemble an S-curve and are well described with an exponential function of the form $y = A(1 - \exp(-f/f_m))$, where A is the maximum achievable stiffness, f the modulation frequency, and f_m represents a characteristic modulation frequency for the system. As expected, all fits converge near 0.5 at high modulation frequencies (> 10 kHz) with a 50% duty cycle. For trapping powers of 60, 120, 240, and 480 mW, the curves are described by characteristic modulation frequencies of 0.59, 1.5, 3.2, and 7.1 kHz, respectively. These values, which have a linear dependence on average trapping power ($R^2 > 0.99$), correspond to the modulation frequencies at which the trap stiffness is 63% of the maximum stiffness for a modulated trap. Therefore, for a given power, a trap must be modulated at a frequency that is higher than its characteristic frequency of modulation. For example, if it is modulated at a frequency five times greater than its f_m , the resulting trap will be characterized with a stiffness that is 99% of that of a continuous trap formed with the same average power.

In addition to the relationship between the characteristic modulation frequency and trap power, the fits produce a f_m that is ~15% less than the corner frequency of an unmodulated trap at all powers studied. The corner, or roll-off frequency, f_c , describes the motion of a trapped bead and is determined by fitting the power spectral density of bead position to a Lorentzian function (Neuman and Block, 2004). This close dependence suggests that, for a given power, the corner frequency of an unmodulated trap can serve as a guideline to determine the minimum modulation frequency at which it resembles a continuous trap. Alternatively, modulation should occur at the highest frequency possible.

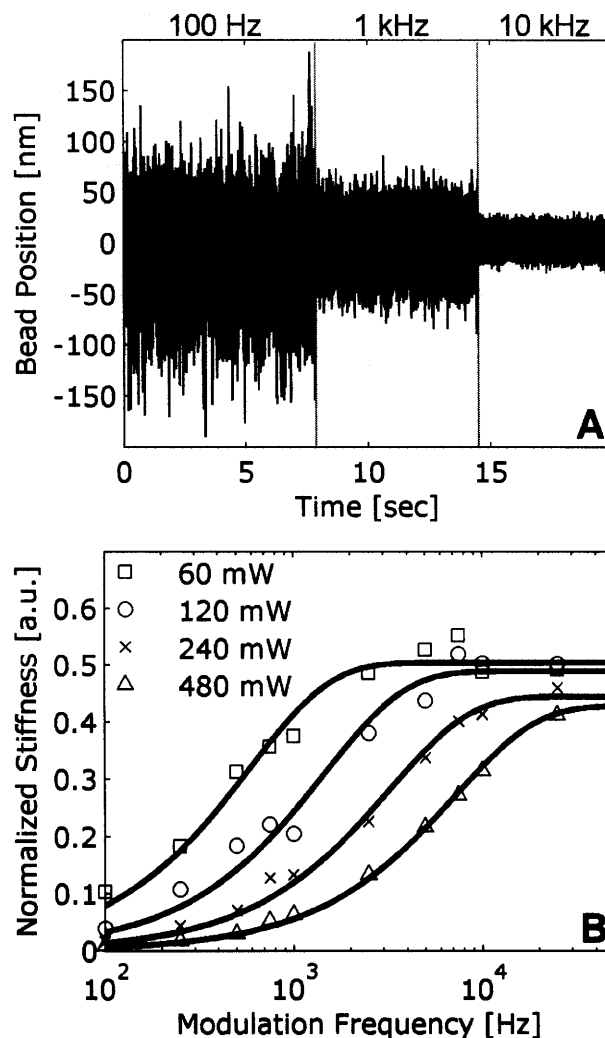


Figure 2.2 Effect of modulation on the integrity of an optical trap. (A) Position trace of a trapped bead for a 50% duty cycle with 100-Hz, 1-kHz, and 10-kHz modulation frequencies. The space explored by the bead is reduced as the modulation frequency increases. (B) Effect of modulation on the stiffness of an optical trap for 60 (\square), 120 (\circ), 240 (\times), and 480 (Δ) mW of trapping laser power. For each power, the measured stiffness was normalized by the trap stiffness of a continuous trap. The data were fit to a simple exponential function, resulting in characteristic modulation frequencies of 0.59, 1.5, 3.2, and 7.1 kHz, respectively.

Fluorophore Longevity

Bulk fluorophore decay rates were found to be independent of modulation frequency; however, they were found to be dependent on the modulation duty cycle and average excitation laser power (results not shown). For these reasons, the fluorescence

excitation laser was modulated at 50 kHz with a 30% duty cycle and set to deliver an average power of 250 μ W, whereas the trapping laser was modulated at 50 kHz with a 50% duty cycle and delivered an average power of 100 mW. These conditions permit the IP or OP synchronization of the trapping and excitation lasers while maintaining the highest possible trap stiffness, reducing the fluorophore photobleaching caused by the excitation laser, allowing good single fluorophore emission sensitivity, and keeping the trapping and excitation laser fluxes constant throughout all experiments. A third condition, in which fluorophores were exposed to the modulated excitation laser with no trapping laser (NT), was used as a control to establish the normal decay profile of the fluorophores. These schemes rely on the separation of time scales between the nanosecond relaxation time constant of excited electrons, the microsecond pulses of our modulation scheme, and the inherent millisecond averaging of the data acquisition rate.

Single Cy3 molecules, which were immobilized on glass coverslips through short DNA linkers to prevent interaction between the fluorophore and substrate, were simultaneously exposed to modulated fluorescence excitation and optical trap lasers to quantify trap-dependent photobleaching effects. The single dyes fluoresced at a constant level before instantaneously bleaching in a single step, returning the signal to background (Figure 2.3). For each condition, the fluorescence emission longevity of 100 Cy3 dyes was recorded, and histograms were fitted to a single exponential decay model to extract a characteristic decay constant for each condition (Figure 3 B–D) (Tokunaga, et al, 1997; Wennmalm and Rigler, 1999). Cy3 fluorophores irradiated in the NT

condition were found to have a decay constant of 89.87 ± 13.05 s, whereas those exposed to the IP and OP arrangements had decay constants of 1.49 ± 0.10 and 32.03 ± 5.72 s, respectively. Clearly, the OP configuration represents a dramatic improvement in the longevity of Cy3 fluorophores over IP. In addition, this modulation condition creates enough time before photobleaching for the low loading rate measurement of mechanical events with an IOFF arrangement.

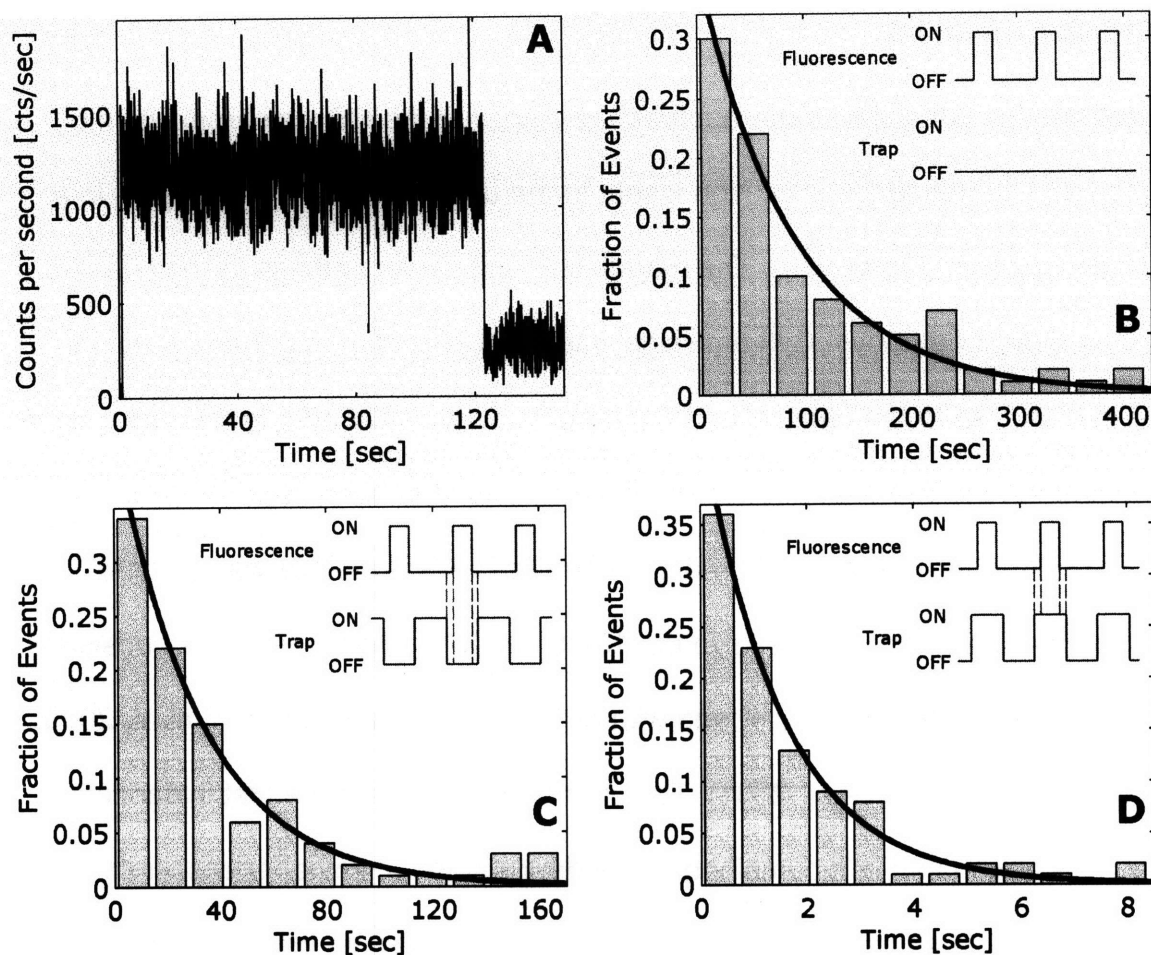


Figure 2.3 Cy3 single molecule fluorescence. (A) Example trace for a single Cy3 photobleaching event exposed to OP trapping and excitation radiation. The fluorophore emits light at a constant rate before irreversibly bleaching in a single step and returning the signal to background level. This particular Cy3 molecule had a longevity of ~ 120 s. Histograms ($n = 100$) of the longevities of single Cy3 fluorophores exposed to the (B) no trap (NT), (C) OP, and (D) IP modulation conditions. The data for each condition were fitted to a single exponential decay model with time constants of 89.87 ± 13.05 s, 32.03 ± 5.72 s, and 1.49 ± 0.10 s, respectively. All fits resulted in $R^2 > 0.95$. Insets contain schematics of the modulation scheme employed for each condition. The hatch marks on the (C) OP and (D) IP insets mark the 2- μ s offset between the trapping and fluorescence excitation laser pulses for each condition. Both trapping and excitation lasers were modulated at 50 kHz with a duty cycle of 50% and 30%, respectively.

Combined Measurement

To demonstrate the suitability of our approach, we applied the OP synchronization of the trapping and fluorescence excitation lasers to the unzipping of a 15-bp region in a simple dsDNA system (Figure 2.4). The modulation and power settings for both lasers were kept as described above. Cy3 emission was used to confirm mechanical events occurring in response to the application of external mechanical loads. In this case, upon dsDNA unzipping, the fluorescence emission was reduced to background levels simultaneously with the mechanical break, confirming that the dsDNA was unzipped (Figure 2.4). The force required to unzip the 15-bp dsDNA region, ~ 10 pN, is consistent with control experiments (Figure 2.4) and with other similar systems (Lang, et al, 2003; Lang, et al, 2004; Liphardt, et al, 2001). To our knowledge, this is the first instance in which Cy3 has been used in a combined, coincident single molecule fluorescence and optical tweezers mechanical measurement. As a control, Cy3 was irradiated with the OP arrangement until irreversibly photobleaching, which occurred at ~ 45 s (Figure 2.4). No force was exerted on the dsDNA system during this period, but after photobleaching, the tether was loaded at 100 nm/s until rupture was observed at ~ 10 pN (Figure 2.4). As expected, the fluorophore emitted at a constant level and was not disturbed by the presence of the trap. However, when compared to the traces from the system in the single molecule fluorescence longevity study, there was a small increase in background and signal noise likely due to the presence of the bead and slightly different molecular configuration.

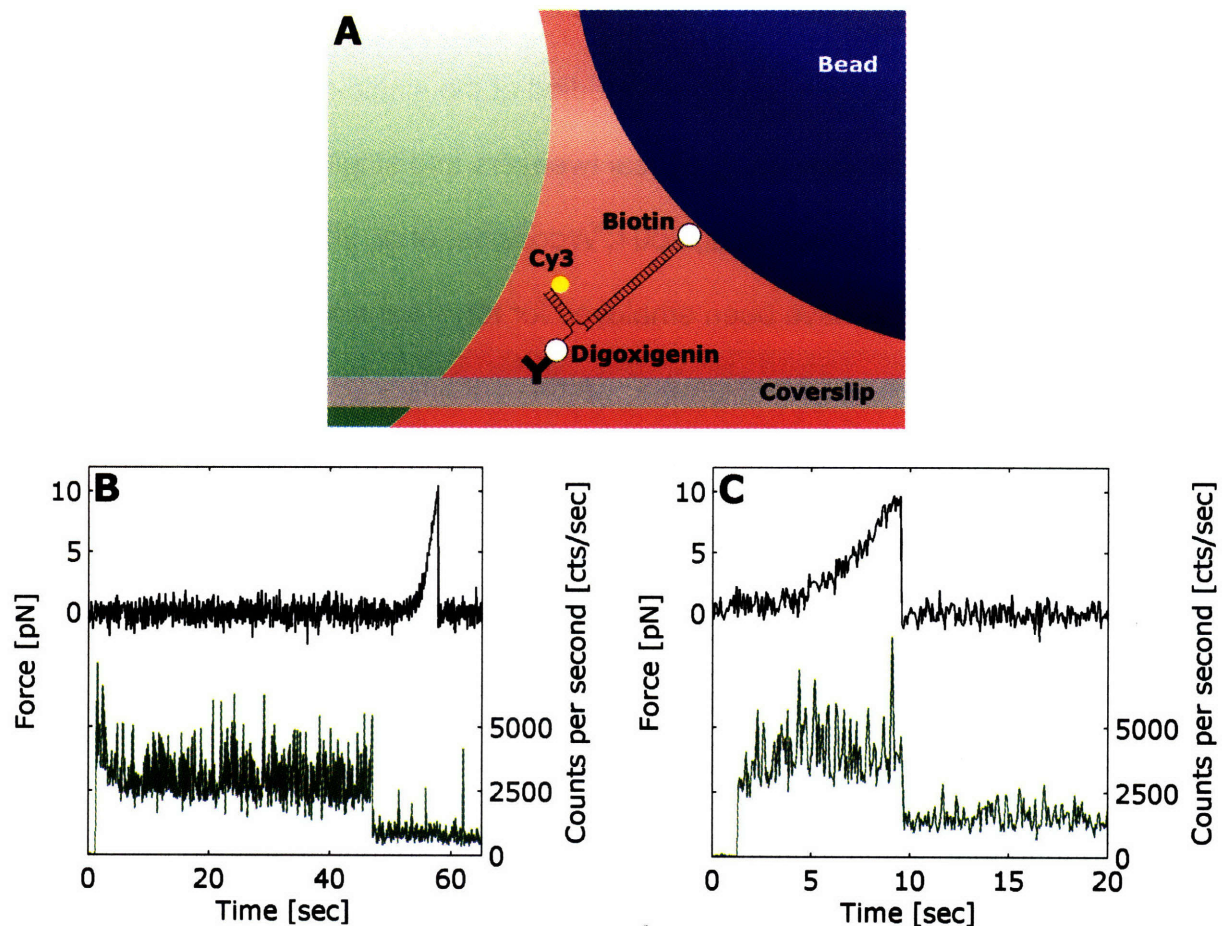


Figure 2.4 Combined measurement using the interlaced modulation technique. (A) Unzipping geometry for a 15-bp dsDNA system. It is attached on one end to a trapped bead via a biotin–streptavidin interaction and immobilized on the other end by means of a digoxigenin–antibody linkage. The 15-bp region of interest is labeled with a Cy3 fluorophore to confirm the location and timing of the unzipping mechanical event. (B) This system was exposed to OP radiation and its emission monitored until irreversibly photobleaching at ~45 s (green). Upon photobleaching, the dsDNA tether was loaded until rupture at ~10 pN (black). (C) Simultaneous trace of the force exerted on the dsDNA system (black) and the photon emission rate of the Cy3 fluorophore (green). The dsDNA system was loaded at a rate of 100 nm/s until a mechanical break occurs at ~10 pN (black). This event is correlated with a simultaneous drop to background levels in the Cy3 emission rate, corroborating the location of the break. The fluorescence excitation was shuttered for 1.5 s after position acquisition started.

Watching Conformational Changes with FRET

The mechanics of DNA hairpins have been studied at the single-molecule level and, thus, offer a benchmark for examining optical tweezers and single-molecule FRET in a combined arrangement (Liphardt, et al, 2001; Woodside, et al, 2006). Furthermore, alternate hairpin constructs have been employed for force-sensing applications (Shroff, et al, 2005). The structure used in this work, which contains a 20-base-pair hairpin stem, is flanked by noncomplimentary sequences annealed to oligonucleotides functionalized with the fluorophores Cy3 and Alexa 647 (Figure 2.5). Complexes exhibiting single-molecule FRET emission were mechanically loaded with the optical trap, effectively reducing the energetic barrier to hairpin opening. This unzipping transition, which occurs at a force of approximately 18 pN, is comparable to other similar measurements (Woodside, et al, 2006) and was reflected by the displacement of the bead toward the center of the trap. The conformational transition was accompanied by a simultaneous reduction in FRET efficiency caused by the increased physical separation of the Cy3 donor and the Alexa 647 acceptor, which indicated the precise location of the structural change caused by the translation of the mechanical load between the low-force (~6 pN) and high-force (~24 pN) states (Figure 2.5). The DNA complexes were moved through several transitions in a process corresponding to the reversible opening and closing of the hairpin segment, which demonstrated both the high degree of mechanical control and the simultaneous reporting by FRET emission. Furthermore, in the representative trace, single-step photobleaching of the donor after approximately 65 s verified the single-molecule measurement.

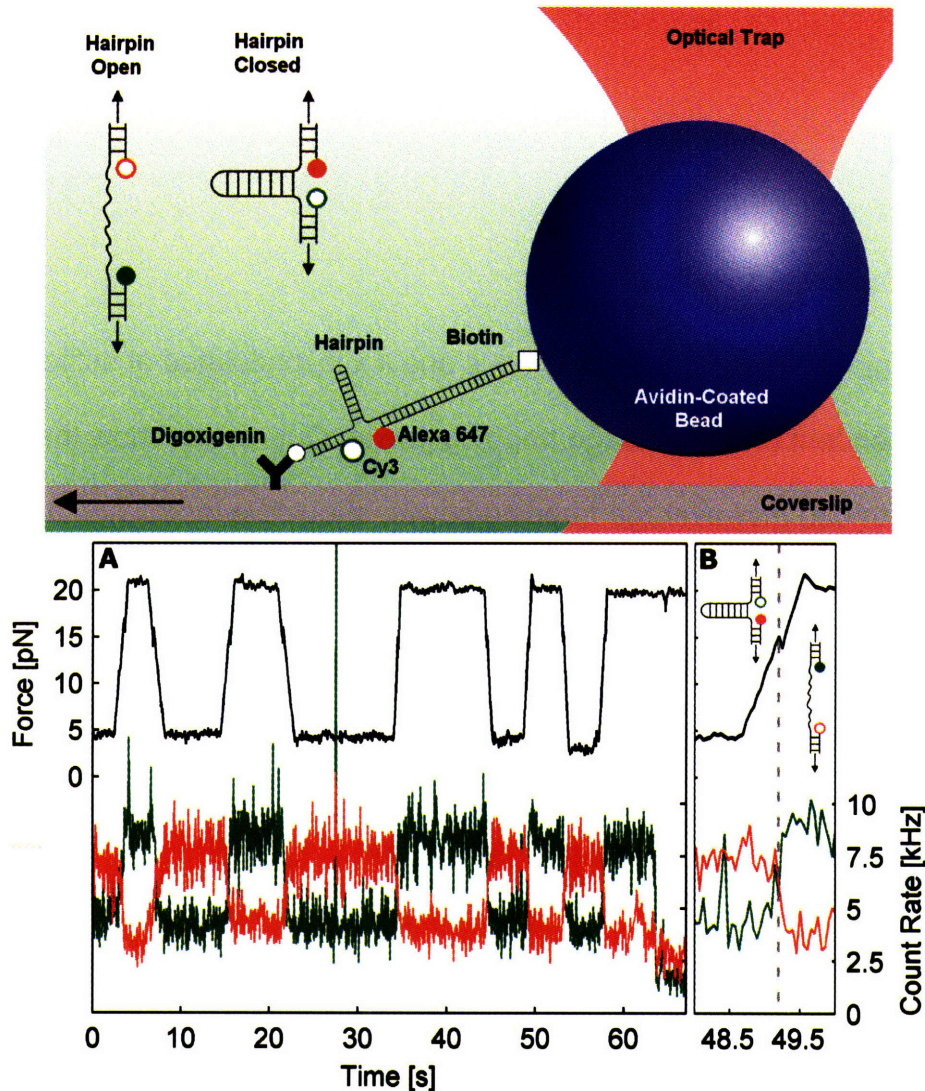


Figure 2.5 Watching force-induced conformational changes with FRET. (top) Experimental assay design. DNA hairpin complexes, labeled with opposing Cy3 and Alexa 647 fluorophores, were mechanically loaded by translating the coverslip, as the position of the trapped bead and the emission of the fluorophores were simultaneously monitored. The optical trap and the evanescent fluorescence-excitation field are depicted in the background in red and green, respectively. The inset cartoons show detail of the hairpin conformational change and the expected fluorophore emission (filled circles). (bottom) Mechanically induced conformational changes monitored with FRET spectroscopy. (A) A DNA hairpin was manipulated with optical tweezers between open or closed conformational states (black) that transition at loads of approximately 18 pN. The state of the hairpin was revealed by FRET between the donor Cy3 (green) and the acceptor Alexa 647 (red). The donor photobleaches at approximately 65 s, confirming that a single FRET pair was monitored. (B) Detail of a single hairpin opening transition accompanied by a simultaneous change in FRET, as highlighted by the gray dashed line. The inset cartoons depict the state of the hairpin.

Discussion

Trap Stiffness and Modulation

A modulated trap can resemble a continuous one if it is modulated at sufficiently high frequency, dependent on the average trapping power. Our results show that a strong trap, formed with 480 mW average trapping power, should be modulated at a frequency of at least 50 kHz, whereas a weaker trap, formed with 60 mW, can be modulated with frequencies as low as 10 kHz while still maintaining trap stiffness (Figure 2.2). This was further confirmed by fits to a simple exponential model and the resulting linear relationship between the characteristic modulation frequencies and trapping power. For a modulation frequency of 50 kHz, the trap is off for a duration of 10 ms, giving a bead with a diffusivity of $4.36 \times 10^{-13} \text{ m}^2 \text{ s}^{-1}$ enough time to diffuse $\sim 4 \text{ nm}$ away from the center of the trap, well within the average signal noise of a relatively weak optical trap. However, for fine measurements with position resolution on the order of 1 nm, such as those required for the resolution of molecular conformational changes and protein folding and unfolding (Kellermayer, et al, 1997; Rief, et al, 1997), the optical trap must be modulated at higher frequencies to minimize diffusional noise. We further validated this technique under a Stokes drag of 10 pN to monitor the effect of modulation on the position bead when it is subject to external loads. Such measurements confirmed that for sufficiently high frequencies the effects of modulation disappear, even when the bead is driven away from the center of the trap (results not shown).

Although these results suggest that the integrity of the trap can be completely recovered at high modulation frequencies, there are practical upper limits on the frequency at which modulation can occur. Acoustic modulation is limited by both the speed of sound in the AOD medium (4.2 mm/ μ s) and the diameter of the laser (\sim 2.5 mm), which in our system results in a maximum modulation frequency of \sim 80 kHz. This frequency is appropriate to modulate a trap formed with up to 400 mW of trapping power and characterized with a stiffness up to 0.4 pN/nm. Higher modulation frequencies can be reached by minimizing the diameter of the laser at the AOD location, employing AOD crystal materials that inherently provide higher sound velocities, or implementing electronic modulation techniques such as those used in telecommunications applications or for multiple color fluorescence measurements (Kapanidis, et al, 2005). Though such arrangements will further extend the versatility of this technique, our configuration is suitable for the types of experiments that are commonly approached with optical tweezers force spectroscopy.

Trap-Dependent Photobleaching Reduction

Trap-dependent photobleaching was observed when Cy3 fluorophores were simultaneously irradiated with the fluorescence excitation and trapping beams modulated IP. At the single molecule scale, Cy3 was irreversibly photobleached over an order of magnitude faster than when exposed to the NT condition (Figure 2.3). These results are in agreement with previous observations suggesting that the absorption of 1064 nm photons by molecules already in the first excited state can lead to a pathway that accelerates photodestruction (van Dijk, et al, 2004).

Our simple solution avoids populating these destructive states by allowing excited Cy3 molecules to return to the ground state before exposing the dye of interest to the high infrared photon flux of the trap. This technique significantly reduces destructive photobleaching effects by alternately modulating the fluorescence excitation and optical trapping lasers, the OP condition, resulting in a 20-fold longevity improvement over IP radiation (Figure 3). Despite this improvement, which extends the characteristic longevity of single Cy3 dyes to >30 s, fluorophore longevity remains shorter than that measured in the absence of a trapping laser, suggesting that the lower energy radiation can still cause some photodestruction. Although the mechanism of this additional photobleaching pathway is unknown, it is possible that it may arise from two-photon excitation (So, et al, 2000), the detection of which is beyond the sensitivity of our instrument for detecting single molecules. Even though there is preliminary evidence against it (van Dijk, et al, 2004), this scenario requires further investigation. Nevertheless, by alternately modulating the two beams, the major pathway for trap-dependent photobleaching is effectively eliminated, allowing IOFF to become feasible. Furthermore, this technique can be readily extended to single molecule experiments using other common dyes, such as Alexa 488, green fluorescent protein, and fluorescent resonance energy transfer pairs.

Modulation, Optical Tweezers, and Single Molecule Fluorescence

We have successfully presented a method for efficiently combining single molecule fluorescence and optical tweezers into a single, functional instrument without sacrificing

the capabilities of either technique. The effectiveness of this arrangement was demonstrated by mechanically unzipping a 15-bp dsDNA overhang model system and monitoring the event through the emission of a strategically placed Cy3 dye. This combination of force measurement and fluorescence emission provides solid evidence for the location and nature of the mechanical observations, as fluorescence signatures and force magnitudes differ for other types of breaks (Lang, et al, 2004). In addition, we report an unzipping force of ~ 10 pN for our 15-bp dsDNA system, which is in agreement with previously reported values for a similar system (Lang, et al, 2003; Lang, et al, 2004).

Though similar results have been presented with an analogous system (Lang, et al, 2003; Lang, et al, 2004), the benefits of our IOFF technique are necessary for combined measurements using common single molecule fluorophores. The most popular of these dyes, including Cy3, are characterized by a high quantum yield and extinction coefficient but are highly susceptible to the trap-induced photobleaching effects that are dramatically reduced by our approach. This result also improves assay development feasibility, a significant hurdle in single molecule research, for the investigation of molecular motor systems that have been independently approached with optical tweezers (Nishiyama, et al, 2002; Veigel, et al, 2005), single molecule fluorescence (Gordon, et al, 2004; Warshaw, et al, 2005; Yildiz, et al, 2004), or other methods (Reck-Peterson and Vale, 2004; Tolic-Norrelykke, et al, 2004). Such tools can now be simultaneously combined to elucidate the mechanochemical cycles governing the motion of these systems (Block, et al, 2003; Schnitzer and Block, 1995; Tokunaga, et al,

1997) and to study real-time force-induced conformational changes (Chigae, et al, 2003). In addition, this technique reduces the requirement of a highly efficient trap, allowing experiments involving optical tweezers to take place deep into solution, where they could be coupled with prism-side total internal reflection and other techniques. Furthermore, IOFF can be used to study protein folding and protein–protein and protein–DNA interactions and to monitor the formation of complex structures at the cellular level in response to external force (Galbraith, et al, 2002).

The combination of optical-tweezers force microscopy and single-molecule FRET detection perhaps represents an even more significant advance, especially for measuring the effects of structural changes on molecular function in a single molecule. By mechanically altering the conformational energy landscape, we actively induced a structural rearrangement pinpointed by strategically placed fluorescence labels. With minor modifications to existing assays, this approach can be extended beyond this model system to provide important new insight into the localized effects of mechanical force in biomolecular systems. For example, this combined technique can be adapted to monitor the intermolecular processes involved in the formation of a mechanically loaded protein complex (Cecconi, et al, 2005), the effects of mechanical deformation on single-enzyme catalysis (Chen, et al, 2003), or the intramolecular movements involved in biological-motor motility (Blanchard, et al, 2004; Block, et al, 2003). In addition, the presence of quantized single molecule fluorescence signals can provide unambiguous verification of the size and location of a mechanical event, a critical tool for the design of often complex single-molecule assays. The new perspective that arises from this ability to physically deform single molecules while simultaneously measuring structural

changes will allow the design of novel force-sensing molecules and will permit a new class of experiments for probing the interrelationship between molecular structure and biochemical function.

We have demonstrated the significant reduction of trap dependent photobleaching by alternately modulating fluorescence excitation and optical trapping lasers, showing a 20-fold improvement in Cy3 longevity at the single molecule level. In addition, we have successfully applied the combination of these two techniques to the fluorescence-reported unzipping of a short segment of dsDNA and opening and closing of a DNA hairpin. These applications, in which the fluorophore is held directly over the highest photon flux trapping region, suggest the broad versatility of this combined instrument. Such a seamless integration of single molecule fluorescence and optical tweezers force spectroscopy can be implemented through our temporal innovation with other common single molecule dyes in a wide range of molecular configurations for the exploration of the effects of mechanical force in biological systems.

Chapter III

Using Single Molecule Fluorescence to Probe the ClpX-Substrate Interaction

Abstract

Protein integrity inside cells is maintained by proteolytic machines capable of recognizing and engaging substrates targeted for destruction. In *E. coli*, one such protease, ClpXP, is composed of the ClpX ATPase and the ClpP peptidase, which are responsible for unfolding and denaturing substrates, respectively. Since the mechanisms by which ClpX achieves its function are poorly understood, here we present the first optical tweezers-based assay to directly and quantitatively measure the interaction between ClpX and its substrates. GFP-I27-ssrA substrates, which can be pre-engaged to ClpX in the presence of ATP γ S, were labeled with Cy3 to monitor the time necessitated by individual enzymes to unfold and translocate GFP. Using a microfluidic setup to quickly replace nucleotides in the assay buffer and a fluorescence excitation modulation technique that extended Cy3's longevity to about 95 s, ClpX was found capable of unfolding and translocating each GFP with a characteristic time constant of 22 s in the presence of 1 mM ATP. This measurement is more than 8 times faster than previously observed in bulk experiments clouded by substrate binding and unbinding.

This rate decreased to approximately 17 and 14 s as the concentration of ATP was reduced to 10 μ M or completely removed, respectively. This suggests that the pre-engaged substrate will dissociate from the enzyme at sufficiently low nucleotide concentrations, a phenomenon observed for ATP γ S as well. The single molecule fluorescence assay presented in this report can be easily modified to further test the mechanistic behavior of ClpX and a host of other enzymes to gain a better understanding of proteolytic machinery.

Introduction

Members of the AAA+ (ATPases associated with diverse cellular activities plus) superfamily of proteins play crucial roles in nearly every major cellular process including protein folding, membrane trafficking, cytoskeletal regulation, organelle biogenesis, DNA replication, intracellular motility, differentiation, and mitosis (Alberts, 1998; Dougan, et al, 2002; Neuwald, et al, 1999; Vale, 2000). AAA+ proteins also play an important role in protein unfolding, which can lead to the transport of proteins across membranes or to protein degradation (Alberts, 2002). In *E. coli*, one such ATPase, the bacterial protein ClpX, helps to maintain protein integrity by engaging substrates, denaturing or unfolding them by a process that is believed to be mechanical in nature, and ultimately translocating them into the cavity of the ClpP peptidase for irreversible proteolysis (Alberts, 2002; Langer, 2000; Sauer, et al, 2004). Many studies have attempted to elucidate the mechanistic details of these events, but still many questions remain. In this report we develop a single molecule fluorescence assay to measure the kinetics of unfolding and translocation of substrates already engaged to ClpX.

An active ClpX ATPase is composed of six identical monomers that form a hexameric ring, with each ATP site located at the interface between two monomers. The bottom surface of the hexamer is characterized by six loops, one for each monomer, bearing the hydrophobic IGF tripeptide sequence, which allows for the coaxial stacking of ClpX to ClpP. The top of the hexamer has been implicated in the recognition and binding of substrates. Even though the key structural motifs and their roles in this interaction have not been completely characterized (Farrell, et al, 2007), ClpX is known to recognize at least 5 classes of degradation sequences (Flynn, et al, 2003). Of these, the eleven amino acid C-terminal ssrA tag (AANDENYALAA) has been extensively studied because it can transform any protein into a substrate (Burton, et al, 2001; Gottesman, et al, 1998; Kenniston, et al, 2003; Kenniston, et al, 2004; Kim, et al, 2000). ClpX has a weak affinity for ssrA-tagged substrates, on the order of 1 μ M, but, once engaged, it can denature them in an ATP-dependent fashion. In the absence of ClpP, substrates are simply translocated through ClpX's pore and released on the other side, where they can spontaneously refold (Singh, et al, 2000). The conformational changes undergone by ClpX in response to the binding and hydrolysis of ATP are not well understood, but mutations along ClpX's pore, a likely location for the generation of force leading to unfolding and translocation, seem to hinder its ability to engage substrates (Siddiqui, et al, 2004).

The rate at which ClpX unfolds substrates is dependent on a number of factors that include the concentration of nucleotide and substrate, the presence or absence of ClpP,

and the structural integrity of the substrate. ClpX appears to have similar affinities for ATP and ATP γ S, an ATP analog that is hydrolyzed about 25 times slower, and, like many other molecular motors, it exhibits a Michaelis-Menten dependence on ATP concentration (Burton, et al, 2003; Hersch, et al, 2005). Nevertheless, some substrates, such as GFP, cannot be unfolded by ClpX in the presence of saturating levels of ATP γ S (Burton, et al, 2003). A Michaelis-Menten relation is also observed for increasing substrate concentrations at saturating ATP levels (Burton, et al, 2003; Kenniston, et al, 2003; Kenniston, et al, 2004). However, the structural integrity of substrates has been observed to influence the rate at which they are denatured, with increasing local stabilities, not global, appearing to require longer degradation times and larger consumptions of ATP (Kenniston, et al, 2003; Kenniston, et al, 2004). Finally, increasing amounts of ClpP decrease the rate at which ATP is hydrolyzed by ClpX, suggesting that it helps to stabilize the ATPase, even though the affinity between ClpX and ClpP is substrate dependent (Joshi, et al, 2004). ClpP has also been observed to increase the rates at which ClpX unfolds substrates by a factor of three for GFP-ssrA (Martin, et al, 2007).

Here we use total internal reflection fluorescence microscopy to measure the interaction of individual ClpX hexamers with GFP substrates that have been labeled with a Cy3 fluorophore on their N-terminal. In fact, the substrate consists of GFP-I27-ssrA, but the I27 mutant employed can be unfolded by ClpX in the presence of ATP γ S, leaving the GFP already engaged to the enzyme for immediate denaturation in the presence of ATP. This is the first application of single molecule techniques to the characterization of

the ClpX machinery. Single molecule fluorescence has been applied extensively to measure the properties of molecular motors (Funatsu, et al, 1995; Pierce, et al, 1997; Warshaw, et al, 2005) because they allow for the detection of nonequilibrium behavior under equilibrium conditions. Furthermore, single molecule techniques are capable of revealing heterogeneities that are commonly averaged out or hidden in bulk approaches, offering a distinct advantage over previous experiments.

Materials and Methods

ClpX trimers and substrates were expressed and purified as described elsewhere (Martin, et al, 2005). In order to facilitate the immobilization of ClpX hexamers, a F270C mutation introduced in the IGF loop of the first ClpX monomer of each trimer was biotinylated via maleimide chemistry (Pierce). Similarly, the substrates contained an N-terminal cysteine that was labeled with a Cy3 maleimide according to the manufacturer's instructions (GE Healthcare).

Flow cells holding a volume of approximately 10 μ L were made out of a custom PDMS channel and an etched glass coverslip. After baking the flow cells for 30 min at 80 $^{\circ}$ C to seal the PDMS-glass interface, they were filled with 0.1 mg/mL streptavidin in PBT (100 mM phosphate buffer, pH 7.5, 0.1% Tween). Nonspecific binding to the glass surface was reduced by flowing 100 μ L of 1 mg/mL casein in PBT prior to immobilizing 20 μ L of 100 nM bClpX in the presence of 1 mM ATP γ S in PD buffer (25 mM HEPES, pH 7.6, 100 mM KCl, 10 mM MgCl₂, 10% glycerol). 20 μ L of Cy3-labeled substrates diluted to an appropriate concentration in PD with 1 mM ATP γ S were then allowed to engage the

immobilized bClpX. In the steps outlined above, a vacuum manifold was used to flow the solution through the flow cells and all incubations took place in humidity chambers at room temperature for 20 min. At this point, the flow cells were equipped with the appropriate tubing and mounted on the single molecule fluorescence platform. After identifying a suitable surface region for analysis, the flow cells were washed with 100 μ L of PD buffer containing an oxygen scavenging system (120 nM catalase, 25 mM β -D(+) glucose, 1.8 μ M glucose oxidase, 1% β -mercapto-ethanol, degassed for 30 minutes in a desiccator) and 1 mM of the appropriate nucleotide. In the case of ATP, a ATP regeneration system was added as well (2.5 mM creatine phosphate and 0.05 mg/mL creatine kinase). This washing step took on the order of 1.5 s and could be readily identified on the captured image sequence because background fluorescence resulting from unbound Cy3-labeled substrates was significantly reduced after washing.

The single molecule fluorescence instrumentation is described elsewhere (Brau, et al, 2006). Briefly, it consists of a heavily modified inverted microscope outfitted with objective-side total internal reflection fluorescence capabilities. The excitation laser, a 532 nm diode laser (World Star Tech), is guided off-axis into a 1.45 NA 100X objective (Nikon) via a dichroic mirror held in a filter cube set (Chroma Technology). In order to minimize photobleaching, the power delivered to the specimen plane was adjusted to 50 μ W with an acousto-optic deflector (AOD) that gates the excitation laser with a square wave set to 0.3 Hz and a 10% duty cycle. Fluorescence emission is collected through the objective and spectrally filtered with a long-pass filter before being imaged onto a EMCCD camera (Andor Technology). The camera is externally triggered such that it

only collects images of the specimen plane for the duration of the excitation laser pulse, 300 ms. The resulting series of images contained many single molecule spots corresponding to individual substrates bound to immobilized ClpX. These were then analyzed to determine the longevity of each fluorescence spot using custom MATLAB software similar to that employed in particle tracking microrheology applications (Mason, 2000; Mason, et al, 1997).

Results

Functionality of Biotinylated ClpX

In order to test the functionality of the biotinylated ClpX hexamers, an ATP consumption assay was performed as described elsewhere (Burton, et al, 2001; Norby, 1988). In the absence of substrate, 300 nM of wild type ClpX hexamers made from dimers of covalently linked trimers (Martin, et al, 2005) hydrolyze ATP at a basal rate of approximately 150 ATP per min (Figure 3.1), a measurement in agreement with another report (Martin, et al, 2007). The ATPase rate increases to approximately 225 ATP per min in the presence of 10 μ M of unlinked *ssrA* tag. Furthermore, in the presence of 10 μ M of *ssrA*-tagged GFP, the basal rate almost triples, indicating an increase in the energy required to denature and translocate a folded substrate. Similar ATPase rates (Figure 3.1) were observed for the hexamers made from ClpX trimers in which the IGF loop of the first monomer was biotinylated. This modification prevents ClpX from docking onto ClpP (results not shown), but it does not affect ClpX's ability to engage substrates as its basal ATPase rate increased in the presence of *ssrA* peptide and

tripled in the presence of GFP-ssrA. In order to indirectly measure the specificity of the biotinylation, 2 μM of free avidin was introduced into the reaction mix. Under this condition, the ATPase rates were not significantly affected for ssrA and GFP-ssrA, suggesting that the partially buried cysteines along the mouth of ClpX's pore (C169) were not biotinylated. However, preliminary experiments suggest that streptavidin slows down ClpX's ability to unfold substrates in the presence of a GroEL trap (results not shown).

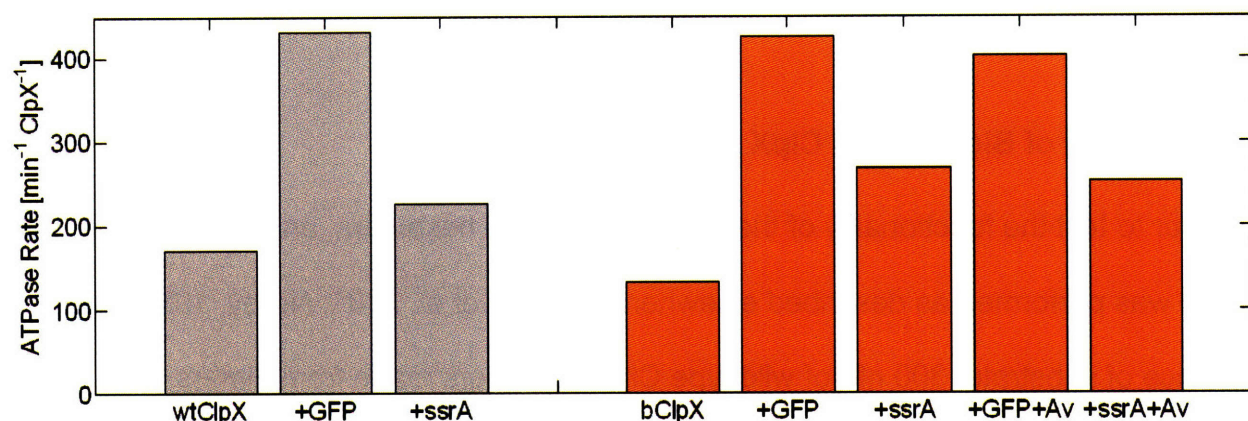


Figure 3.1 ATPase rates for wild type and biotinylated ClpX hexamers. The biotinylation of the IGF loops in ClpX does not affect its ability to denature and translocate substrate. In absence of substrate, wild type (left) and biotinylated (right) ClpX hexamers hydrolyze approximately 150 ATPs per min, but this rate increases to ~ 225 and 410 ATPs per min in the presence of ssrA peptides and ssrA-tagged GFPs, respectively. The addition of free avidin to the reaction does not affect the ATPase rate of the enzyme, suggesting that the biotinylation was specific to F270C mutation introduced in the IGF loop of the first ClpX monomer in each trimer.

Single Molecule Fluorescence Assay

The biotinylation of ClpX facilitates its immobilization on streptavidin-coated glass cover slips. This was confirmed by monitoring the ability of surface-bound biotinylated ClpX (bClpX) to engage substrates. Since the affinity of ClpX for ssrA tags is relatively weak,

GFP-ssrA dissociates from ClpX after short periods of time in the presence of ATPγS. In the presence of ATP, ClpX will only be engaged to GFP-ssrA for the duration of the unfolding and translocations events, which have been measured to take approximately 3 min in bulk (Martin, et al, 2007), but have not been characterized at the single molecule level. These problems were circumvented by employing a GFP-I27-ssrA fusion protein (Figure 3.2) as a substrate. This particular I27 domain of titin contains a V15P mutation that makes it easier to denature (Kenniston, et al, 2003). Furthermore, it can be unfolded by ClpX in the presence of ATPγS. This arrangement (Figure 3.2) allows for the synchronization of all surface-bound enzymes engaging substrate because GFP cannot be unfolded by ClpX in the presence of ATPγS (Burton, et al, 2003). In this configuration, the I27 is unfolded, but it remains threaded through ClpX's pore, which dramatically reduces the probability of dissociation of the substrate from the enzyme. Thus, this readies GFP for immediate denaturation in the presence of ATP (Figure 3.2).

As a fluorophore, GFP is very dim and photobleaches rather quickly. Thus, it is not suitable for single molecule fluorescence experimentation. Furthermore, it is not clear at which point GFP loses its fluorescence capabilities as it starts to become unfolded by ClpX. For these reasons, a cysteine was introduced into the N-terminus of GFP and labeled with a Cy3 fluorophore, which is exceptionally bright and stable and is commonly used in single molecule fluorescence experiments (Brau, et al, 2006; Funatsu, et al, 1995). Since the ssrA tag is a C-terminal degradation tag, the positioning of Cy3 requires that it is the last element of the substrate that comes into contact with

the pore of ClpX. Thus, Cy3 can be excited with a 532 nm laser and its fluorescence can be used to monitor the kinetics of substrate unfolding and translocation.

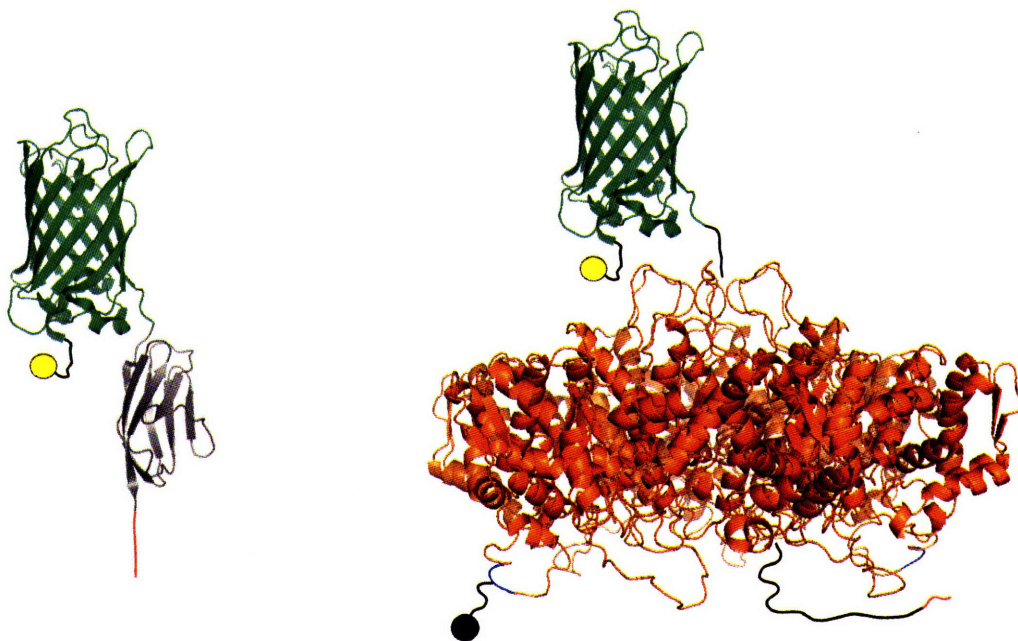


Figure 3.2 Single molecule fluorescence assay for ClpX. (a) The N-terminus of the GFP-I27-ssrA substrate was labeled with a Cy3 fluorophore (Cy3: yellow, GFP: green, I27: gray, ssrA tag: red) (b) Schematic of the proposed assay. In the presence of ATP γ S, ClpX (orange) can denature I27, but not GFP, which functions as a mechanical stop and is left ready for immediate denaturation in the presence of ATP. The unfolded I27 polypeptide is threaded through ClpX's pore and exits on the bottom of the enzyme. The mutant ICF tripeptide sequence in two of the ClpX monomers is highlighted in blue, with one of them biotinylated (black) to facilitate the immobilization of the enzyme on a streptavidin-coated surface (not shown).

Fluorescence Detection and Longevity

In the presence of saturating levels of ATP γ S, the single molecule fluorescence assay described above results in multiple individual fluorescent spots per field of view corresponding to specific ClpX-substrate interactions immobilized on a surface (Figure

3.3). After capturing digital images of the surfaces, a custom software algorithm can be used to quantitatively identify them, determine their relative locations (Figure 3.3), and track them over time. This information can then be used to determine the longevity of the Cy3 fluorophores, which will indicate the time required by ClpX to unfold and translocate GFP in the presence of ATP.

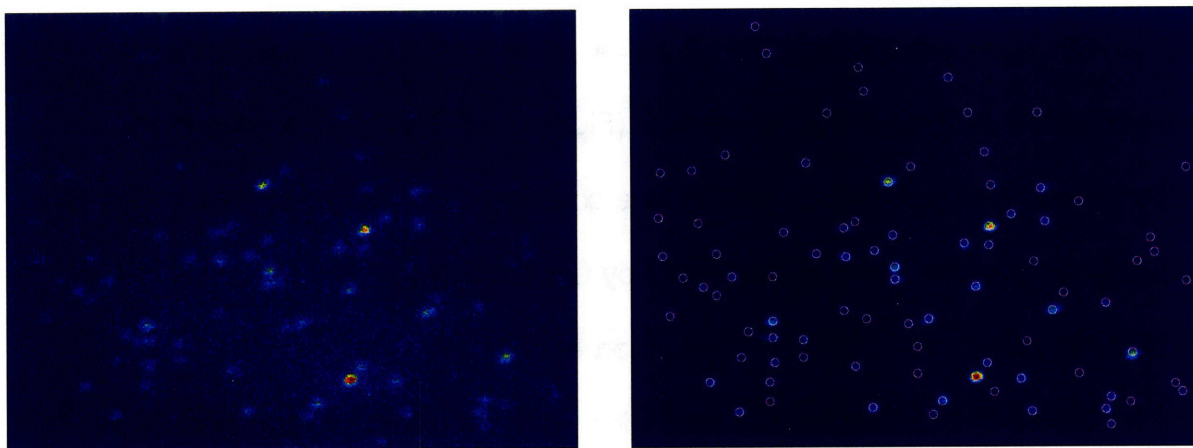


Figure 3.3 Detecting individual fluorescence molecules. (left) Representative image of a surface with immobilized ClpX hexamers engaging Cy3-labeled GFP-I27-ssrA. Each spot corresponds to an interaction between a single biotinylated ClpX hexamer and a single Cy3-labeled substrate. (right) Custom software was used to process the image on the left. The software automatically identifies the single molecule fluorescence spots (white circles) and records their location. If a series of images are analyzed, this information can be used to track the longevity of Cy3 and measure the time required by ClpX to unfold and translocate its substrate.

The longevity of individual Cy3 molecules was measured by immobilizing the labeled substrate, which has a hexahistidine tag proximal to the ssrA tag, on a glass coverslip surface upon which anti-His antibodies had been nonspecifically absorbed. Individual fluorescent spots were simultaneously tracked over time. Since the his tag-antibody interaction is strong, with an affinity on the order of 1 nM, minimal substrate dissociation

was observed over the time scale of these experiments (results not shown). This indicates that fluorescent signal loss is due to photobleaching events of individual Cy3 fluorophores. To minimize the rates at which Cy3 photobleaches, an oxygen scavenging system was employed (see Materials and Methods) and the fluorescence excitation laser power was tuned to 50 μW , the lowest power at which individual Cy3 fluorophores could be readily identified (Figure 3.3). With this arrangement, 67% of all fluorescent spots ($n = 479$) photobleached within a period of 45 s, with the remaining fluorophores surviving for the entirety of the experiment (Figure 3.4). The fluorophores that photobleached seemed to do so with a time constant on the order of 10 s, which is much shorter than the 3 min necessitated by ClpX to unfold GFP, as measured in bulk experiments (Martin, et al, 2007). Thus, in order to extend the longevity of Cy3, an algorithm in which the fluorescence excitation laser was modulated or gated was adopted. In this arrangement, which is similar to one employed to combine optical tweezers and single molecule fluorescence capabilities (Brau, et al, 2006; Tarsa, et al, 2007), the fluorescence excitation laser irradiates the sample with a 300 ms pulse while the camera simultaneously captures an image of the fluorescent surface. In between laser pulses, there is an adjustable dead time period in which the fluorescence excitation laser is shuttered and the camera is idled. Using a 3 s dead period significantly extends the longevity of fluorophores, and, over a 160 s experiment, only 41% ($n = 554$) of the fluorophores photobleach (Figure 3.4). This represents a 75% improvement on the number of surviving fluorophores, 59% versus 33%, over the continuous excitation arrangement even though the fluorophores were exposed to the excitation laser for the same amount of total time. Thus, the modulating arrangement

employed here can provide a large enough separation of time scales over which kinetic measurements can be made with minimal signal contamination coming from photobleaching.

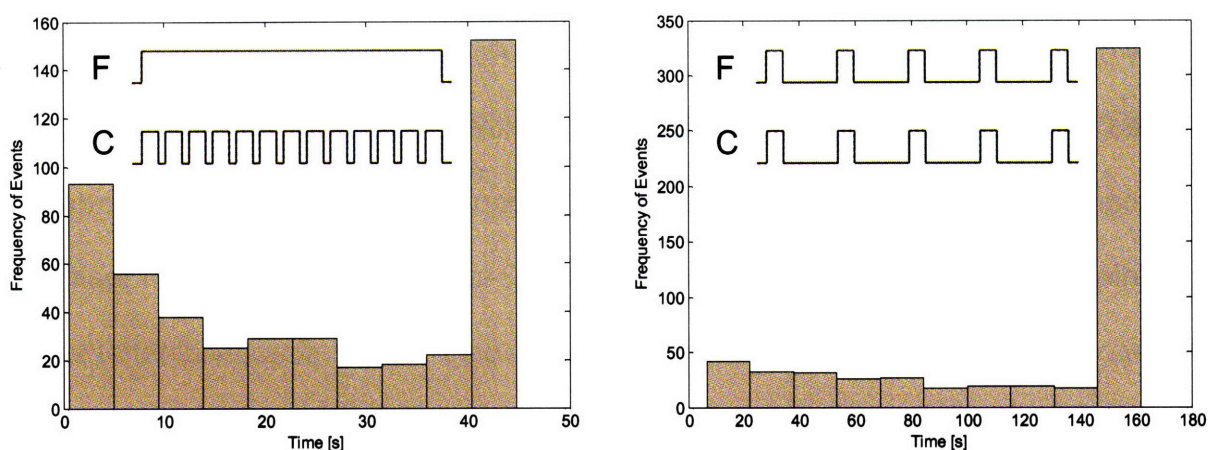


Figure 3.4 Reducing the photobleaching rate of Cy3 labeled substrates immobilized on anti-His antibody coated surfaces. (left) When Cy3 fluorophores were exposed to a continuous laser excitation, 67% ($n = 479$) of them photobleached within 45 s. (inset) The samples was exposed to continuous fluorescence laser excitation (F) and images of the surface were sequentially taken with the EMCCD camera (C) for 300 ms, with a small delay in between images. (right) When the fluorophores are exposed to an arrangement in which the fluorescence excitation laser is modulated, only 41% of the Cy3 fluorophores photobleach over a time period of 160 s. (inset) The modulation consists of shuttering the fluorescence excitation laser (F) off for 3 s and shuttering it on for 300 ms. The EMCCD camera (C) is synchronized so that it takes images with every fluorescence excitation laser pulse. In both cases continuous and modulated cases, the Cy3 fluorophores were exposed to the fluorescence excitation laser for same amount of total time.

Buffer Exchange

Buffer exchange in conventional flow cells made out of a glass coverslip and a microscope slide is tedious and slow. For these reasons, a PDMS-based microfluidic channel was manufactured and mounted on an etched coverslip. The resulting flow cell holds approximately 10 μL of volume and is equipped with inlet and outlet holes that can

be used to flow through the different components of the assay. Once the assay is prepared, tubing can be attached to the holes to facilitate and expedite the exchange of the washing buffer. Prior to attachment, the tubing on the inlet port is filled with buffer and a syringe secured on its other end can be used to push the washing buffer through the flow cell quickly, without disturbing the sample. As an example, a flow cell was prepared with a high concentration of Cy3-labeled streptavidin, which provided a strong fluorescent signal (Figure 3.5). After a brief incubation, the buffer in the syringe attached to the inlet tubing was used to wash the excess Cy3-labeled streptavidin from the flow cell, removing most of the free material and leaving only labeled streptavidin that was nonspecifically adhered to the glass surface (Figure 3.5). This dramatic reduction in fluorescent signal occurs in less than two seconds (Figure 3.5), a time scale that is much faster than the rate at which Cy3 photobleaches when the modulation technique is employed (Figure 3.4). Furthermore, this technique facilitates the fast substitution of the ATP γ S used in the preparation of the assay with ATP, allowing for a more precise measurement of the time required by ClpX to unfold and translocate GFP.

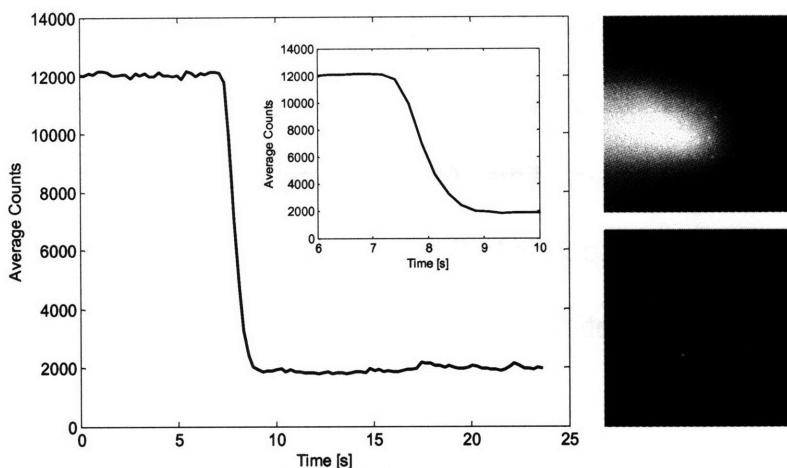


Figure 3.5 Buffer exchange in a PDMS-based flow cell. (left) A PDMS-based flow cell containing Cy3-labeled streptavidin was perfused with washing buffer and the fluorescent counts of the field of view were monitored over time. Prior to washing, the EMCCD camera detected about 12,000 counts, but immediately after washing, the counts dropped to a background level of approximately 2,000. (inset) Further inspection of the washing process reveals that it occurs in less than 2 s. (top right) Image of the flow cell filled with Cy3-labeled streptavidin, prior to washing. (bottom right) Image of the flow cell after washing shows minimal fluorescence corresponding to nonspecifically adhered Cy3-labeled streptavidin.

Nucleotide Dependence

Using the modulating and microfluidic schemes described above, single molecule fluorescence experiments were carried out to measure the time necessary for ClpX to unfold and translocate pre-engaged GFP substrates. Measurements of individual fluorescence spots were recorded, built into a histogram for each experimental condition, and fitted to a single exponential decay function to extract information about the characteristic time scales. At the end of each movie, which lasted about 5 min, there were spots that were still visible in the field of view. Since it is not known whether these spots were specifically bound to ClpX, they were excluded from the fits and the analysis. Nevertheless, they are still presented in the histograms below as the bins after

300 s and sometimes account for 25% of all total spots analyzed. Some of the histograms contain multiple bins after 300 s because the different movies taken for each condition did not start at the same time. After capture, all movies were synchronized such that that time zero corresponds to the first image immediately after washing with fresh buffer and excess nucleotide.

Results show that in the presence of 1 mM ATP γ S, ClpX can interact with substrates for long periods of time. However, there is a finite period over which measurements can be done because the Cy3-labeled substrates photobleach with a time constant of approximately 95 s ($R^2 = 0.80$, $n = 310$) (Figure 3.6). In order to test the possibility of whether the loss in signal is indicative of substrate release, the same experiment was carried out for Cy3-labeled substrates immobilized on anti-His antibody coated surfaces ($n = 738$). In this experiment, the fluorescence signal was lost at a rate of about 92 s ($R^2 = 0.93$), in close agreement with the rate observed for 1 mM ATP γ S (results not shown). Since the affinity between hexahistidine motifs and anti-His antibodies is on the order of 1 nM, the dissociation rate between the two is expected to be in the minutes to hours scale. Even though fluorescence loss due to dissociation was observed in experiments over longer time periods, this suggests that any fluorescence loss during the 5 min experiment is mostly due to photobleaching. The same reasoning is applied to the ClpX-substrate interaction, which has not been characterized for a pre-engaged substrate. However, it is known from bulk experiments that ClpX and *ssrA*-tagged substrates have a Michaelis-Menten constant and an affinity on the order of 1 μ M (Kenniston, et al,

2003), which provides a lower bound estimate on the strength of the interaction for pre-engaged substrates.

Interestingly, the rate at which fluorescence spots disappeared increased to approximately 66 s when the concentration of ATPyS was lowered to 100 μM ($R^2 = 0.85$, $n = 169$) (Figure 5.6), suggesting that the pre-engaged substrate is starting to dissociate. To further explore whether pre-engaged substrates can indeed dissociate from ClpX, the experiments were carried out in the complete absence of nucleotide. Under this condition ($n = 274$), substrates released from ClpX with a time constant of approximately 14 s (Figure 5.6). It is unclear whether the ClpX hexameric ring opens at low nucleotide concentrations or whether there simply isn't enough nucleotide to help ClpX maintain a grip on its substrates. Nevertheless, it is clear that low concentrations of nucleotide lead to the dissociation of substrates from ClpX.

In order to measure the kinetics of unfolding and translocation, the pre-engaged ClpX-substrate interaction was exposed to different concentrations of ATP. Interestingly, there was not much variation between rates at which the Cy3 substrates disappeared in this case. Experiments carried out in the presence of 1 mM, 200 μM , and 100 μM revealed fluorescence decay rates of 21.29, 21.29, and 22.19 s, respectively (Figure 5.7). However, when the ATP concentration was decreased to 10 μM , the fluorescence decrease rate accelerated to 17.16 s (Figure 5.7), perhaps suggesting that some dissociation was taking place. In addition, the histogram for the ATP conditions show that approximately only 10% of the labeled substrates remain on the specimen place at

the end of the movie sets. This contrasts the histograms for the ATP γ S and no ATP conditions (Figure 5.6), which showed about 25% of the substrates remaining at time periods longer than 300 s. The ATP histograms are also better described by an exponential decay function, as their fits all exhibit a $R^2 > 0.94$ (Table 3.1).

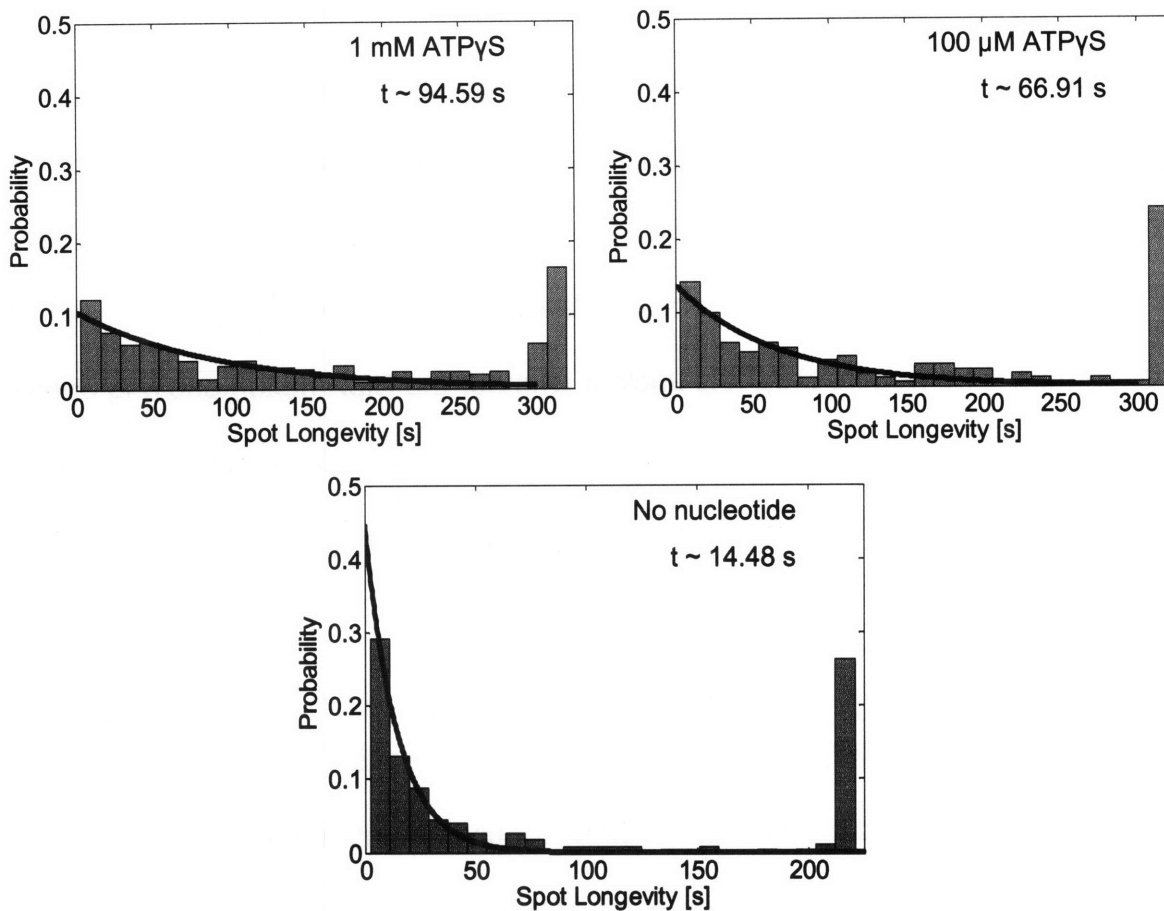


Figure 3.6 Single molecule fluorescence decay rates for the ClpX-substrate interaction in the presence of ATP γ S. At a ATP γ S concentration of 1 mM, the fluorescence spots disappear with characteristic time constants of 95 s (top left). This rate matches closely with the rate observed for labeled substrates immobilized on anti-His antibody coated surfaces, suggesting that minimal dissociation is occurring. However, the dissociation rate increases to 66 s as the nucleotide concentration is decreased to 100 μ M ATP γ S (top right). In the complete absence of nucleotide, the fluorescence spots dissociate with a rate of 14 s (bottom).

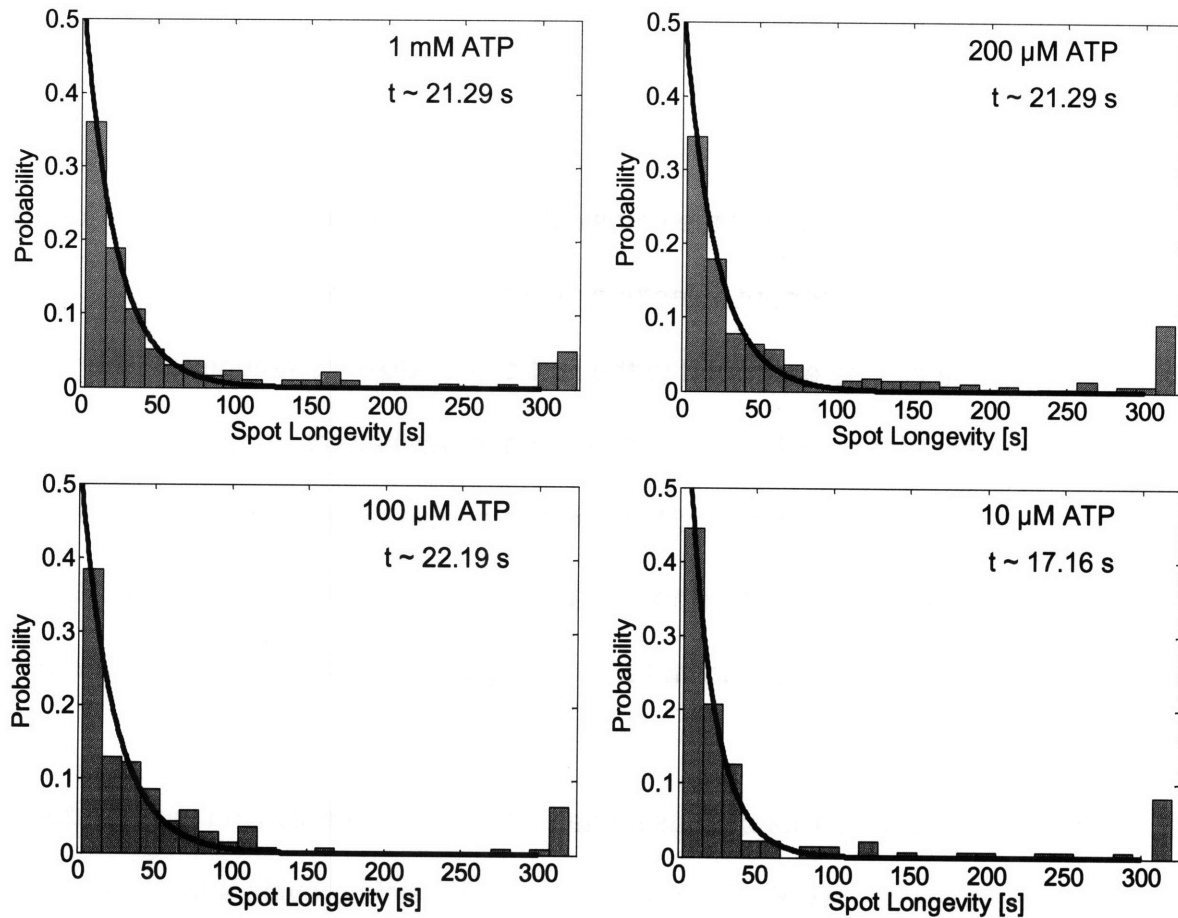


Figure 3.7 Single molecule fluorescence decay rates for the ClpX-substrate interaction in the presence of ATP. At ATP concentrations of 1 mM (top left), 200 μ M (top right), 100 μ M (bottom left), and 10 μ M (bottom right) the fluorescence spots disappear with characteristic time constants of approximately 21, 21, 22, and 17 s, respectively.

	Time Constant [s]	R ²	n
1 mM ATPyS	94.5947	0.8006	310
100 μ M ATPyS	66.6094	0.8453	169
1 mM ATP	21.2966	0.9932	503
200 μ M ATP	21.2976	0.9843	284
100 μ M ATP	21.1963	0.9439	138
10 μ M ATP	17.1618	0.9899	135
No Nucleotide	14.4847	0.984	274
anti-His ab	92.2856	0.93	738

Table 3.1 Summary of results for single molecule fluorescence decay rates for the ClpX-substrate interaction.

Discussion

In this chapter, we have introduced the first single molecule fluorescence assay for the ClpX ATPase. This is an important milestone as it opens the door for much experimentation that can be expanded to the rest of the AAA+ community. In the experiments presented here, ClpX was biotinylated to facilitate its immobilization on streptavidin-coated surfaces. This modification was shown to have negligible effects on ClpX's activity (Figure 3.1), although the preliminary experiments suggest that the presence of streptavidin can slow down its unfolding capabilities (results not shown).

GFP was chosen as a substrate because it has been well characterized in degradation experiments. Furthermore, GFP's fluorescent properties help provide a tremendous advantage for developing a single molecule assay because its binding can be readily observed. Nevertheless, GFP is a poor fluorophore, as it is very dim and photobleaches quickly. This problem was circumvented by labeling its N-terminal with a Cy3 fluorophore, one of the most popular and brightest single molecule dyes. Cy3 has been shown to last about 90 s when conjugated to nucleic acids (Brau, et al, 2006), while GFP usually photobleaches in a few seconds (results not shown). However, similar to other fluorophores (Panchuk-Voloshina, et al, 1999), Cy3's longevity was compromised upon conjugation to GFP. This problem, however, was remedied by the successful adoption a fluorescence excitation modulation technique (Figure 3.4). In addition to its superior photophysical properties, Cy3 also can be efficiently excited with a 532 nm laser line, a wavelength at which GFP minimally absorbs. Furthermore, if there is any

fluorescence being radiated by GFP, it can be easily filtered out because its emission peak is found at about 510 nm, while Cy3's is at 570 nm. Finally, since GFP loses its fluorescence capabilities as it is being unfolded, the strategic placement of Cy3 on its N-terminal allows for the monitoring of its complete unfolding and translocation by ClpX.

The results presented here suggest that ClpX is capable of unfolding and translocating substrates quicker than previously thought, with a characteristic time constant on the order of 22 s for pre-engaged GFP. Previous experiments had shown that ClpXP can unfold GFP-ssrA at a rate of approximately 60 s (Martin, et al, 2007), as determined by the irreversible loss of native fluorescence. However, ClpX takes about 180 s to unfold GFP-ssrA in the absence of ClpP (Martin, et al, 2007), a rate that is about 8 times slower than our measurements, which also account for the translocation of the unfolded substrate. Of course, the bulk measurement takes into account the binding and unbinding of the substrate to the enzyme, and the many failed attempts by the latter to actually unfold the former (Kenniston, et al, 2003), whereas our measurements monitor the unfolding and translocation of a pre-engaged substrate. As such, it is better to compare our results to single-turnover bulk measurements in which substrates are pre-engaged to ClpXP in the presence of ATPyS (Andreas Martin, personal communication). In this case, stop flow techniques are employed to quickly replace ATPyS with ATP before monitoring the degradation of a substrate. Their results show that ClpXP takes approximately 9 s to unfold and translocate one molecule of GFP-ssrA. Once again, assuming that ClpX's enzymatic behavior is three-fold slower in the absence of ClpP, we expect a rate of approximately 27 s, which is in agreement with

our single molecule results. The sources of the ~ 20% discrepancy between the single molecule results and the bulk ones are unclear, but they could arise from inactive enzymes in the solutions of the bulk experiments. These are present in the single molecule assay as well, but they are self selected out of the measurements by the nature of the experiments.

As described above, the unfolding and translocation rate for pre-engaged GFP-ssrA was measured to be approximately 22 s. This rate was insensitive to changes in ATP for up to a 10-fold dilution from 1 mM ATP. On the other hand, a ten-fold dilution of ATP γ S was enough to promote dissociation of the substrate from the enzyme. Perhaps, even though both ATP and ATP γ S have affinities on the order of 10 μ M, their hydrolysis rates play an important role in the enzyme's ability to hold on to its substrates. Since ATP γ S is hydrolyzed about 25 times slower than ATP, it makes sense for the integrity of the ClpX-substrate interaction to be affected at higher concentrations of ATP γ S than ATP.

It is well known that ClpX cannot unfold GFP in the presence of ATP γ S; thus, any loss of fluorescence signal in this case has to be interpreted as photobleaching or substrate dissociation from the enzyme. Our results show that the fluorescent decay rate of the substrate in the presence of 1 mM ATP γ S compares favorably to the photobleaching decay rate of substrates immobilized on surfaces coated with anti-His antibodies (Table 3.1). With photobleaching rates on the order of 95 s, this suggests that the rate at which substrate dissociation occurs is minimal at high concentrations of ATP γ S, although it

was observed to increase as the concentration of ATP γ S was lowered (Figure 3.6) (Table 3.1). In contrast, the rate of fluorescence decay remained constant at about 22 s for concentrations of ATP higher than 100 μ M. However, it was observed to increase to about 17 s for 10 μ M ATP, which suggests that some of the pre-engaged GFP-ssrA substrates are disengaging from ClpX. This is similar to the behavior observed for ATP γ S in which the substrate starts to dissociate from the enzyme once sufficiently low concentrations of nucleotide are reached.

The measurements presented in this report rely on the disappearance of a fluorescence signal to infer information about the behavior of the ClpX-substrate interaction. As such, it can be difficult to distinguish between the loss of fluorescence due to photobleaching from the loss of fluorescence due to unfolding, translocation, and release, which appear to occur at similar rates of 14 and 22 s in absence and presence of saturating concentrations of ATP. In order to test whether these two measurements are truly different, we have exposed pre-engaged substrates to ATP in the absence of Mg²⁺ and observed minimal fluorescent loss, suggesting that substrates remain engaged in the presence of ATP (results not shown). Since ATP cannot be hydrolyzed in the absence of Mg²⁺, this setup is being used to replace ATP γ S with ATP before any hydrolysis takes place to obtain a more accurate measurement of the unfolding and translocation rates. We are also developing a substrate that, once engaged via a I27 domain of titin, will present two sequential GFP molecules for ClpX to unfold and translocate. It is expected that the rate of fluorescence decay should double to approximately 45 s when this substrate is

employed, while the substrate release in rate in the absence of ATP remains the same. However, initial efforts have been derailed by nonspecific binding of this substrate to a variety of different blocking proteins.

Chapter IV

Using Optical Tweezers to Probe the ClpX-Substrate Interaction

Abstract

Protein integrity inside cells is maintained by proteolytic machines capable of recognizing and engaging substrates targeted for destruction. In *E. coli*, one such protease, ClpXP, is composed of the ClpX ATPase and the ClpP peptidase, which are responsible for unfolding and denaturing substrates, respectively. Since the mechanisms by which ClpX achieves its function are poorly understood, here we present the first optical tweezers-based assay to directly and quantitatively measure the interaction between ClpX and its substrates. Results show that ClpX is capable of exerting forces on its substrates that are minimally dependent on the nucleotide concentration, 1 mM or 1 μ M, or identity, ATP or ATP γ S. We measured rupture forces on the order of 55 pN for loading rates of about 18 pN/s and analyzed histograms of the probability density distributions of the rupture forces using two nonequilibrium kinetic models. Kinetic parameters estimated from both models are similar and suggest that the ClpX-substrate interaction has an intrinsic dissociation rate and a transition distance from the free-energy minimum to the rupture barrier on the order of 0.05 s⁻¹ and 0.25 nm, respectively. The uniformity of the results and lack of unfolding events or rupture

intermediates observed suggests that the weakest element in the probed interaction is the integrity of the ClpX hexameric ring. This underscores the importance of ClpP, which is known to stabilize ClpX. Nevertheless, the single molecule assay described above can be easily modified to test the processivity of ClpX and a host of other enzymes to gain a better understanding of proteolytic machinery.

Introduction

Protein integrity inside cells is maintained by a series of tightly regulated processes by which unwanted targets are removed or dismantled. In higher organisms, most of these events are carried out by the proteasome and the ubiquitination pathway, while in a bacterial cell, such as *E. coli*, proteolysis is carried out by different ATP-dependent proteases (Gottesman, 2003). These proteases, which are typically composed of a peptidase and a AAA+ (ATPases associated with diverse cellular activities plus) ATPase, function as molecular machines capable of destroying substrates that have been targeted for degradation. Both the peptidase and the ATPase play very different, but complementary, roles in this process; nevertheless, it appears that the ATPase is the workhorse of the complex. In addition to recognizing substrates, the ATPase is also responsible for their unfolding and translocation into the catalytic cavity of the peptidase, where irreversible degradation takes place. Thus, the peptidase is simply a passive bystander that waits for the ATPase to feed it substrates. The processes by which substrates are unfolded and translocated are very poorly understood, although they are believed to be mechanical in nature and to result from a series of conformational changes associated with the binding and hydrolysis of ATP. In this report we develop a

single molecule optical tweezers based assay in an attempt to measure the biophysical properties of the ClpX ATPase.

A functional ClpX ATPase, a member of the AAA+ superfamily of proteins, is composed of six identical monomers that form a hexameric ring, with each ATP site located at the interface between two monomers. The bottom surface of the hexamer is characterized by six loops, one for each monomer, bearing the hydrophobic IGF tripeptide sequence, which allows for the coaxial stacking of ClpX to the ClpP peptidase, a decaheptameric ring itself. On the other hand, the top of the hexamer has been implicated in the recognition and binding of substrates. Even though the key structural motifs and their roles in this interaction have not been completely characterized (Farrell, et al, 2007), ClpX is known to recognize at least 5 classes of degradation sequences (Flynn, et al, 2003). Of these, the eleven amino acid C-terminal ssrA tag (AANDENYALAA) has been extensively studied because it can transform any protein into a substrate (Burton, et al, 2001; Gottesman, et al, 1998; Kenniston, et al, 2003; Kenniston, et al, 2004; Kim, et al, 2000). ClpX has a weak affinity for ssrA-tagged substrates, on the order of 1 μ M, but, once engaged, it can denature them in an ATP-dependent fashion. In the absence of ClpP, substrates are simply translocated through ClpX's pore and released on the other side, where they can spontaneously refold (Singh, et al, 2000). The conformational changes undergone by ClpX in response to the binding and hydrolysis of ATP are not well understood, but mutations along ClpX's pore, a likely location for the generation of force leading to unfolding and translocation, seem to hinder its ability to engage substrates (Siddiqui, et al, 2004).

The rate at which ClpX unfolds substrates is dependent on a number of factors that include the concentration of nucleotide and substrate, the presence or absence of ClpP, and the structural integrity of the substrate. ClpX has an affinity of about 1 μM for ATP and ATP γ S, an ATP analog that is hydrolyzed about 25 times slower, and, like many other molecular motors, it exhibits a Michaelis-Menten dependence on ATP concentration (Burton, et al, 2003; Hersch, et al, 2005). Nevertheless, some substrates, like GFP, cannot be degraded in the presence of saturating levels of ATP γ S (Burton, et al, 2003). A Michaelis-Menten relation is also observed for increasing substrate concentrations at saturating ATP levels (Burton, et al, 2003; Kenniston, et al, 2003; Kenniston, et al, 2004). However, the structural integrity of substrates has been observed to influence the rate at which they are denatured, with increasing local stabilities, not global, appearing to require longer degradation times and larger consumptions of ATP (Kenniston, et al, 2003; Kenniston, et al, 2004). Finally, increasing amounts of ClpP decrease the rate at which ATP is hydrolyzed by ClpX, suggesting that it helps to stabilize the ATPase, even though the affinity between ClpX and ClpP is substrate dependent (Joshi, et al, 2004).

None of the above experiments have been able to address the question as to what forces ClpX is capable of exerting on its substrates. It is widely believed that this ATPase must be capable of applying loads of at least 100 pN, the forces observed to generally unfold I27 and GFP in AFM experiments (Dietz and Rief, 2004; Rief, et al, 1997). However, the pulling geometry in these experiments differs greatly from that

associated with ClpX because the forces applied with an AFM are biaxial. It is the equivalent of trying to pull a knot through a small hole versus trying to unravel the knot apart by pulling on its two ends. These two very different scenarios will undoubtedly result in different forces necessary to undo a knot or protein. To this end, here we use optical tweezers to measure the interaction between individual ClpX hexamers and its substrates. In order to achieve this, ClpX was biotinylated (Chapter III), immobilized on polystyrene beads, and tethered to a GFP-I27-ssrA construct anchored on a coverslip surface via a dsDNA segment. Results show that ClpX is capable of exerting loads of at least 50 pN on its substrates, at which point the hexameric ring seems to open and disengage from the substrate. Moreover, these loads seem to be independent on the nature and concentration of the nucleotide employed, suggesting that single ClpX subunits individually engage substrates even when multiple nucleotides are bound.

Materials and Methods

ClpX trimers and substrates were expressed and purified as described elsewhere (Martin, et al, 2005). In order to facilitate the immobilization of ClpX hexamers, a F270C mutation introduced in the IGF loop of the first ClpX monomer of each trimer was biotinylated using maleimide chemistry. Similarly, GFP-I27(V15P)-ssrA substrates containing an N-terminal cysteine were crosslinked to primary amines in one of the 5' ends of a 1010 bp segment of dsDNA using Sulfo-SMCC (Pierce), according to the manufacturer's instructions. The other 5' end of the dsDNA segment contains a biotin motif to facilitate its immobilization on streptavidin coated surfaces. The structural sequence of the tether complex is the following: biotin-dsDNA-GFP-I27-ssrA. For some

applications, the I27 domain of the tether was irreversibly unfolded by carboxymethylation of its internal cysteines in 2.5 M guanidine hydrochloride and 100 mM iodoacetic acid.

Flow cells were made by running two pieces of double-stick tape, separated by about 5 mm, along the short axis of a standard microscope slide and mounting an etched coverslip on them. After preparing the flow cells, which hold a volume of approximately 15 μL , they were filled with 0.1 mg/mL streptavidin in PBT (100 mM phosphate buffer, pH 7.5, 0.1% Tween) and incubated for 20 min. During this incubation, 40 μL of 5 mg/mL casein, 100 nM bClpX, and 1 mM ATP γ S in PD buffer (25 mM HEPES, pH 7.6, 100 mM KCl, 10 mM MgCl₂, 10% glycerol) were mixed with 10 μL of streptavidin coated 800 nm beads (Spherotec) and placed in ice. The flow cells were then perfused with 100 μL of 5 mg/mL casein in PBT and incubated for 20 min. The tether complexes were then diluted to an appropriate concentration that yielded single molecule tethers and 20 μL of the solution was flown into the flow cell, allowing their biotinylated ends to bind the streptavidin immobilized on the surface. During this incubation, the bClpX coated beads were washed four times by centrifugation at 13,000 RPM and resuspension in 100 μL of PD buffer containing 1 mM ATP γ S, 5 mg/mL casein, and 0.1 mg/mL free biotin. The bead suspension was then sonicated for 2 min at 40% power prior to flowing 20 μL into the flow cells. After a 20 min incubation, excess beads were washed away from the flow cell with 150 μL of PD buffer containing 5 mg/mL casein, 0.01 mg/mL free biotin, 500 nM ethidium bromide, and the appropriate ATP or ATP γ S concentration. In the case of ATP, a ATP regeneration system was added as well (2.5 mM creatine phosphate and

0.05 mg/mL creatine kinase). All incubation took place in a humidity chamber at room temperature and ambient pressure.

The optical tweezers platform is described elsewhere (Brau, et al, 2006). Briefly, it consists of a heavily modified inverted microscope outfitted with a high numerical aperture oil immersion objective (1.40 NA 100X, Nikon) and a piezo electric stage with nanometer resolution (Physik Instrumente). The trapping, 1064 nm, and detection, 975 nm, lasers are collinearly guided into the objective via a dichroic mirror that sits underneath the objective (Lang, et al, 2002) and reflects infrared light while transmitting visible light. The diameter of the trapping laser is adjusted so that it slightly overfills the objective pupil with a Keplerian telescope made out of two lenses. This leads to the formation of a diffraction limited spot at the specimen plane, which conveys trapping capabilities to the instrument. The location of the trap in the specimen plane is controlled with a pair of orthogonally oriented acousto-optic deflector that permit precise and fast steering in two dimensions. After passing through the condenser lens, the detection laser is spectrally isolated from the trapping beam and imaged on a position sensitive device (PSD) for back focal plane detection with nanometer precision. The optical trap was calibrated using previously described procedures (Lang, et al, 2002; Neuman and Block, 2004; Svoboda and Block, 1994a) and was found to be capable of trapping 1 μm beads with a stiffness of approximately 0.1 pN/nm per 100 mW of trapping laser. The power of the detection laser is typically set to less than a hundredth of the trapping power, so it makes a minimal contribution to the trapping phenomena. All instrument routines are automated and controlled with custom LabView software.

During experiments, flow cells were mounted on the microscope and visually inspected for tethered beads. Once identified, the anchor point of a tether was centered in the middle of the trap by scanning the piezo stage in two dimensions measuring the position of the trapped bead as it swept through the detection region (Khalil, et al, 2007; Wang, et al, 1997). Loads were then exerted on the tether by moving the piezo stage along one of its main axis at constant speed while maintaining the location of the trap stationary. Upon rupture of a tether, each bead was position and stiffness calibrated using the variance method. All data was acquired at 50 kHz through a 16-bit A/D board (National Instruments), anti-alias filtered in line, and analyzed using custom MATLAB software.

Results

Single Molecule Force Spectroscopy Assay

The biotinylation of ClpX (bClpX) facilitates its immobilization on streptavidin-coated microspheres. The functionality of the immobilized bClpX was assessed with an ATP consumption assay as described in Chapter III (Figure 3.1). Since the exact amount of bound ClpX per bead is not known, exact hydrolysis rates could not be determined. However, the ATP hydrolysis rate in the absence of substrate tripled in the presence of GFP-ssrA (results not shown), comparing favorably with experiments done in solution (Figure 3.1). This suggests that the immobilization of bClpX on the surface of bead does not affect its ability to engage, unfold, and translocate substrates.

The developed assay employs a novel tether made by crosslinking a dsDNA segment to a protein containing the *ssrA* recognition sequence. This was achieved by covalently linking an N-terminal cysteine in the protein to a primary amine in one of the 5' ends of the dsDNA segment. The other 5' end of the dsDNA segment contains a biotin motif that facilitates the immobilization of the tether on a coverslip surface coated with nonspecifically immobilized streptavidin. The protein end of the tether contains the topological sequence GFP-I27-*ssrA*, making the tether a substrate for bClpX that has been immobilized on the surface of beads (Figure 4.1).

Similar to the single molecule fluorescence assay for ClpX (Chapter III), substrates were engaged in the presence of ATP γ S. However, in this case, the excess component is the bClpX-coated beads, which are washed away with excess buffer containing an appropriate nucleotide concentration. When ATP or ATP γ S is employed at saturating concentrations of 1 mM, tethered beads are readily observed, with more than 20 tethers per field of view. In contrast, almost no tethered beads were observed in control experiments, which consisted of the systematic removal of streptavidin, tethers, or biotinylated ClpX. This confirms that the tethers are specifically formed, and, establishes the ClpX-substrate interaction as the weakest linkage in the tether since biotin-streptavidin interactions have an affinity constant on the order of 10^{-15} M and are routinely used in single molecule force spectroscopy experimentation. Furthermore, stretching curves of the tethers at low forces revealed that they have a contour length and a persistence length of approximately 390 nm and 40 nm, respectively, which

compare favorably with theoretical and experimental results for a 1010 base pair segment of dsDNA (Wang, et al, 1997). In addition, although difficult to detect because of bead autofluorescence, fluorescence irradiating from the GFP could be observed for a brief period before it photobleached. Finally, no tethers were observed in the absence of nucleotide.

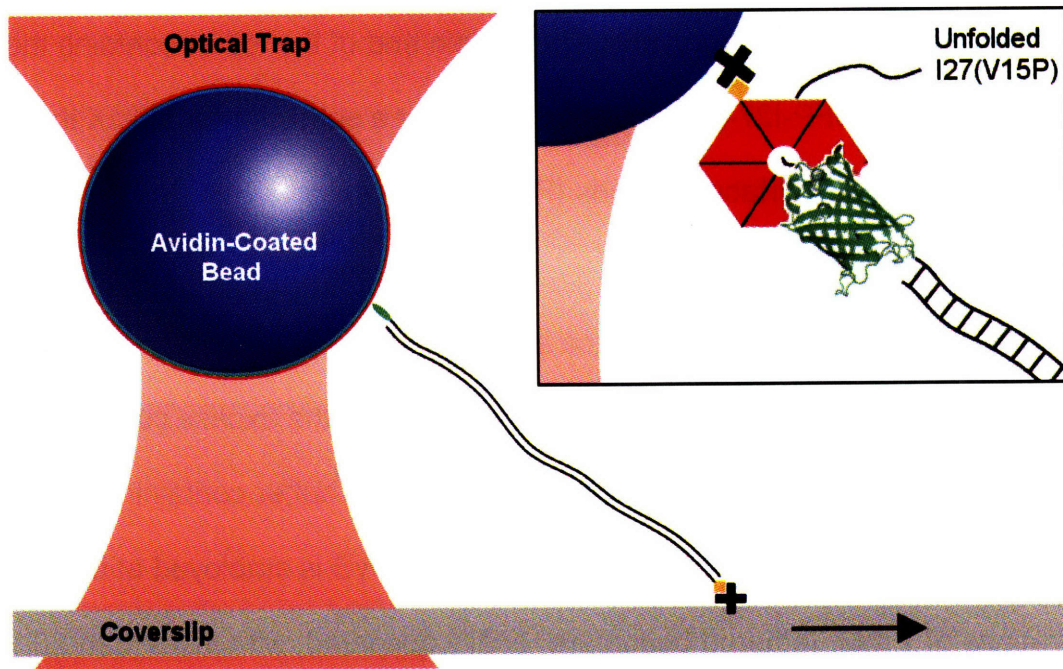


Figure 4.1 Single molecule force spectroscopy assay for ClpX. Tether complexes were made by crosslinking a N-terminal cysteine in a ClpX substrate to a 5' primary amine. The dsDNA segment is 1010 bp long and has a biotin motif on the opposing 5' end that facilitates immobilization on streptavidin coated surfaces (black cross). The other end of the tether, which contains a GFP-I27-ssrA fusion protein (green oval), can interact with biotinylated ClpX immobilized on a streptavidin-coated polystyrene bead. Once tethered, the bead can be optically trapped and manipulated. (inset) Close-up of the ClpX-substrate interaction shows that in the presence of ATP γ S, the I27 domain is translocated through the pore of ClpX (red hexamer), while GFP remains folded.

Force-Induced Unbinding

Optical tweezers force spectroscopy was used to probe the interaction between ClpX and its substrates. Briefly, 800 nm tethered beads were captured with a stationary optical trap that was characterized as a parabolic potential well with a stiffness of approximately 0.6 pN/nm. After centering the trapped bead and placing it a few nanometers directly above the tether anchor point with an automated procedure, the tether was loaded by moving the coverslip surface relative to the trap with the piezo electric stage at a speed of approximately 100 nm/s, yielding an expected loading rate of about 60 pN/s. Each loading curve exhibits a single clean break rather than the typical saw tooth pattern representative of multiple unbinding or unfolding events. Considering that the resolution of the instrument is on the order of one nanometer, this suggests that ClpX or substrate unfolding was not taking place. Prior to rupture, a characteristic unbinding curve is reminiscent of dsDNA stretching in which little force is required to unravel the collapsed chain before higher loads are necessary once the chain is extended (Figure 4.2). Upon rupture, the bead immediately returns to its baseline location in the center of the trap, suggesting that only one tether was being loaded and indicating that all physical connections to the surface of the sample have been severed. After rupture, the stage was moved by another 500 nm to further confirm that the bead had a single tether and that only one ClpX-substrate interaction was being probed.

In order to measure the strength of the ClpX-substrate interaction, experiments under different nucleotide conditions were carried out. Results show that the ClpX-substrate

interaction can withstand substantial levels of force, higher than 40 pN, regardless of the nucleotide concentration or identity. For 1 mM ATP γ S (n = 120), 1 μ M ATP γ S (n = 33), 1 mM ATP (n = 54), and 1 μ M ATP (n = 39) mean rupture forces of 61.79 ± 24.42 pN, 64.14 ± 24.14 pN, 61.99 ± 35.18 pN, and 46.92 ± 19.01 pN were observed (Table 4.2), where values are presented as the sample average \pm the standard deviation of the mean. Of these, only the mean rupture force for 1 μ M ATP proved to be statistically significant from the other data sets, according to a t-test performed at a 95% confidence limit (Table 4.1). Since the optical trap instrument is only calibrated to measure forces in the plane perpendicular to the laser beam, these measurements have been triangulated to account for the vectorial nature of the forces applied. This means that for a bead radius of about 400 nm, and a tether length that is also on the order of 400 nm, the true force exerted on the tether is approximately $\sqrt{3}$ times larger than the measured force at the time of rupture. The measured rupture forces are close to the force at which dsDNA undergoes a transition from B-form to S-form and ultimately melts (Smith, et al, 1996), leading to rupture. This problem was circumvented by having ethidium bromide, a intercalator that increases the melting force of dsDNA from about 60 pN to over 120 pN at a concentration of 500 nM (Vladescu, et al, 2007), present in the assay buffer.

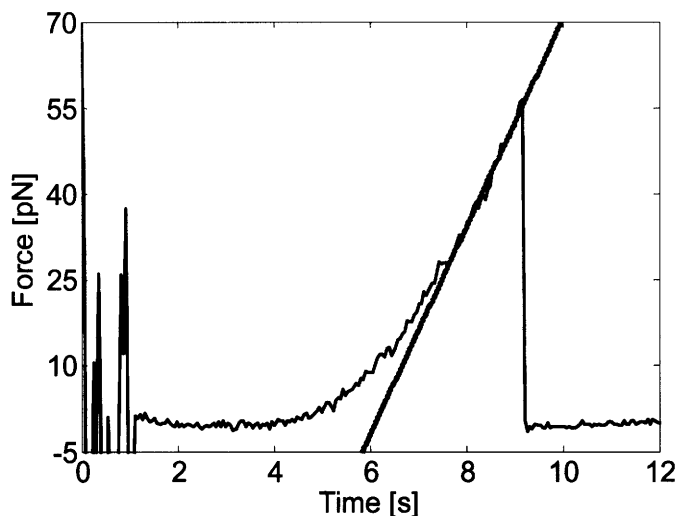


Figure 4.2 Sample ClpX-substrate unbinding curve. After centering the optical trap over a tethered bead, the bead is trapped at 1 s. At this point, the load exerted on the tether is increased by moving the sample relative to the trap. After rupturing, which occurs at approximately 9 s at a force level of about 55 pN, the bead returns to the center of the trap, where it experiences an average force of 0 pN. The experimental loading rate prior to rupture was determined to be about 18 pN/s by fitting the data just before the unbinding event (gray line). The data between 0 and 1 s correspond to the Brownian motion of an untrapped tethered bead.

Rupture Force Distributions and Modeling

In order to extract more information about the ClpX-substrate interaction, probability distribution histograms of the dissociation events were constructed and fitted to two theoretical models (Figure 4.3). Both of these models, the Bell-Evans (BE) and the Hummer & Szabo (HS), can be used to estimate the no-load intrinsic dissociation rate, k_{off} , and the transition distance from the free-energy minimum to the rupture barrier, x^\ddagger , of a particular unbinding or unfolding event. The BE model, which combines Bell's theory of bond dissociation (Bell, 1978) with chemical kinetics, has been used extensively to describe single molecule force spectroscopy unbinding and unfolding populations obtained with both optical trapping and atomic force microscopy techniques

(Evans and Ritchie, 1997; Guo and Guilford, 2006; Lang, et al, 2004; Neuert, et al, 2006). On the other hand, the HS model introduces a more general microscopic formalism, is applicable for a larger range of loading rates, and fits for a third parameter, the molecular spring constant, κ_m , that can be used to approximate the free energy profile of the molecular interaction (Hummer and Szabo, 2001, 2003). Both the BE and the HS models use the loading rate of the tether prior to rupture as an input parameter. As mentioned above, the expected loading rate is about 60 pN/s; however, it is better to measure the experimental loading rate directly from an unbinding curve by fitting the data just before the rupture event to a straight line (Ray, et al, 2007) (Figure 4.2). Histograms of the experimentally determined loading rates reveal averages \pm standard deviations of the mean of 20.15 ± 6.79 pN, 21.32 ± 5.87 pN, 20.92 ± 11.84 pN, and 14.45 ± 4.62 pN for the 1 mM ATP γ S, 1 μ M ATP γ S, 1 mM ATP, and 1 μ M ATP experimental groups, respectively (Table 4.2). These values are lower than the expected loading rate of 60 pN/s. However, one must remember that the stiffness of dsDNA is not constant, unlike that of the optical trap. Furthermore, if one treats dsDNA and the trap as two springs in series, the overall stiffness of the system will be characterized by the weakest spring. Thus, the stiffness of the system cannot be higher than the stiffness of the trap, leading to an experimentally determined loading rate that is lower than expected. Nevertheless, similar to the rupture forces, the loading rate for the 1 mM ATP condition was found to be statistically different from the other groups (Table 4.1). The population statistics for each experimental group was used to discriminate against outlying rupture events by discarding those events in which the loading rate was more than two standard deviations away from the mean of the

population. However, not more than two events were eliminated from each data set using this methodology. Nevertheless, this allows the loading rate populations to be treated as constant, as described by their average, which is an important consideration in the application of the BE and HS models.

	Rupture Force				Loading Rate			
	1 mM ATP γ S	1 μ M ATP γ S	1 mM ATP	1 μ M ATP	1 mM ATP γ S	1 μ M ATP γ S	1 mM ATP	1 μ M ATP
1 mM ATP γ S	1	-	-	-	1	-	-	-
1 μ M ATP γ S	0.617	1	-	-	0.48	1	-	-
1 mM ATP	0.955	0.758	1	-	0.8166	0.758	1	-
1 μ M ATP	0.001	0.001	0.017	1	0.000	0.000	0.001	1

Table 4.1 p-values for the rupture force and loading rate populations for unbinding events of the ClpX-substrate interaction at different nucleotide conditions. For a 95% confidence limit (5% significance), the p-values show that the rupture forces and loading rates for the 1 μ M ATP population are different than the other experimental groups. No statistically significant differences were observed between the 1 mM ATP γ S, 1 μ M ATP γ S, and 1 mM ATP groups.

According to the BE model, for a constant loading rate, the probability density function, $p_{BE}(F)$, of a population of rupture forces, F , is given by

$$p_{BE}(F) = A \exp\left(\frac{F}{B}\right) \exp\left[AB\left(1 - \exp\left(\frac{F}{B}\right)\right)\right], \quad (4.1)$$

where F is the force range in which rupture events are observed and $A = k_{off} / \dot{F}$ and $B = k_b T / x^\ddagger$, where k_{off} and x^\ddagger are defined as before and k_b is Boltzmann's constant, T the

absolute temperature of the system, and \dot{F} the experimentally-determined average loading rate of the population. The probability density function for the HS model can be obtained by evaluating

$$p_{HS}(F) = \frac{A'}{\kappa_s v} \exp[A' - A' e^{(B't - C't^2)}] \exp(B't - C't^2) (B' - 2C't) \quad (4.2)$$

at time

$$t = \frac{F + \kappa_s x^\ddagger}{\kappa_s v}, \quad (4.3)$$

where $\beta = (k_b T)^{-1}$. The expression for the HS probability density function has been simplified by defining

$$A' = \frac{k_{off} \exp[-\beta \kappa_s (x^\ddagger)^2 / 2]}{\beta \kappa_s v x^\ddagger (\kappa_m / \kappa)^{3/2}}, \quad (4.4)$$

$B' = \beta \kappa_s v x^\ddagger$, $C' = \beta (\kappa_s v)^2 / (2\kappa)$, and $\kappa = \kappa_s + \kappa_m$, where κ_s and κ_m are the trap and molecular spring constants, respectively, and v is the pulling velocity at which the tether is loaded; thus, in this model, the loading rate prior to rupture is equal to $\kappa_s v$. These models claim that a molecular interaction can be completely described by the parameters k_{off} and x^\ddagger , and, in the case of the HS model, κ_m . The molecular spring constant is of particular importance because it can be used to describe the free-energy profile along the pulling reaction coordinate, $\Delta G(x) = (\kappa_m x^2) / 2$. Furthermore, the height of the free energy barrier at rupture can be determined by evaluating $\Delta G(x^\ddagger)$.

Each experimental condition was fit individually to both models (Figure 4.3) (Table 4.2). The HS model readily captures the rupture force histograms, as evidenced by goodness of fit parameters, R^2 , larger than 0.73 for all experimental conditions. On the other hand, the goodness of fit for each group was lower for the BE model than the HS model. This makes sense since the HS model is more flexible because it fits for three parameters instead of two. Interestingly, both models fit the 1 μM ATP γS ($n = 33$) and 1 μM ATP ($n = 39$) experimental groups worse than the 1 mM ATP γS ($n = 121$) and 1 mM ATP groups ($n = 54$). Although it is possible that the rupture kinetics at high nucleotide concentrations are better described by the models employed, it is more likely that the limited number of samples recorded for the low nucleotide concentrations is affecting the fits.

The fits obtained for the intrinsic dissociation constant and the distance to the transition state for each model agree well with each other, with x^\ddagger and k_{off} being on the order of 0.25 nm and 0.05 s^{-1} , respectively. However, for each experimental group, the HS model fits for a lower k_{off} , with a range between 0.02318 to 0.06923 s^{-1} , than the BE model, with a range between 0.0612 to 0.08969 s^{-1} . The opposite is true for the distance to the transition state, x^\ddagger , as the HS model fits for a range between 0.2398 to 0.05165 nm, while the BE model returns a range between 0.1416 to 0.21 nm. Both models show that k_{off} and x^\ddagger increase and decrease, respectively, as the ATP concentration is lowered, which could be an indication that at lower nucleotide concentrations it is easier for force-induced dissociations to occur. The BE model reveals the same trend as the concentration of ATP γS is reduced. However, the HS model yields the opposite

relationship for ATP γ S. The reasons for these discrepancies are unclear, but considering the relative similarities in the fits for both models, it is difficult to make a clear distinction between them. In addition, the fitted values for k_{off} and x^\ddagger are similar to other force spectroscopy measurements done on systems with rupture force averages on the same range as those measured here (Guo and Guilford, 2006; Lang, et al, 2004; Neuert, et al, 2006).

The HS model also reveals that the molecular spring constant of the ClpX-substrate interaction decreases as the nucleotide concentration is lowered. This is particularly true for the ATP condition, in which a $\sim 30\%$ decrement is observed, whereas a $\sim 12\%$ drop is observed for the ATP γ S condition. In addition, the molecular spring constant is over twice as stiff in the presence ATP than ATP γ S for both high and low nucleotide concentrations. This suggests that the ClpX-substrate interaction is stiffer in the presence of ATP, which is hydrolyzed by ClpX 20-fold faster than ATP γ S. As described above, the molecular spring constant and the distance to the transition state can be used to calculate the height of the rupture free energy barrier. Interestingly, $\Delta G(x^\ddagger)$ is on the order of $5 k_bT$ for the 1 mM ATP γ S, 1 μ M ATP γ S, and 1 μ M ATP experimental groups. However, $\Delta G(x^\ddagger)$ increases to over $9 k_bT$ in the presence of 1 mM ATP, suggesting that the ClpX-substrate interaction is strongest in the presence of saturating concentrations of ATP.

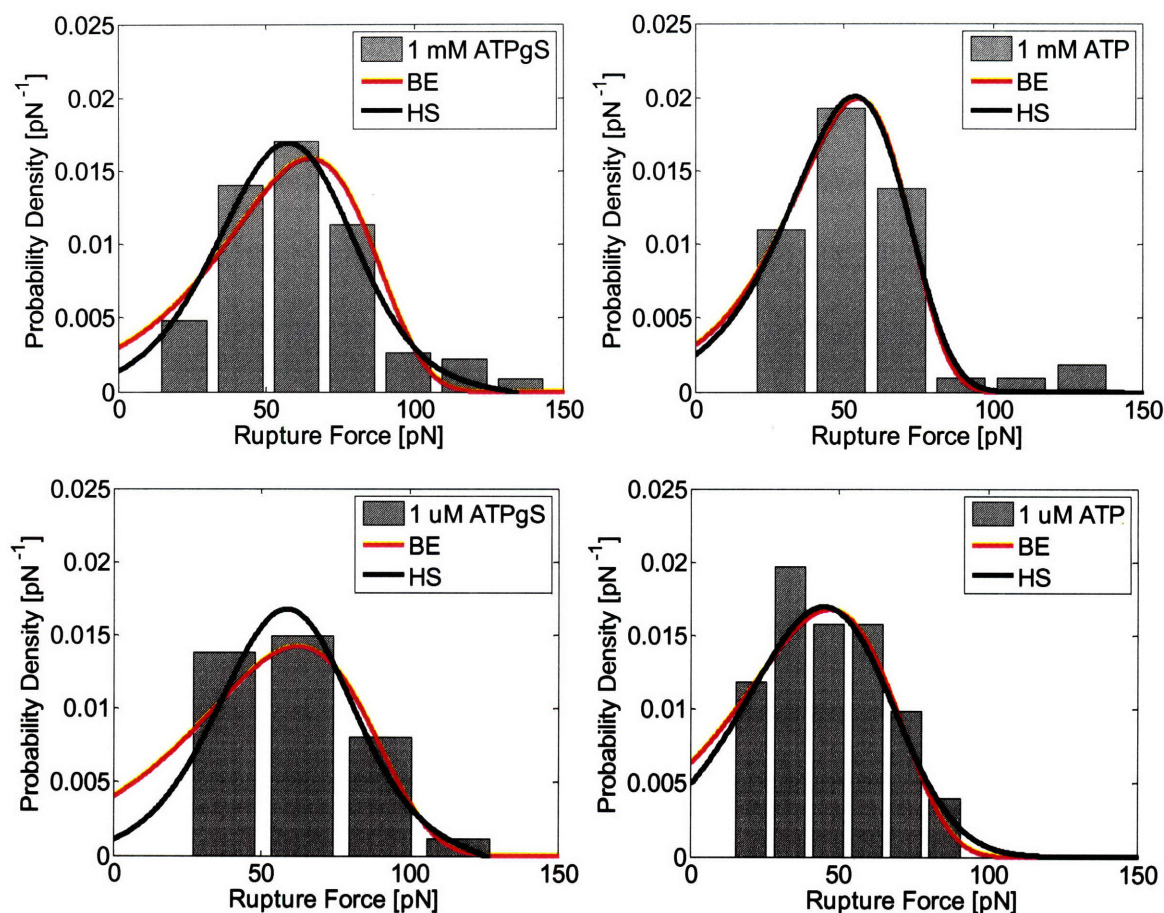


Figure 4.3 Rupture force probability density distributions for the ClpX-substrate interaction. Unbinding measurements were carried out in the presence of ATPγS (left) or ATP (right) at concentrations of 1 mM (top) or 1 μM (bottom). Results show that the ClpX-substrate interaction is severed at approximately 60 pN at all nucleotide conditions, except for 1 μM ATP, which shows a rupture force of about 45 pN (Table 4.2). The histograms were fit to either the Bell-Evans or the Hummer-Szabo models to gain information about the intrinsic dissociation rate, the distance to the transition state, the molecular stiffness of the interaction, and the height of the rupture free energy barrier. Even though the HS model seems to provide a better fit, both models agree with each other relatively well (Table 4.2).

The ClpX-substrate interaction measured above is a static one in which the I27 domain of titin in the C-terminal of the substrate has been unfolded and translocated by ClpX (Figure 4.1). However, since the I27 domain of titin has been observed to refold after being unfolded with an AFM (Rief, et al, 1997), it is possible that it can refold behind ClpX after translocation. In order to address whether the force spectroscopy

measurements presented above were unfolding the I27 domain of titin before rupturing the ClpX-substrate interaction, the I27 domain of titin was carboxymethylated.

Carboxymethylation has shown to irreversibly unfold the I27 protein domain, making it easier for ClpX to translocate it since the unfolding step has been removed (Kenniston, et al, 2003). Force spectroscopy measurements on this tether with the carboxymethylated I27 show average rupture forces and loading rates of 50.251 ± 19.1578 and 15.9385 ± 4.8161 , respectively, which are on the same range as the results presented above for the native I27. This, combined with the fact that I27 unfolds under loads higher than 100 pN, as confirmed measured in AFM experiments (Oberhauser, et al, 1999), suggests that, regardless of whether I27 is refolding or not after translocation, the rupture force measurements presented above are probing the ClpX-substrate interaction.

	1 mM ATP γ S	1 μ M ATP γ S	1 mM ATP	1 μ M ATP
n	121	33	54	39
Rupture Force [pN]	61.74 \pm 24.5	64.14 \pm 24.14	61.99 \pm 35.18	46.92 \pm 19.01
Loading Rate [pN/s]	20.52 \pm 7.75	21.55 \pm 5.93	20.87 \pm 11.73	14.24 \pm 4.73
Bell-Evans				
k_{off} [s^{-1}]	0.0612	0.08649	0.06569	0.08969
x^{\ddagger} [nm]	0.1649	0.1416	0.21	0.1597
R^2	0.85	0.59	0.98	0.80
Hummer-Szabo				
k_{off} [s^{-1}]	0.02814	0.02318	0.05165	0.06923
x^{\ddagger} [nm]	0.3451	0.3701	0.2697	0.2398
K_m [pN/nm]	385.1	339.9	1029	726.5
R^2	0.9486	0.7326	0.9812	0.8209
$\Delta G(x^{\ddagger})$ [k_bT]	5.5762	5.6606	9.1002	5.0794

Table 4.2 Summary of results for single molecule force spectroscopy measurements of the ClpX-substrate interaction. Rupture force histograms for high and low concentrations of ATP and ATP γ S were fitted to the BE and HS models to obtain information about the intrinsic dissociation rate, the distance to the transition state, the molecular spring constant, and the height of the rupture free energy barrier of the ClpX-substrate interaction.

Discussion

In this report, we have introduced the first single molecule force spectroscopy assay for the ClpX ATPase. This is an important milestone as it opens the door for much experimentation that can be expanded to the rest of the AAA+ community. The results presented here did not find much difference between the strength of the ClpX-substrate

interaction for high and low concentrations of ATP and ATP γ S. In fact, the lowest average force measured, on the order of 45 pN for the 1 μ M ATP experimental group, was only 25% less than the forces measured for the other experimental groups.

However, the standard deviation of the measurements for each group, on the order of 40% of the mean, makes it hard to concretely distinguish between the experimental groups, even though the rupture forces and the loading rates for the results for the 1 μ M ATP group were shown to be statistically different from the other nucleotide tests. Since a similar result is not observed at low ATP concentrations, it is possible that these differences may simply arise from relatively small sample sizes. Taken together, this data suggests that rupture of the ClpX-substrate interaction occurs when force levels that can open the ClpX hexameric ring are reached. Since this is the first force spectroscopy experimentation in which ClpX is immobilized, it is not known what effects does its proximity to the bead surface may have on its stability. In addition, ClpX stability has already been hindered in the absence of ClpP, which docks onto the enzyme and stabilizes it, as evidenced by a reduction and an increase in its ATP hydrolysis rate and substrate unfolding capabilities, respectively, in the presence of ClpP (Joshi, et al, 2004; Martin, et al, 2007).

The systematic removal of different assay components suggests that the ClpX-substrate interaction is specifically being probed. None of these results is more instructive than the lack of tethers observed in the absence of nucleotide. Tethers were readily observed in the presence of 1 mM ATP or ATP γ S, a result that is consistent with the view that ClpX needs to first engage and then unfold the I27 domain of titin for tethering

to occur. As the concentration of nucleotide was lowered from 1 mM to 1 μ M, the number of tethers observed was dramatically reduced, and the ones observed were not long lived. In this case, the tethered beads would spontaneously dissociate after a short period of time, suggesting that ClpX requires at least a couple of its nucleotide sites filled in order to appropriately engage its substrates (Hersch, et al, 2005). Since the affinity for the ClpX-nucleotide interaction is on the order of 10 μ M (Burton, et al, 2003), it is possible that only one nucleotide site is being occupied per enzyme in the low nucleotide conditions. Interestingly, the level of force that the ClpX ring can withstand does not appear to significantly depend on the nature or concentration of the nucleotide employed. In addition to confirming that nucleotide binding triggers a conformational change in ClpX that allows it to engage substrates, this suggests that ClpX only holds on to its substrate with only one monomer. Previous studies showed that under saturating ATP conditions only about 2 ClpX monomers are capable of binding ATP at a time (Hersch, et al, 2005). Perhaps, even though the enzyme can bind multiple nucleotides, it only allows for one monomer at a time to engage substrate and the other monomers with bound ATP are simply waiting for the substrate to be passed on after hydrolysis. If there are no more monomers with ATP, this might lead to slipping or dissociation. This is consistent with experiments in which only one active ClpX monomer can drive substrate degradation (Martin, et al, 2005).

The single molecule assay developed in this report utilizes streptavidin that has been nonspecifically absorbed on glass as its anchor point. In addition to the ClpX-substrate interaction, the rest of the links in the tethering scheme consist of covalent bonds,

biotin-streptavidin interactions and the targeted ClpX-substrate interaction. Thus, if the streptavidin is weakly immobilized, it could severely contaminate the results. This was addressed by slightly modifying the streptavidin immobilization strategy by, instead of depositing it directly on the glass surface, binding it to nonspecifically absorbed biotin-BSA or covalently bound PEG linkers with biotin motifs at its ends. The rupture forces made with these schemes were in great agreement with those presented above (results not shown), strongly suggesting that the ClpX-substrate interaction is being specifically probed. Even though the strength of the interaction between nonspecifically absorbed proteins and glass has never been measured, it is likely that this interaction is very strong since nonspecifically bound I27 concatamers in AFM experiments can withstand forces higher than 200 pN.

The results presented here indicate that the rate of hydrolysis of nucleotides in saturating concentrations does not affect the forces that ClpX is capable of exerting. The same is true at concentrations of 1 μM , although the tethers were found to be short lived. This suggests that ATP concentration only influences the speed at which unfolding and translocation can occur. This behavior is similar to the molecular motor kinesin, in which its affinity for microtubules, its substrate, is not influenced by ATP concentration, but the velocity at which it moves and the distance it travels, its processivity, are heavily dependent on it. Kinesin's velocity and processivity have been found to be heavily dependent on external loads exerted with an optical trap (Block, et al, 2003). This is likely the case for ClpX as well, but a processivity assay has yet to be developed. With the assay presented here, we attempted to capture ClpX as it unfolded

and translocated GFP. Unfortunately, this was not possible because the speed at which the instrumentation could be set up to capture these events was slower than the rates of unfolding and translocation. In addition, slowing down these events was not an option because ClpX cannot unfold GFP in the presence of ATP γ S or for concentrations ATP much lower than 1 mM ATP. Perhaps a longer tether containing more protein domains will provide enough time for these interesting events to be monitored.

Chapter V

Passive Microrheology with Optical Tweezers

(This chapter was adapted from Brau, et al, 2007)

Abstract

Efforts at understanding the behavior of complex materials at the micro scale have led to the development of many microrheological techniques capable of probing viscoelastic behavior. Among these, optical tweezers have been extensively developed for biophysical applications, offer several advantages over traditional techniques, and can be employed in both passive and active microrheology applications. In this report, we outline several methods that can be used with optical tweezers to measure the microrheological behavior of materials such as glycerol and methylcellulose solutions. In addition, we quantify the effect that the index of refraction of solution has on the stiffness of the optical trap. Our results indicate that optical tweezers force microscopy is a versatile tool for the exploration of viscoelastic behavior in a range of substrates at the micro scale.

Introduction

Complex fluids that exhibit both elastic and viscous properties are referred to as viscoelastic materials. Under dynamic stress, these materials exhibit a nonlinear, time dependent behavior captured by $\sigma = G^*\epsilon$, where σ is the applied stress, ϵ is the resulting strain and G^* , known as the complex shear modulus, is a measure of the material's resistance to deformation. The real part of complex shear modulus, G' , represents the ability of the material to store energy while the imaginary part, G'' , represents the ability to dissipate energy. These properties can be probed at the micro scale with a range of techniques collectively known as microrheology. Most microrheological methods rely on the temporal monitoring of microscopic particle displacements, permitting reduced sample sizes and direct access to the properties that determine, but do not necessarily mirror, macroscopic behavior. Microrheological techniques are further categorized as either passive, where the thermal fluctuations of an embedded particle are monitored, or active, where an external force is applied to an embedded particle to deform the medium while its response is monitored. In this report, we describe the use of optical tweezers microrheology to experimentally measure both components of $G^*(\omega)$ in complex fluids and polymer solutions. In addition, we describe methods to determine the viscosity of solutions using Stokes drag and quantify the effects that changes the index of refraction of a solution have on the stiffness of an optical trap.

Optical tweezers are often used to trap and manipulate individual dielectric microspheres with diameters on the order of 1 μm . These particles, which are similar in

size to those used in particle tracking microrheology (PTM), are constrained by the refractive forces in a tightly focused laser beam. In an optical trap, mechanical forces between 0.1 to 100 pN can be readily applied with nanometer position resolution. Such forces are quantified by modeling the optical trap as a linear spring, measuring small particle displacements from the center of the trap, and calibrating the trap spring constant, or stiffness. The stiffness of the trap depends in part on the refractive index and size of the particle, the wavelength of the trapping light, the dimensions and photon flux in the trap focus, and the optical properties of the surrounding medium (Ashkin, 1992). These factors and their independence from the viscosity of the surrounding medium make optical tweezers force microscopy well suited for microrheological applications.

The noninvasive nature of optical tweezers force microscopy also makes it an ideal approach for studying the localized viscoelastic properties of solutions. In addition, because optical tweezers can monitor or manipulate microscopic objects by exerting loads larger than thermal forces, both passive and active microrheology can be approached with a single probe. For example, optical tweezers can extend the principles of PTM by passively monitoring the motion of a trapped particle and relating it to the properties of the surrounding material by using the generalized Stokes-Einstein equation (Mason, 2000; Mason, et al, 1997; Schnurr, et al, 1997; Yamada, et al, 2000). When an optical trap is employed, the particle is physically held inside a detection zone, avoiding traditional PTM complications associated with a freely diffusing particle exiting the field of view. Furthermore, optical tweezers provides resolution of nanometer-level

distortions and high frequency responses, up to ~10 kHz, not accessible with PTM, which is typically limited to ~10 Hz (Waigh, 2005). With traditional PTM methods, the locations of the particles are usually monitored using video recording, thus limiting the spatial and temporal resolution of such measurements.

In addition to monitoring the motion of particles resulting from thermal forces, optical tweezers can be used to exert forces or drag a trapped particle to mechanically deform the embedding medium (Furst, 2005; Valentine, et al, 1996). This approach is known as active microrheology and offers the potential of measuring the high-deformation response of the material of interest, including elastic non-linear behavior. Traditionally, magnetic tweezers have been used in active microrheology because they can explore higher force levels than optical tweezers. However, optical tweezers are increasingly finding new active microrheology applications because of their versatility and ability to precisely position beads in locations of interest. In addition, optical tweezers can simultaneously manipulate multiple beads whose surface chemistries can be easily modified, allowing for the measurement of different interactions between the beads and the surrounding medium.

Several reports have used both passive or active optical tweezers microrheology to study complex solutions, including suspensions of viruses (Addas, et al, 2004), polymer hydrogels (Yamaguchi, et al, 2005), and wormlike micelles (Atakhorrami and Schmidt, 2006). In addition, optical tweezers have also found novel applications in rotational microrheology (Bishop, et al, 2004; Cheng and Mason, 2003) and colloidal

micromechanics (Furst and Gast, 1999; Pantina and Furst, 2004), and have been used to locally heat regions of interest (Bishop, et al, 2004; Peterman, et al, 2003). Here, we outline optical tweezers approaches to study the behavior of glycerol and methylcellulose solutions.

Instrumentation

The optical tweezers setup is detailed elsewhere (Brau, et al, 2006; Lang, et al, 2002). Briefly, it consists of collinear trapping (1064 nm) and detection (975 nm) lasers guided into a 100X, 1.4 NA, oil-immersion objective on a heavily modified inverted microscope. The instrument is also equipped with a 3-axis piezoelectric stage, a position sensitive device (PSD), and a pair of acousto-optic deflectors (AODs) that increase its versatility and functionality. In addition, many instrument components and routines are completely automated. All position and force calibrations were performed as described elsewhere (Lang, et al, 2002; Neuman and Block, 2004; Svoboda and Block, 1994a).

Results and Discussion

Stokes Drag and Index of Refraction Considerations

The simplest microrheological measurement that can be made with optical tweezers is that of determining the viscosity of a particular fluid using Stokes drag. When such viscosity is unknown, the stiffness of the optical trap must first be calibrated with a method that does not require *a priori* knowledge of the viscosity of solution. This is done

with the equipartition theorem (Neuman and Block, 2004; Svoboda, et al, 1994), which relates bead position to thermal energy such that

$$\frac{1}{2}k_bT = \frac{1}{2}\alpha \langle x^2 \rangle, \quad (5.1)$$

where k_b is Boltzmann's constant, T is the absolute temperature of the system, α is the stiffness of the trap, and $\langle x^2 \rangle$ is the time-averaged positional variance of a trapped bead.

This direct measure of trap stiffness can then be used to determine the viscosity of the surrounding fluid. Such measurements can be approached with the Stokes Drag method, which monitors displacements in a trapped bead under external fluid flow (Neuman and Block, 2004; Svoboda, et al, 1994). Under constant fluid flow, the equilibrium between the drag imparted on the bead and the restoring force of the trap is given by the force balance

$$\alpha x = 6\pi\eta r v, \quad (5.2)$$

where x is the displacement of the bead from the center of the trap, r is the radius of the bead, η is the viscosity of the fluid, and v is the velocity of the fluid, which is estimated by the velocity of stage motion.

We employed this framework to determine the viscosity of anhydrous glycerol (American Bioanalytical), a small molecule with many industrial applications and a critical component of many biomolecules. Glycerol, a colorless liquid with a bulk viscosity of approximately 1.4 Pa s, has been shown to be significantly less viscous when mixed with water (Renaud, et al, 2005). This was verified in our experimental system using Stokes drag to determine the viscosity of different water-glycerol mixtures. Samples were prepared by mixing 100 μ L of the appropriate mixture with 0.5 μ L of 490 nm beads that had been resuspended in water. The viscosity of pure water was measured to be 0.8 mPa s, which is in close agreement with the standard value of 1 mPa s at room temperature when taking into account the variability in the average bead radii. As expected, the addition of slight amounts of glycerol to water do not significantly increase the viscosity, as a 25% (v/v) glycerol mixture was only 2.5X more viscous than pure water (Figure 5.1). In fact, the viscosity of the mixtures exhibits an exponential dependence with glycerol content for mixtures with less than 50% (v/v) glycerol. Sharper increases in viscosity were observed for mixtures with a higher glycerol content, as evidenced by the 75% and 100% (v/v) solutions, which were 30 and 600X more viscous than pure water, respectively. This trend compares favorably with accepted viscosity values (Renaud, et al, 2005), showing the suitability of optical tweezers approaches for active microrheological experiments. Furthermore, these experiments show that the precision of this approach is not compromised by common low frequency noise sources such as drift.

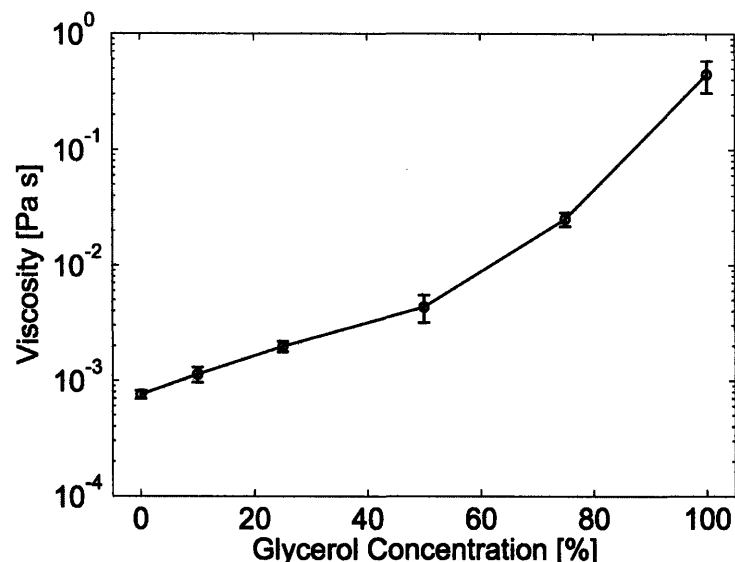


Figure 5.1 Viscosity of different water-glycerol mixtures as determined with optical tweezers using the Stokes method. The viscosity has an exponential dependence on glycerol content for concentrations less than 50%. Each data point is the average ($n \sim 10$) of experiments performed on different beads, and the error bars represent the standard deviation of the mean.

The methodological validation provided by glycerol experiments can be further extended to study the effects of different refractive indices on trap stiffness (Resnick, 2003), which are important because complex fluids may have different optical properties than water. We approached this comparison with different mixtures of water, refractive index of 1.3328, and glycerol, refractive index of 1.4718. For comparison, refractometer measurements provided the refractive index of water-glycerol mixtures, which increase linearly with glycerol content (Table 5.1). Using these same set of solutions, we showed that, as expected, equipartition-determined trap stiffness increases linearly with trapping laser power (Figure 5.2), which was measured before entering the objective. However, the slope of the linear fits decrease with increasing glycerol content. This effect can be explained by the role of refractive index mismatches between the trapped particle and the surrounding medium in determining trap stiffness. As glycerol is added, the

refractive index of the solution is brought closer to that of the particle, 1.55 for silica beads in this case, and trap stiffness is reduced. This effect is corrected by normalizing the trap stiffness with the relative refractive index, such that

$$\alpha_w = \alpha_m \frac{n_b - n_w}{n_b - n_m}, \quad (5.3)$$

where α_w is the expected trap stiffness in water at any given power, α_m is the measured trap stiffness in a given glycerol mixture, and n_b , n_w , and n_m are the index of refraction of the bead, water, and mixture, respectively. By applying this correction, the power-dependent trap stiffness measurements collapse into a single line (Figure 5.2), with the exception of high glycerol-content mixtures in which higher viscosities introduce low frequency errors in trap stiffness calibrations (Neuman and Block, 2004). Nevertheless, this result confirms that differences between trap stiffness in different glycerol mixtures are entirely due to index of refraction effects, providing a method to determine such changes and to extrapolate trap stiffness when using solutions with varying refractive index.

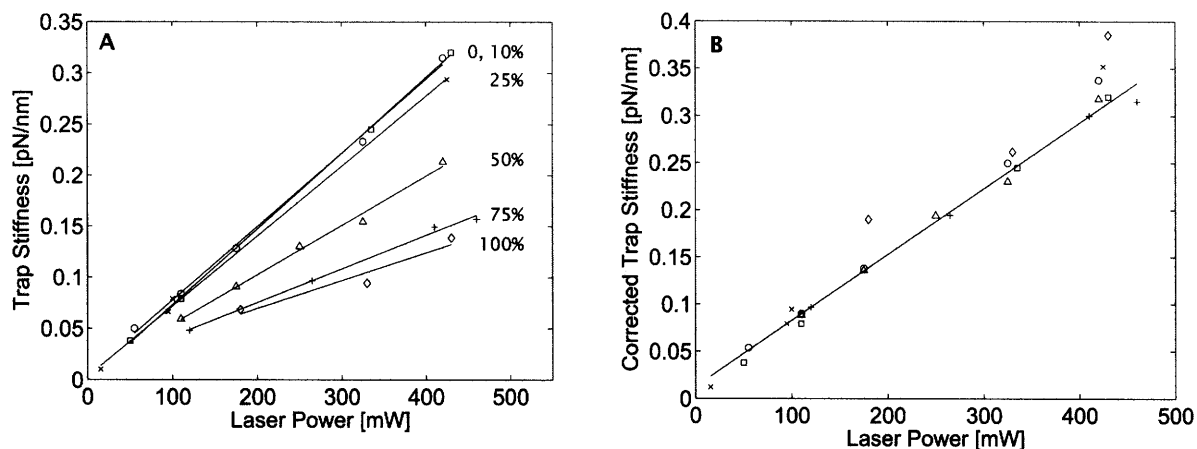


Figure 5.2 Index of refraction effects on optical trap stiffness. (a) Trap stiffness as a function of laser power for beads in mixtures of varying glycerol content: \square (0%, Water), \circ (10%), \times (25%), Δ (50%), $+$ (75%), \diamond (100%). The dependence on laser power decreases with increasing glycerol content. Each solid line represents a fit to each mixture. (b) The trap stiffness was adjusted to account for changes in index of refraction, allowing the data to be described by a linear fit.

Glycerol (v/v) (%)	Index of Refraction, n	Methylcellulose (w/v) (%)	Index of Refraction, n
0	1.3328	0	1.3328
10	1.3476	0.1	1.3402
25	1.3688	0.5	1.3422
50	1.4043	1	1.3423
75	1.4418	2	1.3442
100	1.4718	3	1.3447

Table 5.1 Refractive indices for glycerol and methylcellulose solutions.

Theoretical Considerations

The motion of an optically trapped bead in a purely viscous medium is described by the Langevin equation,

$$\alpha x(t) + \beta \frac{dx(t)}{dt} = f_{th}(t), \quad (5.4)$$

where β is the viscous drag coefficient and f_{th} is the thermal force resulting from random collisions between the bead and medium. In the Newtonian limit, which applies in aqueous media, viscous effects are time-independent for all time scales, and the drag coefficient is given by $\beta = 6\pi\eta r$. However, many polymeric solutions and biologically relevant materials exhibit time-dependent viscoelastic behaviors. These behaviors are described by the complex shear modulus, $G^*(\omega) = G'(\omega) + iG''(\omega)$, where ω represents angular frequency and G' and G'' are the storage and loss moduli, respectively. In this general case, the Fourier transform of the motion of a trapped bead, $x(\omega)$, can be related to the Fourier transform of the thermal force, $f_{th}(\omega)$, by

$$x(\omega) = \frac{f_{th}(\omega)}{6\pi\omega G^*(\omega)} = h(\omega) f_{th}(\omega), \quad (5.5)$$

where $h(\omega) = h'(\omega) + ih''(\omega)$ is the complex transfer function for the system of interest (Addas, et al, 2004; Schnurr, et al, 1997). For any external load, this complex transfer function captures the response of an optically trapped bead in a viscoelastic medium. If the trapped bead is in thermal equilibrium with the environment, the fluctuation

dissipation theorem (Gittes, et al, 1997; Landau, et al, 1980) can be used to determine the imaginary part of the transfer function

$$h''(\omega) = \frac{\omega S(\omega)}{4k_b T}, \quad (5.6)$$

where $S(\omega)$ is the experimentally determined power spectral density (PSD) of bead motion given by

$$S(\omega) = \lim_{T \rightarrow \infty} \frac{2}{T} |x(\omega)|^2 = \lim_{T \rightarrow \infty} \frac{2}{T} \left| \int_0^T x(t) e^{i\omega t} dt \right|^2, \quad (5.7)$$

where T is the duration of the recorded data signal. For the case of an optically trapped bead in pure water, the PSD is described by a Lorentzian function, which can be used to determine the stiffness of an optical trap (Neuman and Block, 2004; Svoboda and Block, 1994a). The real part of the complex transfer function is calculated by evaluating the Kramers-Kronig dispersion relation (Landau, et al, 1980; Ohta and Ishida, 1988), such that

$$h'(\omega) = \frac{2}{\pi} P \int_0^{\infty} \frac{\omega' h(\omega')}{\omega'^2 - \omega^2} d\omega' = \frac{2}{\pi} \int_0^{\infty} \cos(\omega t) \int_0^{\infty} h''(\omega') \sin(\omega' t) d\omega' dt, \quad (5.8)$$

where P denotes a principal-value integral. The integrals in equation 8 can be evaluated numerically; however, care must be taken in interpreting $h'(\omega)$ because the cosine and

sine transforms of finite samples can lead to discontinuities or nonsensical data corresponding to the smallest and largest frequencies studied. For this reason, the first and last data point of the storage and loss moduli were excluded from the data below.

Once calculated, the frequency-dependent h' and h'' are used to determine the real and imaginary components of the complex shear modulus (equation 5.5). However, care must be taken when interpreting G' because it will contain information about both the elastic behavior of both the trap and the surrounding viscoelastic medium. Since the trap behaves as linear spring, its contributions to the storage modulus are constant over all frequencies. Thus, the effects of the trap can be subtracted from the calculated or observed storage modulus, G'_{obs} , to reveal the true storage modulus

$$G' = G'_{obs} - \frac{\alpha}{6\pi r}. \quad (5.9)$$

In the case of water, the observed storage modulus simply equals the constant contribution from the trap. If the spring constant is not previously known, it can be inferred from the observed data because the contributions from the trap will dominate the elastic contributions from the surrounding medium at low frequencies (Addas, et al, 2004). For a generalized viscoelastic fluid, there are no analytical expressions for $G'(\omega)$ and $G''(\omega)$. However, for a bead trapped in a purely viscous solution such as water, $G'(\omega) = 0$ and $G''(\omega) = \omega\eta$.

Finally, the empirical Cox-Merz rule (Manero, et al, 2002) can be used to relate a viscoelastic medium's G' and G'' to its complex viscosity

$$\eta^* = \left[\left(\frac{G'(\omega)}{\omega} \right)^2 + \left(\frac{G''(\omega)}{\omega} \right)^2 \right]^{1/2}. \quad (10)$$

With this method, the dependence of the optical trap response on the viscosity and elasticity of a medium can be used to probe complex fluids, such as methylcellulose and actin networks.

Methylcellulose

Methylcellulose is a hydrophobically modified, nonionic cellulose derivative in which 50-60% of the native hydroxyl groups in the sugar monomer have been replaced by methyl groups, allowing it to become water soluble (Kobayashi, et al, 1999; Li, et al, 2002; Zheng, et al, 2004). Methylcellulose has been extensively used in research efforts aimed at understanding of the mechanics and dynamics of cellular organisms. For example, it has been employed to study actin-based springs (Shin, et al, 2007) bacterial flagellar motors (Berg and Turner, 1979), and the actin-based motility of a bacterial pathogen (McGrath, et al, 2003). In these applications, methylcellulose was used to slow biological processes or to estimate their force exerting capabilities. Interestingly, methylcellulose has also been observed to increase the swimming velocity of some non-flagellated bacteria (Gilad, et al, 2003; Shaevitz, et al, 2005). The rheology of methylcellulose has been mainly studied at the macro scale with parallel plate

rheometers. Even though many advances have been made with such approaches, which have focused on methylcellulose's interesting gelation behavior (Desbrieres, et al, 2000; Kobayashi, et al, 1999; Li, et al, 2002; Schmidt, et al, 2003; Ward and Sweeney, 2004; Zheng, et al, 2004), little is known about the microrheology of methyl cellulose and how it affects cellular processes.

Methylcellulose solutions were prepared by dissolving methylcellulose powder (Sigma, 63,000 MW) in water heated to 80 °C and allowing the solution to thermally equilibrate to room temperature before curing overnight at 4 °C. The index of refraction of the solutions was found to be minimally dependent on methylcellulose content (Table 5.1). In addition, the contribution of the optical trap to the observed storage modulus was approximately the same in all the solutions tested (results not shown), a result that is consistent with the glycerol data presented above.

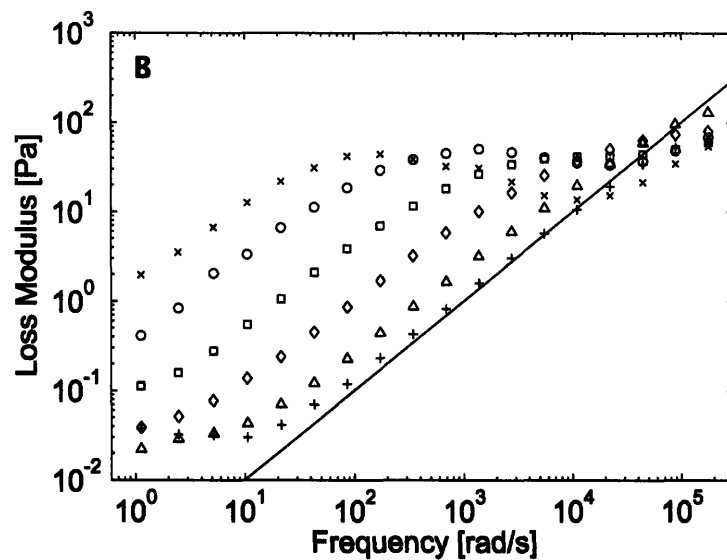
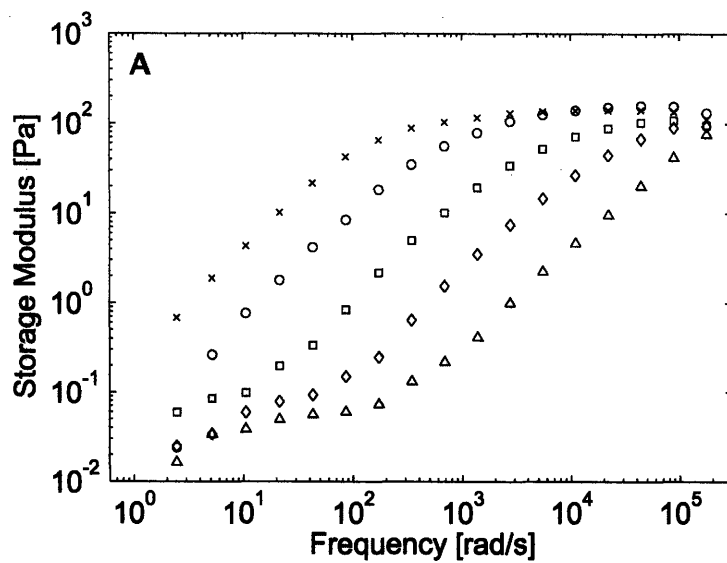
In this report, we applied the theoretical framework described above to characterize the frequency-dependent microrheological behavior of methylcellulose with optical tweezers using 490 nm glass beads. For different methylcellulose concentrations, the storage modulus increases monotonically with frequency and methylcellulose content until plateauing at approximately 150 Pa (Figure 3a). The frequency-dependent portion of the curves scale as $G' \sim \omega^{1.1}$, while polymer theory predicts that $G' \sim \omega^2$ (Doi and Edwards, 1986). Although the reasons for this behavior are not entirely clear, it is possible that the beads are interacting with the methylcellulose chains, leading to depletion zones (Chae and Furst, 2005; Starrs and Bartlett, 2003). In addition, optical traps that are relatively

stiffer than the surrounding medium may lead to inaccurate storage modulus measurements (equation 5.9). Furthermore, these measurements are affected by low frequency noise contributions from the optical trap that reduce the reliability of modulus values below 0.1 Pa (Figure 5.3). Nevertheless, the overall trends expected from polymer theory are observed in the data (Doi and Edwards, 1986).

The same experimental framework was employed to measure the loss modulus of methylcellulose. The loss modulus for the different concentrations of methylcellulose was shown to scale as $G'' \sim \omega^1$, as expected from polymer theory (Figure 5.3) (Doi and Edwards, 1986). At low frequencies, the loss modulus of methylcellulose increases with methylcellulose concentration, indicating that the viscosity of the solution increases as well. This behavior is continued at high frequencies for low concentration methylcellulose solutions. The loss modulus of the 3% solution, however, reaches a maximum at approximately 100 rad/s, before decreasing to a minimum at $\sim 10^4$ rad/s and increasing again at higher frequencies (Figure 5.3). A similar behavior is observed for the 2% solution. This phenomenon is typical of entangled polymer networks, where, at low frequencies, the polymer motion is described by reptation, and, at high frequencies, individual polymer vibrations dominate their behavior (Doi and Edwards, 1986; Larson, 1999). The transition between these dissipation modes causes the nonlinear behavior in high content methylcellulose solutions.

The time-dependent behavior of the measured storage and loss moduli can be used to determine the time-dependent viscosity of the solutions using the Cox-Mertz rule

(Figure 5.3). At low frequencies, the viscosity of methylcellulose remains constant and correlated to methylcellulose content, while at higher frequencies the viscosity decreased and scales as $\eta \sim \omega^{-1}$. This decrease, known as shear-thinning, occurs at high frequencies because the polymer network is not allowed to relax, making it easier for individual polymers to slide past each other (Doi and Edwards, 1986). Shear-thinning is especially pronounced in high concentration solutions, though our results also show apparent shear-thinning in low concentration solutions. Theoretically, the methylcellulose solutions should shear-thin until reaching the viscosity of water, but this high-frequency behavior was not observed because of instrument acquisition limitations above 100 kHz. In addition, the low methylcellulose content solutions, including water, appear to have a low frequency shear thinning regime. This is an artifact corresponding to low frequency instrument noise, which also affects the modulus measurements presented above and is captured by the PSD of bead motion in the low methylcellulose content solutions. As the viscosity of the solution increases with methylcellulose content, the low frequency component of bead motion increases as well and effectively hides the low frequency instrument noise, reducing such effects in these measurements. Alternatively, these artifacts may be avoided with the use of a weaker trap (results not shown).



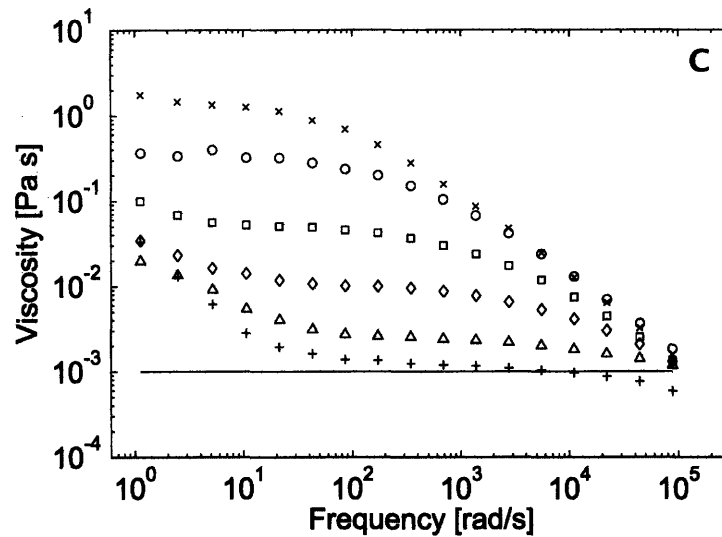


Figure 5.3 Properties of methylcellulose solutions: + (0%, Water), Δ (0.1%), \diamond (0.5%), \square (1%), \circ (2%), \times (3%). (a) The frequency dependent storage modulus increases with methylcellulose concentration and exhibits a plateau modulus of approximately 150 Pa. (b) The loss modulus also increases with methylcellulose concentration. The 2 and 3% solutions exhibit significant reptation behavior. The theoretical curve for pure water ($G'' = \omega\eta$) is indicated by a solid line. (c) The dynamic viscosity of methylcellulose, as determined with the Cox-Mertz rule, exhibits a shear-dependent behavior. The theoretical viscosity for pure water ($\eta = 0.001$ Pa s) is indicated by a solid line. Low-frequency instrument noise makes modulus measurements lower than 0.1 Pa unreliable.

Conclusions

We have applied optical tweezers to measure the microrheological properties of various substrates. Passive microrheology methodologies were outlined, described, and used to measure the storage and loss moduli of methylcellulose solutions. In addition, we imparted Stokes drag on optically trapped beads to measure the viscosity of different water-glycerol mixtures, which were found to have different indices of refraction. The effects of these differences in index of refraction on the stiffness of the optical trap were calculated and a simple empirical model for these effects was introduced.

As demonstrated by these applications, optical tweezers are a versatile tool with a measurement bandwidth that expands over 5 decades; however, important considerations must be taken into account when using them to study the microrheology of complex fluids. For example, the bead size, material, and surface chemistry must be carefully considered because they will dictate interactions with the surrounding medium and the optical trap. In the case of a polymer network, beads that are smaller than the mesh size of the network will fail to probe the properties of the network. On the other hand, beads that are too large may compromise the spatial resolution of the position detection system where small fluctuations may become undetectable and lead to an overestimation of the properties of the material of interest (results not shown). In addition, bead surface chemistries may create depletion zones around the bead, effectively isolating the bead from the network (Chae and Furst, 2005; Starrs and Bartlett, 2003), or may increase the binding interactions between the bead and the network, a situation that may or may not be desired. Finally, the bead material will dictate its index of refraction, which ultimately determines the ability and stiffness with which the bead will be trapped.

Another important point to consider is the stiffness of the optical trap. As shown above (Figure 5.2), the stiffness of the trap is dependent on the power of the trapping laser and the index of refraction of the bead and surrounding medium. Even though the properties of the surrounding medium will not affect the force-exerting capabilities of the trap, they will influence the motion of trapped beads, a fact that is exploited in the passive microrheology technique outlined above. Nevertheless, weak traps that minimally

influence bead motion are typically better suited in these experiments because their contributions to the observed storage modulus are reduced. If the trap is relatively stiff compared to the storage modulus of the surrounding medium, measurements of the medium's storage modulus will be inaccurate. In addition, weak traps can help bury instrument noise by permitting low frequency bead motion, thus improving the accuracy of the measurements at low frequencies. On the other hand, stiffer traps may be desired when employing active microrheology techniques with optical tweezers. These methods usually rely on dragging trapped beads through the material of interest and, therefore, require large forces to deform the surrounding medium and make measurements accurate.

Chapter VI

Exploring the Mechanome

Abstract

Optical tweezers and single molecule fluorescence are finding increasing applications in the exploration of the mechanome. In this chapter, we present four applications of the instrumentation developed in Chapter II. The first application of the IOFF instrument is to study the effects that IOFF may have on the photochemical behavior of different fluorophores. Results show that IOFF improves the longevity of all fluorophores that are susceptible to enhanced photobleaching in the presence of an optical trap. In addition, the data suggests that reverse intersystem crossing may occur when the optical trap and the fluorescence excitation laser are alternately modulated. The second application measures the statistical mechanical properties of filamentous phage and presents it as an alternative to dsDNA tethering in single molecule assays. Phage is shown to be much stiffer than dsDNA, as evidenced in their respective fits to the wormlike chain model. The third application presents a novel combination of optical and magnetic tweezers to measure the rheological properties of the leading and trailing edges of cells that have been primed for migration. Results show that the leading edge is approximately twice as stiff as the trailing edge, suggesting that cellular polarization leads to intracellular mechanical differences. Finally, the fourth application uses an

optical trap to trigger the acrosomal reaction in horseshoe crab sperm. This biological spring is an striking example of actin based motility in the absence of ATP. These experiments underscore the importance of the mechanome and highlight the importance of forces in biology.

IOFF Improves Fluorophore Longevity

(This section was adapted from a manuscript in preparation by Ding, et al.)

Introduction

The combination of optical tweezers and single molecule fluorescence techniques into a simultaneous, single tool allows for the direct observation of molecular changes as mechanical forces are applied while locating such changes with sub-nanometer resolution. This combined instrument can be used to explore the interactions of biomolecules, such as proteins, DNA and molecular motors (Cornish and Ha, 2007; Ishijima and Yanagida, 2001; Lang, et al, 2003). However, until recently, the combination of optical tweezers with single molecule fluorescence had proven difficult because the high photon flux of the trapping beam accelerates the photobleaching of fluorophores, dramatically reducing the time to perform a meaningful measurement to only a few seconds (Brau, et al, 2006; Lang, et al, 2004; van Dijk, et al, 2004). This problem was circumvented by the development of a novel technique, termed interlaced optical force-fluorescence (IOFF), that reduces trap-induced photobleaching by alternately modulating the optical trapping and fluorescence excitation beams without compromising the trap integrity (Brau, et al, 2006). This technique, which is not limited

to particular experimental geometries, results in a 20-fold improvement in the fluorescence longevity of Cy3 when compared to the simultaneous exposure to the trapping and excitation lasers. The feasibility and versatility of IOFF was later demonstrated in the combination of optical tweezers with the powerful tool of fluorescence resonance energy transfer (FRET) by observing the opening and closing of a DNA hairpin with a Cy3-Alexa647 pair (Tarsa, et al, 2007). Here we investigate the applicability of this technique to a variety of fluorophores commonly used in single molecule biophysics measurements.

In this report we study the effects of accelerated photobleaching due to the trapping beam on 100 nm beads coated with fluorophores and quantify the improvement of the photobleaching rate when using IOFF. We demonstrate that fluorophores with absorption maxima around 488 nm are not affected by the trapping laser. On the other hand, fluorophores with an absorption maxima of 532 nm and 635 nm are most affected, but exhibit a dramatic fluorescence longevity improvement with our technique. Surprisingly, when IOFF is employed, the longevity of some of these dyes exceeds their longevity in the absence of the trap. We hypothesize that this behavior may be evidence of reverse intersystem crossing, one of the so-called forbidden transitions in which an electron goes from a triplet state back to a singlet state.

Materials and Methods

The instrument platform, which is described elsewhere (Brau, et al, 2006), was outfitted with fluorescence excitation laser at 488, 532, and 635 nm. In addition, the function

generator used to alternate and synchronize the trapping and fluorescence excitation laser beams was replaced by a field programmable array board.

Beads coated with the appropriate fluorophore were nonspecifically immobilized on the surface of a coverslip in a flow cell. Measurements were made by precisely centering fluorophore-coated beads at a location in the specimen plane corresponding to the pinhole aperture with an automated routine using the detection laser and the piezo-electric stage. The beads were then exposed to either in-phase (IP) or out-of-phase (OP) irradiation conditions (Brau, et al, 2006), corresponding to the simultaneous or alternately gating of the trapping and fluorescence excitation lasers, respectively, and their fluorescence emission was recorded for 5 minutes. As a control condition termed NT, the beads were exposed to the fluorescence excitation laser in the absence of the trapping laser. All experiments were carried out in 20 mM Tris, pH 7.5, 6 mM NaCl, 1.7 mM MgCl₂, 10% glycerol, 120 nM catalase, 25 mM β -D(+) glucose, 1.8 μ M glucose oxidase, 1% β -mercapto-ethanol (degassed for 30 minutes in a desiccator). The small size of the beads ensured that they were completely bathed by the irradiation of the trapping laser, with a diffraction limited focused waist on the order of 500 nm, and the fluorescence excitation laser, which had a zone of \sim 20 μ m. In addition, the concentration of immobilized beads was low enough to ensure that the fluorescence emission collected from a single bead was not contaminated from fluorescence from neighboring beads. All signals are acquired at 20 Hz using custom LabView software and analyzed with MATLAB.

Results and Discussion

Biotin-coated beads were saturated with the following streptavidin-conjugated fluorophores: fluorescein, Alexa488, Alexa532, Alexa555, Cy3, TMR, quantum dot 666, Alexa647, and Cy5. The photochemical behavior of GFP was explored as well, although it was immobilized via a hexahistidine motif on its N-terminal to beads coated with anti-His antibodies. Beads coated with each fluorophore were exposed to the NT, OP, or IP modulating conditions, and their fluorescence emission was monitored with a silicon avalanche photodiode. The recorded decay curves were well described by double exponential function, but the multitude of fitting parameters made it difficult to make a meaningful comparison between the fluorophores. Instead, a single parameter was used: the integration of each curve. Since all curves were normalized, higher integration values indicate a longer lived fluorophore, while low integration values indicate a short lived fluorophore.

Results show that the IOFF technique is most effective on those fluorophores excited with 532 nm and 635 nm. All of these fluorophores exhibit substantial enhanced photobleaching in the IP condition, relative to NT. However, this fast photobleaching in the presence of the trap is greatly improved with the OP condition, 2 to 17-fold, relative to the IP condition (Figure 6.1). In contrast, the fluorophores with an absorption maxima around 488 nm were insensitive to the effects of the trapping laser, as they did not exhibit shorter longevities for the IP condition (Figure 6.1). Nevertheless, these fluorophores photobleached at the fastest rate, even in the absence of the trap, as their integration values were no more than half of those from the fluorophores excited at

longer wavelengths (results not shown). Therefore, it is possible that any photobleaching effect from the trapping laser is obscured by their inherently fast decay rate.

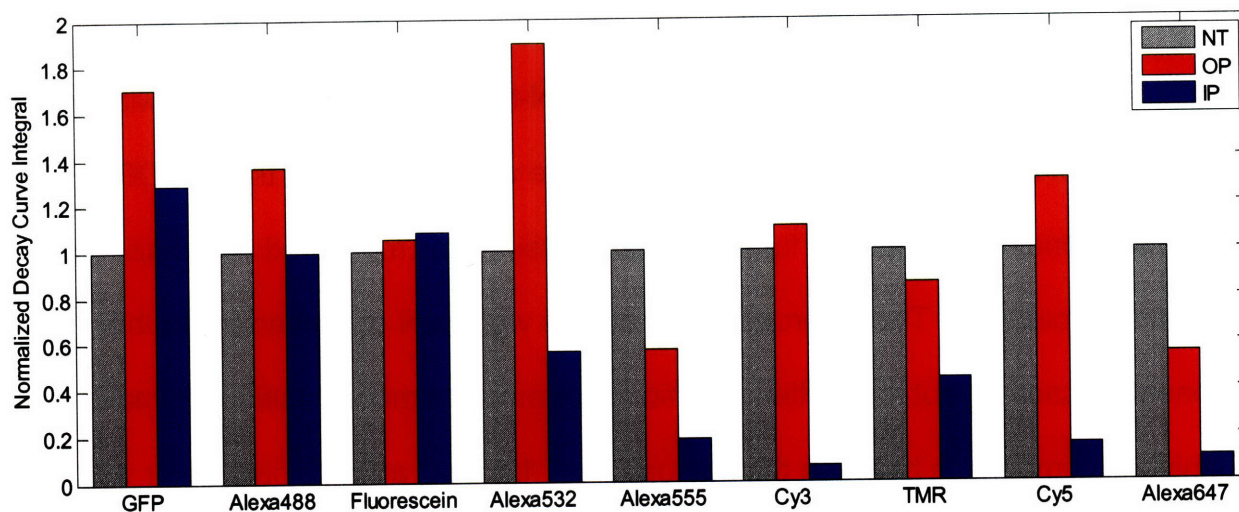


Figure 6.1 Effects of IOFF on the photobleaching decay rate of different fluorophores. Results show that fluorophores whose absorption maxima correspond to 488 nm excitation (GFP, Alexa488, and fluorescein) are not susceptible to accelerated photobleaching. In contrast, fluorophores exposed to a 532 or 635 nm excitation source photobleach considerably faster in the simultaneous presence of the optical trap. Interestingly, some of the fluorophores show a slower rate of photobleaching in the OP condition than in the absence of the trap, NT.

For those fluorophores excited with wavelengths of 532nm and 635 nm, Cy3 is the most affected by the accelerated photobleaching resulting from the presence of the trapping laser, showing 17-fold decrease in fluorescence longevity from NT to IP modulations. However, Cy3 is also the fluorophore whose fluorescence longevity is improved the most with the IOFF technique, recovering back its fluorescence to NT levels with OP modulation. In this range of wavelengths, the fluorophore least affected by trapping laser is TMR and shows a 2-fold improvement in fluorescence longevity with the IOFF technique. Data for quantum dots with an absorption maximum at 532 nm indicate that it

is the longest lived fluorophore studied and that it is insensitive to the NT, IP, or OP modulation schemes (results not shown).

Interestingly, some of the fluorophores exhibit a slower decay rate in the OP condition than in the absence of the trap. This unexpected result may suggest that some of the dyes are undergoing reverse intersystem crossing. Even though it is considered a forbidden electronic transition, there is mounting evidence that this phenomenon may actually be possible (Larkin, et al, 2002). For the IOFF configuration, once an electron finds itself in a triplet state, it is possible that the lower energy trap photons may kick it off into a higher energy singlet state, from where the electron can return to the ground state. This effectively diminishes the population of electrons that are susceptible to photobleaching, making the fluorophores longer lived, as observed in some of the cases presented above (Figure 6.1).

Single M13 Bacteriophage Tethering and Stretching

(This section was adapted from Khalil, et al, 2007.)

Introduction

The Ff class of filamentous bacteriophage, composed of the structurally akin species f1, fd, and M13, has elicited the interest of many wide-ranging scientific communities because of its self assembling nature. Protected and transported within the highly organized protein-based capsid is the structural and assembly information necessary for its own production. This structural feature provides a direct and accessible link between

phenotype and genotype, which particularly in the case of M13 bacteriophage, has proven advantageous for numerous studies and applications. For instance, combinatorial libraries of polypeptides can be fused to M13 coat proteins, in a technique known as phage display, as a means of screening binding candidates against targets (Barbas, 2001). Recently, targets have been extended beyond biologicals to a wide variety of inorganics, in efforts to discover biological systems capable of organizing and growing materials (Whaley, et al, 2000). In addition to serving as the vehicle for displaying these ligands, the unique structure of M13 itself has been exploited as a biological template for nanotechnology, such as in the directed synthesis of semiconducting/magnetic nanowires and lithium ion battery electrodes (Mao, et al, 2003; Mao, et al, 2004; Nam, et al, 2006). Considering its utility as both a genetic blueprint and structural backbone for materials and device architecture, a better understanding of its mechanical behavior and a novel means of actively assembling M13 can greatly advance the design of future M13-based materials.

In this report, we introduce M13 as a strong and versatile biopolymer alternative to dsDNA in constructing the instrumental tethered bead assay. First, we demonstrate a robust method for generating M13 tethers in solution. Second, we investigate the SM elasticity via optical tweezers stretching and modify the appropriate limit of the wormlike chain (WLC) model to accurately capture force-extension (F - x) measurements. Finally, we discuss significant features and extensions of this system.

Results

The elastic properties of M13 are critical to its use as a single molecule tool. In an effort to characterize them, the opposing ends of individual M13 molecules were modified with biotin and hexahistidine motifs, respectively. M13 tethers were then stretched with a high-resolution optical trap using procedures similar to those for short dsDNA tethers (Wang, et al, 1997) in an instrument described elsewhere (Brau, et al, 2006). Briefly, 440-nm-diameter polystyrene beads, affixed to proximal ends of M13, were trapped by the optical gradient forces of a tightly focused laser beam and positioned at a set height above the coverslip surface (Figure 6.2). The piezo-electric stage was then translated laterally while bead displacements from the trap center were recorded, and, with the necessary calibrations (Svoboda and Block, 1994a), these results were converted to F - x measurements.

Stage-based stretching of M13 molecules with optical trap stiffness in the range of 0.25–0.35 pN/nm gave F - x measurements from fractions of a pN up to 30–40 pN. Despite its hierarchical structure, M13 F - x behavior was reminiscent of typical WLC biopolymer stretching (Figure 6.2). In fact, plotted alongside a typical F - x curve for a 3,500-bp dsDNA molecule, stretched by identical procedures, the M13 response appeared very similar to that of dsDNA (Figure 6.2). After a small entropic elasticity regime, the thermal random-walk fluctuations governing the filament's orientation were stifled and its end-to-end distance approached its contour length, or the B-form length in the case of dsDNA. Just before the molecule reached its contour length it began to

display compliance, and enthalpic stretching, or simply linear elasticity, accounts for actual polymer extension. Interestingly, investigation at higher forces showed that M13 experiences no abrupt overstretching transitions, as does dsDNA at 60–65 pN (results not shown) (Smith, et al, 1996). In all instances, the F - x response was reversible and showed no plasticity or permanent deformation.

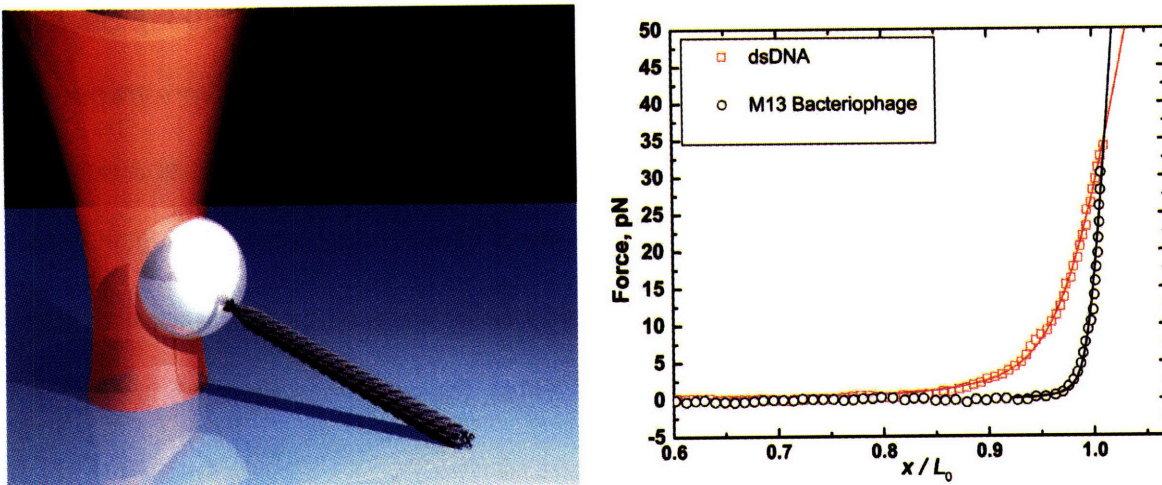


Figure 6.2 Single M13 bacteriophage stretching. (A) Rendering of M13 bacteriophage stretching by an optical trap (not to scale). The M13 end proximal to the bead contains a biotin motif, while the end attached to surface contains a hexahistidine. (b) F - x comparison of M13 bacteriophage and dsDNA. A typical F - x measurement for M13 bacteriophage (black o) with a corresponding WLC fit overlaid on the data. The M13 behavior is suggestive of a stiffer analog to 3500 bp dsDNA, for which a typical F - x measurement (red \square) is plotted along with its corresponding WLC fit.

Comparing the stretching curves of a 3500 bp segment of dsDNA and of a M13 tether reveals that bacteriophage is much stiffer than dsDNA. Even though both tethers had comparable contour lengths, on the order of 1 μm , fitting them to the appropriate form of the worm-like chain model (Khalil, et al, 2007) revealed that the persistence length of M13 is 30 times larger than dsDNA (1265 nm vs. 42 nm). Furthermore, the elastic stretching modulus of M13, 2.18 nN, doubles dsDNA's, 1.02 nN. These results show

that M13 is a much stiffer tether than dsDNA, and, considering M13's genetic versatility, suggest that M13 should be considered as an alternative tether when developing force spectroscopy assays.

Discussion

A significant challenge in single molecule biophysics research is in developing creative and trustworthy assays to link the biological problem of interest to the high-resolution instruments responsible for detection and manipulation. In this report, the characterization of the single molecule elasticity of filamentous bacteriophage was presented. The appropriate form of the WLC was equipped with an elastic chain stretching term and then used to model optical tweezers stretching data. The extracted mean persistence length, 1,265 nm, supports recent predictions that filamentous bacteriophage persistence lengths may be shorter than previously thought (Lau, et al, 2002). The M13 system appears well suited for higher force studies, such as for protein extension and distortion, particularly now that the force capability of optical tweezers is increasing (Mills, et al, 2004). In contrast to dsDNA, phage showed no deviation from standard entropic/enthalpic stretching when subjected to loads through 70 pN. Nonetheless, in optical tweezers-based studies, dsDNA is commonly used to translate forces to a protein of interest (Cecconi, et al, 2005). The M13 template may be better able to communicate these forces because it is stiffer (longer persistence length and higher elastic stretching modulus) than DNA. Furthermore, the M13 template can provide multiple, localized attachments to the species of interest to prevent or delay detachment.

Intracellular Mechanical Variances in Polarized Cells

(This section was adapted from Su, et al, 2007.)

Introduction

Cellular locomotion is a very complex process requiring the concerted coordination of many biochemical pathways. During migration on surfaces or in tissue matrices, the cell body becomes polarized in the direction of motion, resulting in a leading protruding edge and a trailing retracting edge. These changes in cell morphology have been related to changes in actin dynamics, particularly in the leading and trailing edges where actin is actively polymerized and depolymerized, respectively. Recent studies have shown that the mechanical properties of cells are correlated to actin networks (Haga, et al, 2000); however, the rheology of polarized migrating cells has never been measured. In fact, even though there is a rich literature on actin dynamics as well as on the molecular biology factors affecting cell polarization and migration (Lauffenburger and Horwitz, 1996; Mitchison and Cramer, 1996; Pollard and Borisy, 2003), there is very little known about the rheology of migrating cells. Furthermore, the fundamental question of whether cells become softer or stiffer during migration is subject to considerable debate (Cramer, et al, 2002; Kole, et al, 2005). In this report, we use soft lithography techniques in combination with optical tweezers and magnetic tweezers to control the shape of adherent cells and probe the location-dependent rheological properties of cells primed for migration (Jiang, et al, 2005).

In order to better measure the local intracellular rheological properties for a cell poised for migration, we use cells polarized using microfabrication and a magnetic microrheometer combined with optical tweezers. Magnetic rheometry is typically employed to study the rheology of cells because it is capable of accessing the high forces, on the order of nN, needed to deform cellular structures. However, they are not capable of stably trapping and placing objects at desired locations. Conversely, optical tweezers provide precise positioning ability, but they are best suited to probe the force regimes experienced by single molecules at the pN level and thus cannot provide the high forces needed to measure the full range of cellular rheological properties. In our approach, fibronectin coated superparamagnetic beads are first trapped and positioned with optical tweezers at the desired location of immobilized cells. The beads are then allowed to endocytose and later pulled upon with magnetic tweezers.

Optical-Magnetic Rheometer Setup

Several reports have demonstrated optical tweezers capable of trapping metallic beads. A particular study found that Rayleigh size gold particles (36 nm) are trapped stronger than similarly sized latex particles (Svoboda and Block, 1994b). The dominance of the gradient force for these particles was attributed to the larger polarizability of metals; however, unfavorable force balances are expected for particles larger than 40 nm. This result is at odds with a later report stating that superparamagnetic and polystyrene beads with 2.6 μm diameters can be optically trapped with the same force (Romano, et al, 2003; Sacconi, et al, 2001). This study featured a magneto-optic trap in which a custom magnetic manipulator was built around a water immersion objective to rotate

optically-trapped superparamagnetic particles. Similar magneto-optical tweezers arrangements have also been developed, with a particular design used to intertwist two DNA molecules attached to a paramagnetic bead (Claudet and Bednar, 2005) and another to measure liquid-crystal-mediated forces between spherical superparamagnetic beads (Kotar, et al, 2006). Here we develop technology to combine the trapping capabilities of optical traps with the high-force exerting capabilities of magnetic tweezers to measure the rheological properties of adherent cells.

The optical tweezers platform (Figure 6.3) is similar to previous designs (Brau, et al, 2006; Lang, et al, 2004), but it employs a 975 nm light source as the trapping laser. In this design, double-trap capabilities were achieved by splitting and recombining the main laser line with two polarizing beam-slitting cubes (CVI). The amount of power delivered to each trap was controlled with a half-waveplate.

Beads were initially placed on and bound to the cells (Figure 6.4) by holding the beads for approximately 15 minutes with a power of 1mW. Laser powers were measured before the beam entered the microscope. After binding the beads to the appropriate cell region, a box around the cell of interest was drawn for later identification (and bead manipulation with magnetic tweezers) by burning the gold surface with at least 55 mW of power. In addition to optical losses through the objective, the gold and titanium-coated plate was observed to only transmit approximately 15% of the laser light. The optical trap was calibrated by using the Stokes drag method (Svoboda and Block,

1994a) and the stiffness of the trap was calculated to be approximately 0.28 fN/nm for 4.5 micron superparamagnetic beads at 4mW of power.

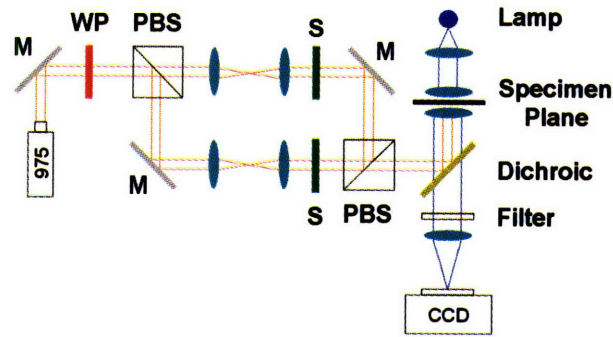


Figure 6.3 Optical tweezers schematic. M = mirror, PBS = polarizing beam splitter, S = shutter, WP = half-waveplate. Two optical traps were formed by splitting and recombining a 975 nm laser line and guided them into the objective with a dichroic mirror. One of the traps was formed with low power, ~ 5 mW, and was used to trap superparamagnetic beads and position them on specified surface or cellular locations. After the beads were immobilized on cells, the other trap was formed with high laser power, > 55 mW, and was used to mark the substrate around the cell of interest for later identification and manipulation with magnetic tweezers.

The magnetic trap is based on a design described elsewhere (Huang, et al, 2002). It was calibrated by dragging a magnetic bead in a solution of polydimethylsiloxane under different forces. For cellular rheology experiments, cells were kept at 37 °C through the use of both a temperature controlled stage and an objective heater. For each experiment, a 5-second step-forcing function of approximately 20 nN of force was applied. The regional shear modulus was calculated as previously described (Schnurr, et al, 1997; Su, et al, 2007) and was evaluated at 0.05 Hz, a time scale longer than the relaxation time of the cell (Su, et al, 2007). The position of the bead was tracked over

time using a custom particle-tracking program described previously (Lammerding, et al, 2003).

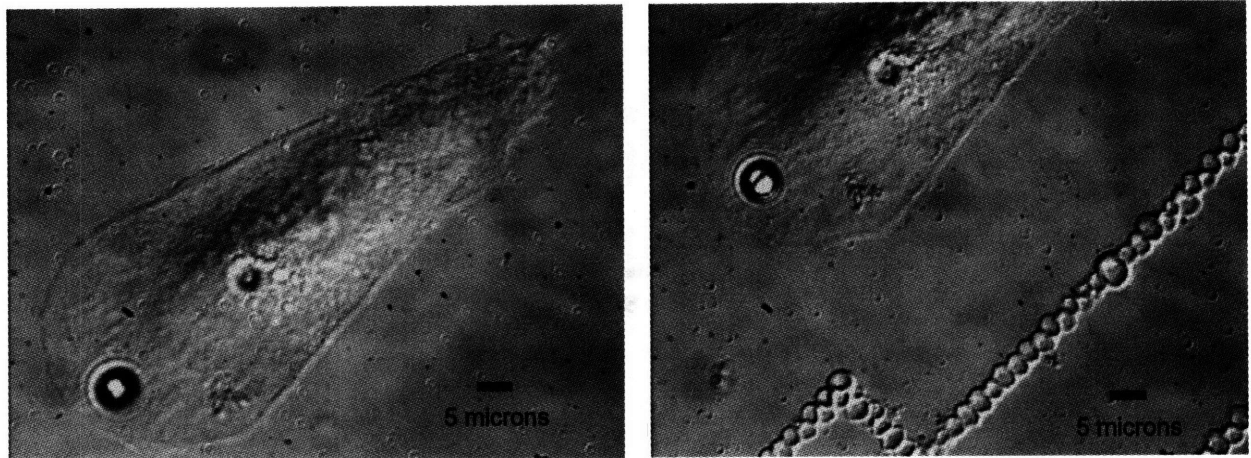


Figure 6.4 Positioning a magnetic bead with an optical trap on the leading edge of a polarized cell (left) An optically trapped magnetic bead is placed on the leading edge of a patterned cell. (right) After placement, the gold substrate in the surface is burnt with the trapping laser for ready identification of the cell in subsequent experiments.

Results and Discussion

The resulting shear modulus at the leading edge was found to be a factor of ~ 1.9 stiffer than the trailing edge and a factor of ~ 2.4 stiffer than the nucleus (Figure 6.5). Earlier experiments performed on cells adhered to micropatterned islands of increasing size found that their shear modulus was biphasic with pattern diameter while cell height was monotonic (Su, et al, 2007). From this we conclude that cell height while potentially a contributor is not the determining factor of cellular shear modulus. The result that the nucleus is softer than the leading edge qualitatively confirms AFM results by Haga and coworkers with the exception being that AFM results report that the nucleus is a factor of 10 softer than surrounding regions. We attribute this difference in part to the fact that

the AFM probes the surface whereas the optical-magnetic trap probes the interior of the cell surrounding an endocytosed bead.

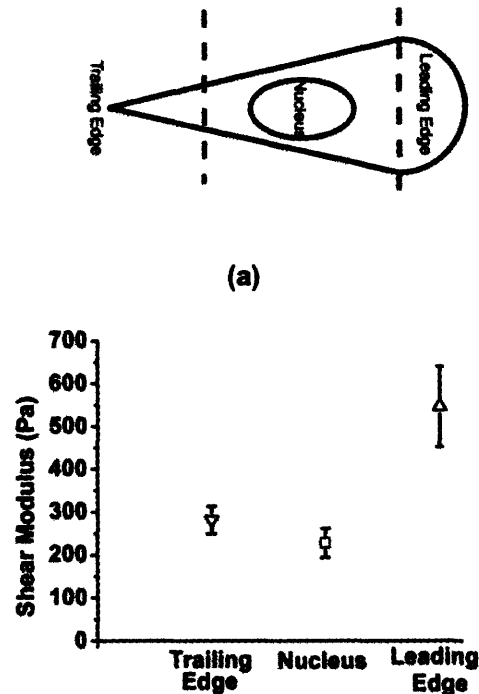


Figure 6.5 Rheological variances in polarized cells. (a) Schematic of cell with different regions defined. The teardrop is 103 microns long and 30 microns in diameter at the widest part (b) Shear modulus at different cellular locations ($n = 5$). Error bars represent the standard error of the mean.

Our results are consistent with previous AFM surface measurements, (Haga, et al, 2000; Heidemann and Wirtz, 2004) that adherent cells are mechanically differentiated in their different regions. Other work (Kole, et al, 2005) has demonstrated using intracellular microrheology that the leading edge of Swiss 3T3 fibroblasts is stiffer than the perinuclear region. We observe in addition to the differences in stiffness between the leading and trailing edge, that the nuclei of NIH3T3 fibroblast cells are softer than the surrounding cytoplasm by a factor of ~ 2.4 . Our values for the Young's modulus at the leading edge are on the order of 1000 Pa which agrees with the modulus needed by

the Brownian ratchet model to predict the forces generated from the polymerization of actin filaments in the lamellipodia (Kole, et al, 2005). In addition, it has been shown that a cell poised for migration is softer than a quiescently resting cell (Su, et al, 2007) demonstrating the mechanical properties change upon the onset of migration. These results contradict with results by Kole et al, 2004, who obtained Young's moduli on the order of 10 Pa and whose stiffness results for quiescent cells were larger than for migrating cells.

The Force of an Actin Spring

(This section was adapted from Shin, et al, 2007.)

Introduction

The acrosome reaction in sperm cells of horseshoe crab *Limulus polyphemus* provides a spectacular example of nontraditional actin motility. To initiate fertilization, *Limulus* sperm cells must penetrate two layers surrounding the egg, an outer basement lamella ~ 5 μm thick and an inner vitelline envelope ~ 35 μm thick. Sperm cells penetrate this physical barrier by uncoiling and extending a 60 μm long bundle of actin (Brown and Humphreys, 1971). Structural analysis reveals that, before reacting, the acrosome bundle consists of a paracrystalline array of bent, twisted actin filaments bound to two proteins—scruin and calmodulin. In the presence of Ca^{2+} , scruin changes conformation (Sanders, et al, 1996), causing the individual actin filaments to untwist and extend to a homogeneous, straightened bundle (Tilney, 1975). Interestingly, this motility does not involve ATP hydrolysis or a myosin motor protein (Shin, et al, 2003; Tilney, 1975).

Studies have revealed that the force underlying this motility is a spring-based mechanism in which mechanical energy is stored in slight but concerted overtwists of the actin filaments in the bundle (Derosier, et al, 1980; Schmid, et al, 2004; Shin, et al, 2004). Thus, the *Limulus* sperm acrosome bundle is a mechanochemical spring where the relevant displacement governing force generation arises from an overtwist rather than from a rectilinear extension or compression from equilibrium.

In this work, we measure force generated by the *Limulus* acrosome reaction by using methylcellulose as a viscoelastic thickening agent to mechanically slow down the extension rate of the acrosome bundle. This method yields a lower bound estimate of the acrosome reaction force, but provides an independent verification of stall forces measured in agarose (Shin, et al, 2007). This work provides the first estimate of the force associated with the mechanochemical conformation change in a bundle of actin.

Materials and Methods

Typically, the acrosome reaction in the *Limulus* sperm, as well as in other marine invertebrate sperm, is triggered by flowing calcium ionophore, which transports extracellular Ca^{2+} into the cytoplasm. Our recent finding has shown that a tightly focused 488 nm laser capable of forming an optical trap can also induce the acrosome reaction when it is used to irradiate certain regions of the sperm cell. For efficient triggering, we focus the beam to a diffraction-limited spot using a 100X 1.4 NA microscope objective. Measured immediately before entering the objective lens, the beam intensity is ~ 7 mW. Compared to the traditional use of calcium ionophore for

activation, our newly discovered laser irradiation technique allows us to trigger the acrosome reaction on selected cells on demand (Figure 6.6).

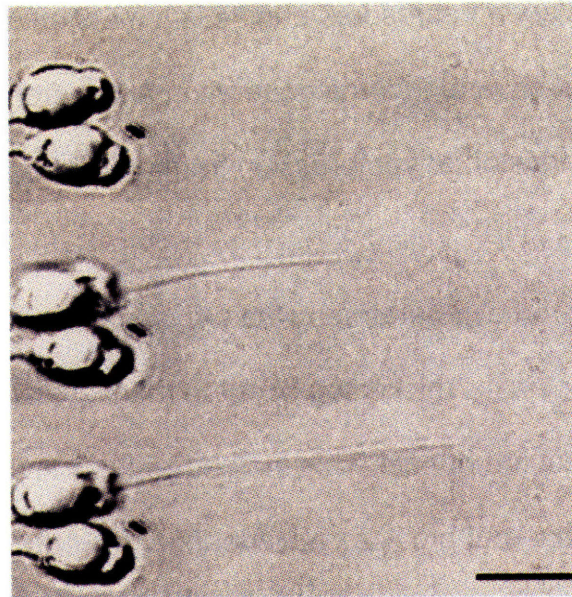


Figure 6.6 The acrosome reaction in *Limulus* sperm. Upon laser activation, a sperm cell extends the acrosome bundle to a final length a length of 50–60 μm in artificial sea water (scale bar $\sim 5 \mu\text{m}$).

We use methylcellulose solutions to mechanically slow down the acrosome reaction. To determine the viscosity of each solution, we apply a Stokes' drag force to a laser-trapped $0.5 \mu\text{m}$ diameter glass bead in methylcellulose media. This method probes a length-scale comparable to that of the bundle diameter, a factor not shared by more conventional rheology methods. Since the viscosity of the media is an unknown, the optical trap was calibrated with the equipartition method. By balancing Stokes' drag with the linear restoring force of the trap, we can find the viscosity of the solution.

Results and Discussion

In order to measure the force generated in the acrosome reaction, we used a solution of methylcellulose and artificial sea water to mechanically slow down its extension rate. Unlike experiments with agarose (Shin, et al, 2007), the acrosome bundle is able to extend to its full length with a finite final velocity. For the acrosome bundle to extend in a viscous medium at a finite velocity, the force generated by the acrosome reaction must at all times exceed the opposing viscous drag, and thus the maximum drag force exerted by the environment yields a lower bound of the acrosome reaction force. For a viscoelastic fluid, the drag force can be found by using the Stokes equation for a cylinder in the limiting case of viscous regime with Deborah number (De) $\ll 1$ (Tirado and Garcadelatorre, 1979). Methylcellulose solutions of 4% (w/v) or lower concentrations exhibit a Newtonian viscous liquid-like behavior with $De \ll 1$, while solutions at 5% or above behaves more like an elastic solid. Here, we obtain a maximum lower bound force using the viscosity from the 4% MC solution. For a strain rate of 0.2 s^{-1} , which is the characteristic strain rate for the extending acrosome bundle in the 4% MC solution, the viscosity of the media was measured with an optical trap to be $\sim 5 \text{ Pa s}$. This yields force values for the acrosome reaction on the order of 260 pN, and provides a lower-bound estimate for the force of the acrosome reaction. Since the acrosome was never stalled in methylcellulose solutions, this value represents a lower bound estimate. In fact, experiments in agarose media have shown that the acrosome stalls at forces about 7 times higher than those measured here (Shin, et al, 2007). Furthermore, force levels on the order of 2 nN have shown to be sufficient to puncture the protective layers of the egg, and, thus, achieve fertilization (Shin, et al, 2007).

Appendix I

Protocols

General Single Molecule Protocols

- Avidin Coated Beads
- Checking PCR Products by Gel Electrophoresis
- Coating Streptavidin Beads with Biotinylated Antibodies
- dsDNA Tethers, general
- Etching Coverslips
- Flow Cells
- PCR

iOFF Protocols

- Combined Single Molecule Fluorescence and Optical Tweezers
- Combined Single Molecule FRET and Optical Tweezers
- Single Molecule Fluorescence

ClpX Protocols

- Carboxymethylation of Cysteine Residues
- Crosslinking Primary Amines to Thiol Groups
- Labeling Cys Residues with Cy3
- Optical Tweezers Assay for ClpX
- Single Molecule Fluorescence Assay for ClpX

Miscellaneous Protocols

- Buffer Recipes
- Methylcellulose Solutions
- PEG Surfaces
- PDMS Channels
- Tubulin Polymerization (Microtubules)

Avidin Coated Beads

(adapted from Polly Fordyce)

This protocol outlines a method for making avidin-coated beads. The procedure consists of covalently coupling biotin molecules to COOH groups on the surface of polystyrene beads. These are then coated with free avidin and last for at least 6 months in the cold room rotator.

Materials

Buffers:

- 100 mM MES buffer, pH 5
- 100 mM phosphate buffer, pH 7.5, 0.1% Tween (PBT)
- 1 M glycine quenching buffer

Reagents:

- 560 nm COOH-functionalized polystyrene beads, 10% solids (Cat # PC03N/3263 (near soap free), Bangs Beads)
- 10 mg/mL biotin-X cadaverine in DMSO (Cat # B-1596, Molecular Probes)
- Sulfo-NHS (Cat # 24510, Pierce)
- EDC (Cat # 22980, Pierce)
- Avidin-DN (Cat # A-3100, Vector Labs)

Procedure

Conjugating beads to biotin and coating with avidin

1. Take the EDC and the Sulfo-NHS jars and place them on the bench top. It is important to let them equilibrate to room temperature before opening them to weigh the dry solids. EDC and Sulfo-NHS are very moisture sensitive.
2. Add iced to cup sonicator and sonicate 200 μ L of beads for 5 min at 30% power.
3. Mix the following in a 15 mL Falcon tube:
 - 200 μ L biotin-X cadaverine
 - 20 mg Sulfo-NHS
 - 1.6 mL 100 mM MES buffer
4. Add the sonicated 200 μ L beads to the mixture and invert several times to mix.
5. Add 50 mg of EDC to mixture and vortex.
6. Incubate on a rotator overnight at room temperature.

7. Add 500 μ L of the glycine quenching buffer and incubate for 15 min on a rotator at room temperature.
8. Separate beads into 5 equal fractions (500 μ L) in 1.5 mL Eppendorf tubes.
9. Spin in bench top centrifuge for at least 4 min at 10k RPM and resuspend in 200 μ L of PBT. Repeat a total of 6 times.
10. After last wash, add 300 μ L of PBT to each tube.
11. Add ice to the cup sonicator and sonicate each tube for 2 min at 40% power.
12. Add 500 μ L of washed beads to 1 mL bottle of Avidin-DN. Mix and transfer into new Eppendorf tubes. Incubate overnight in the rotator in the cold room. Beads can be stored at this step for at least 6 months.

Purifying beads from excess avidin just before use

1. Take appropriate amount of beads, usually 100 μ L, spin in bench top centrifuge for at least 4 min at 10k RPM and resuspend in same amount of PBT (usually 100 μ L). Repeat a total of 6 times and sonicate for 2 min at 40% power. At this point, the beads can be used right away or stored in the fridge for a couple of days. If so, wash the beads at least once before use and then sonicate for 2 min at 40% power.
2. It is usually a good idea to measure the concentration of beads before use. To do so, record the transmission (%T) of the solution at 500 nm. Note that a standard or calibration curve will have to be needed. For comparison, after washing and just before use, we usually get a bead concentration of approximately 50 pM.

Checking PCR Products by Gel Electrophoresis

This protocol presents procedures for making agarose gels, loading DNA samples in them, and comparing the samples against a ladder standard. It is useful to run a gel immediately after PCR to check that everything went as planned. Note that this protocol has been optimized for resolving bands representative of ~1000kb dsDNA. If other dsDNA sizes wish to be resolved, the agarose concentration or running time must be changed. Always use sterile, DNase, and RNase-free pipette tips.

Materials

Buffers:

- 10mM TE buffer, pH 7.5
- 5X TBE buffer (Cat # 955155301, Brinkmann)

Reagents:

- 6X gel loading buffer (Cat # G7654, Simga)
- 1kb dsDNA ladder
 - 200 μ L 6X gel loading buffer
 - 750 μ L TE buffer
 - 50 μ L stock solution (Cat # L-201, Bayou Biolabs)
- Agarose (Cat # EM-2120, VWR)
- SybrGreen 10,000X (Cat # S7563, Molecular Probes)

Procedure

1. In an 250 mL Erlenmeyer flask, dissolve 0.8 g of agarose powder in 80 mL of 1X TBE buffer (1% gel). Swirl, then heat up solution in microwave for at least two minutes. Note that the solution may boil. If this happens, open the microwave door and let cool down for a briefly. Continue with heating until the two minutes have elapsed.
2. Allow agarose solution to cool at room temperature for 4 min. In the meantime, thaw an aliquot of the SYBR Green dye.
3. Add 8 μ L of SYBR Green dye to the agarose solution. Swirl to mix.
4. Prepare gel electrophoresis chamber for gel pouring (want gaskets and walls sealing the gel volume off from rest of apparatus). Place the appropriate combs in the chamber slots.
5. Pour the agarose solution into the chamber and wait ~30 min for it to gel.
6. Rotate the chamber such the combs are proximal to the cathode (black terminal).

7. Fill electrophoresis apparatus with 420 mL 1X TBE buffer. Make sure that there is sufficient liquid to submerge gel.
8. Remove the comb from the gel very carefully and inspect wells for ruptures in their walls.
9. Dilute PCR product to a 1:10 ratio in TE buffer. This will improve the quality of the bands.
10. Add 6 μ L of the 1kb dsDNA ladder to one of the wells, usually the first or last well.
11. To a 96-well plate, add 3 μ L of the 6X gel loading buffer to as many, N, wells as PCR products that will be run in the gel.
12. Mix 18 μ L of the diluted PCR product with the 3 μ L of the 6X gel loading buffer and transfer 18 μ L of the resulting mixture to one of the wells in the gel. Be careful not to rupture any of the walls of the well. Do not introduce any bubbles.
13. Once all the samples have been loaded, replace the apparatus cover and set the power supply to 110V at constant voltage. Press Run.
14. Run the gel for ~1.5-2 hrs if only one comb is present. If two combs are present, run for 45 mins.
15. To view the resulting bands, bring the gel to the Alpha Innotech FluorChemTM 8900 machine, open the door, and place on top of the illuminator. On the computer, click acquire, then open the door of the machine and center the gel on the camera field of view. This is also a good point to adjust the magnification of the image on the camera. Close the door again and select filter position #3 (SYBR Green). Click on UV transillumination and the bands should show up on the computer monitor. Set the capture time to 100 ms (this can be changed as necessary) and click acquire image. Adjust the image levels and click save to store the image.
16. Dispose of the gel in an appropriate container (hazardous material).

Coating Streptavidin Beads with Biotinylated Antibodies

(adapted from Chip Asbury)

This protocol describes a simple method for coating streptavidin beads with biotinylated anti-His antibodies.

Materials

Buffers:

100 mM PBT, pH 7.5

Reagents:

10 mg/mL casein in PBT

Biotinylated anti-His (penta-His) antibody (Cat # 34440, Qiagen)

Streptavidin Beads, 800 nm, 1% w/v (Cat # SVP-08-10, Spherotech)

Procedure

1. Mix the following:
 - 19.5 μ L PBT
 - 20 μ L 10mg/mL casein
 - 0.5 μ L anti-His antibody
 - 10 μ L beads
2. Incubate in ice for 20 min
3. Wash 4 times by centrifuging for 4 min at 10,000 RPM and resuspending in 100 μ L PBT.

dsDNA Tethers, general

(adapted from Polly Fordyce and Keir Neuman)

This protocol describes a general methodology for forming dsDNA tethers in a flow cell. There are many variants of this protocol. In the “inverted” protocol, the tethers are bound to the surface-bound antibody first, and then the beads are flown into the flow cell.

Materials

Buffers:

100 mM PBT, pH 7.5

Reagents:

20 pM 1010 base pair dsDNA (biotin and digoxigenin ends)

200 µg/mL anti-digoxigenin antibody in PBS (Cat # 1333089, Roche Applied Science)

1 mg/mL casein in PBT

Procedure:

1. Wash avidin-coated beads. Resuspend and sonicate in PBT. Mix 100 µL 20 pM dsDNA with 100 µL 50 pM beads and incubate in rotator at 4 °C or ice for at least 20 min.
2. Make flow cell with microscope slide, double-sticky tape, and etched coverslip. Dilute antibody to 20 µg/mL with PBT and flow 20 µL into the flow cell. Incubate for 20 min.
3. Flow 100 µL 1 mg/mL casein and incubate for 20 min.
4. While the casein is incubating, wash bead-dsDNA complexes to remove excess or unbound dsDNA and primers. Sonicate complexes for 2 min at 40% power.
5. Flow 20 µL of bead-dsDNA complexes and incubate for 20 min.
6. Flow 200 µL of PBT.

Etching Coverslips

(adapted from Polly Fordyce)

This protocol outlines a method to etch coverslips using KOH.

Materials

Reagents:

Potassium Hydroxide (KOH)
Ethanol (100%)
ddH₂O (Millipore, Dedon Lab)

Equipment:

Corning Coverslips, 24 x 60 mm, 1½ thickness (Cat # 12-553-6, Fisher Scientific)
Teflon racks (custom made)

Procedure

1. Dissolve 100 g of KOH in 300 mL of 100% ethanol in a 1 L beaker. Stir with a stir bar until KOH is completely dissolved or for 30 min.
2. Place coverslips in Teflon racks. Usually we do 6-10 racks per procedure.
3. Fill another 1 L beaker with at least 300 mL of 100% ethanol and two additional 1 L beakers with at least 300 mL of ddH₂O. Degas all four beakers (two at a time) in the bath sonicator (degas setting) for 5 min. After degassing, place one of the ddH₂O beakers and the KOH beaker in the bath sonicator.
4. Submerge one coverslip rack in the KOH solution and sonicate for 5 min.
5. Wash coverslips by dipping the rack up and down or spinning it in the ethanol beaker.
6. Wash coverslips by dipping the rack up and down or spinning it in the ddH₂O beaker.
7. Submerge the rack of coverslips in the ddH₂O beaker in the sonicator and sonicate for 5 min.
8. Spritz coverslips with ddH₂O bottle. Do each coverslip side at least twice.
9. Spritz coverslips with ethanol bottle. Do each coverslip side at least twice.
10. Repeat steps 4-9 for other racks. Note that the ddH₂O and KOH beakers in the sonicator can contain coverslip racks during sonication at the same time.

11. Dry rack in oven for at least 15 min at 100 °C. Store coverslips in racks inside sealed containers at room temperature. They last about a week.

Flow Cells

This protocol outlines a simple method by which to flow cells from microscope slides, double-stick tape, and etched coverslips.

Materials

Equipment:

Etched Coverslips

Double Stick Tape (Cat # 909955, Office Depot)

Microscope Slides (Cat # 48312-068, VWR)

Procedure

1. Place two strips of double stick tape along the center of the short axis of a microscope slide. The pieces of tape should be about 4 mm apart of each other. To avoid air bubbles, stick the top part of the tape (the part facing up on the roll) on the slide. In other words, flip the piece of tape before sticking it on the slide.
2. Take an etched coverslips and place it along the two strips of double stick tape.
3. Use an eppendorf tube and press on the coverslip to seal the slide-tape-coverslip interface. Be careful to not crack the coverslip.
4. Flow appropriate reagents. In the first flow, capillary action will suck the solution in. The flow cells can hold about 15 μL .
5. To exchange the contents inside the flow cell, load one side of the channel with the appropriate solution and suck with a vacuum manifold on the other side. It usually advantageous to keep the flow rates low by not opening the vacuum all the way and by using a 20 μL pipette tip on the end of the tubing. I usually control the flow rate even more by placing the pipette tip in the same plane of the flow cell, but holding it perpendicular to the channel.

PCR

(adapted from Polly Fordyce)

This protocol describes a simple procedure for making dsDNA segments 1010 base pair long. It employs two primers, named forward and reverse, whose 5' ends can be readily modified with a variety of different motifs. In the example below, the 5' ends of the forward and reverse primers will have a biotin and a digoxigenin motif, respectively.

Materials

Buffers:

10 mM TE buffer, pH 8

Reagents:

Recombinant Taq DNA Polymerase Kit (Cat # 10342-020, Invitrogen)

Taq DNA Polymerase

10X PCR buffer

50 mM MgCl₂

dNTPs (2.5 mM)

6 µL 100 mM dATP (Cat # 10216-018, Invitrogen)

6 µL 100 mM dCTP (Cat # 10217-016, Invitrogen)

6 µL 100 mM dGTP (Cat # 10218-014, Invitrogen)

6 µL 100 mM dTTP (Cat # 10219-012, Invitrogen)

216 µL ddH₂O

M13mp18 plasmid (Cat #, P-105)

5 µg/mL in TE buffer

Oligo primers (Custom Ordered, IDT)

20 µM in TE buffer

forwardprimer

5' – TAT TGC GTT TCC TCG GTT TC – 3'

biotinforwardprimer

[biotin] – 5' – TAT TGC GTT TCC TCG GTT TC – 3'

reverseprimer

5' – TTG AAA TAC CGA CCG TGT GA – 3'

digoxigeninreverseprimer

[digoxigenin] – 5' – TTG AAA TAC CGA CCG TGT GA – 3'

QiaQuick Purification Kit (Cat # 27104, Qiagen)

Procedure

1. Dilute all reagents to the appropriate concentrations as specified above and start pre heating the blocks in the PCR machine (program 99).
2. Mix the following cocktail for as many PCR reactions as needed:

Reagent	Volume [μL]
ddH ₂ O	61
10X buffer	10
dNTPs	10
MgCl ₂	3
M13mp18	10
forward primer	2
reverse primer	2
Taq Polymerase	2
Total	100

When doing many PCR reaction (with the same oligos), it is preferable to make one master mix tube that can aliquoted into each PCR tube (100 μL). Note that I usually mix all the reagents together before adding the polymerase. Also, since the polymerase is dissolved in glycerol, pipetting up and down several times is required to ensure proper mixing.

3. Place the PCR tubes in the PCR machine.
4. Run program 99. If the program has been deleted or altered, reprogram the machine as follows:

Stage	Temperature [$^{\circ}\text{C}$]	Time [min]	# of Cycles
Supermelt	94	3	1
Melt	94	1	30
Anneal	48	1	
Elongate	72	5	
Final Extension	72	10	1

5. Clean up the PCR products with the QiaQuick purification kit. Note that 2 tubes can be pooled together if they contain the same PCR products. However, note that we have had a bad experience with these purification kits because we end up losing a significant fraction of our product and many times just ignore this step.
6. Check the quality of the PCR products by running them in an electrophoresis gel. Store all samples in the -20°C freezer if not in use.

Combined Single Molecule Fluorescence and Optical Tweezers

(adapted from Polly Fordyce and Matthew J. Lang)

This protocol presents a method for making a dsDNA construct with a 15 base pair overhang that can be unzipped with optical tweezers and simultaneously monitored with single molecule fluorescence.

Materials

Buffers:

Tris buffer (20 mM, pH 7.5)
TE buffer (10 mM, pH 8)

Materials:

20 μ M primer 1: [biotin] – 5' – TAT TGC GTT TCC TCG GTT TC – 3'
20 μ M primer 2: [Cy3] – 5' – TTG AAA TAC CGA CCG T*G TGA TAA ATA
AGG CGT TAA A – 3' (* = abasic site)
20 μ M oligo: [digoxigenin] – 5' – CGG TCG GTA TTT CAA – 3'
1.2 μ M (100X) catalase in PBT (Cat # 219261, Calbiochem)
2.5 M (100X) β -D(+) glucose in PBT (Cat # 34635, Calbiochem)
180 μ M (100X) glucose oxidase in PBT (Cat # 345386, Calbiochem)
 β (2)-mercaptoethanol (Cat # EM-6010, VWR)

Procedure

1. Run a PCR reaction using the M13mp18 plasmid and primers 1 and 2 and clean the reaction using the QiaQuick purification kit.
2. Determine concentration of PCR reaction and dilute to 20 nM. Dilute the dig-oligo to 100 nM. Mix 10 μ L of each with 50 μ L of TE buffer and 30 μ L of 1 M NaCl. Anneal by placing the mixture in water bath at 90 °C and letting it equilibrate to room temperature in the dark. At this point, the annealed complex can be frozen. Alternatively, the anneal process can be carried out in a machine by setting the temperature to 95 °C and ramping it down to a speed of 0.1 °C/s until reaching 10 °C.
3. To form tethers, mix 100 μ L 20 pM of the annealed DNA complex with 100 μ L of washed avidin beads and follow the general dsDNA protocol with the following modification:

In the final wash, use 200 μ L of Tris buffer with 1% BME, 0.1 mg/mL BSA (or casein), and 1X glucose, catalase, and glucose oxidase. Degas the solution for 30 min before using.

Combined Single Molecule FRET and Optical Tweezers

(adapted from Mariya Barch)

This protocol presents a method for making a dsDNA construct with a 20 base pair hairpin that can be unzipped with optical tweezers and simultaneously monitored the fluorescent emission of a donor and an acceptor in a strategically placed FRET pair.

Materials

Buffers:

Tris buffer (20 mM, pH 7.5)
TE buffer (10 mM, pH 8)

Materials:

20 μ M primer 1: [biotin] – 5' – CAA ATC ATC TGT TTC ATT GAA
ACC TGA CAT G – 3'
20 μ M primer 2: 5' – GAT CC* ATG GAT GAG ATG GCT ACC ACT CAG
ATT TCC – 3' (* = abasic site)
20 μ M oligo 1: [Cy3] – 5' – CAA CAA TAC ATC ATC TAC CAT CAT C – 3'
20 μ M oligo 2: 5' – GGA TCC AGT ACC ATC TCA TCT CAG CTC CAC –
3' – [Alexa 647]
20 μ M oligo 3: [digoxigenin] – 5' – GAT GAT GGT AGA TGA TGT ATT
GTT GTT TCG CCG CGG GCC GGC GCG CGG TTT TCC GCG CGC
CGG CCC GCG GCG TTT GTG GAG CTG AGA TGA GAT GGT ACT G –
3'
PABX4T fimbrin plasmid (Courtesy of Yelena Freyzon)
T4 DNA ligase (Cat # M0202S, New England Biolabs)
Polynucleotide kinase (Cat # M0201S, New England Biolabs)
1.2 μ M (100X) catalase in PBT (Cat # 219261, Calbiochem)
2.5 M (100X) β -D(+) glucose in PBT (Cat # 34635, Calbiochem)
180 μ M (100X) glucose oxidase in PBT (Cat # 345386, Calbiochem)
 β (2)-mercaptoethanol (Cat # EM-6010, VWR)

Equipment:

QIAquick Gel Extraction Kit (Cat # 28704, Qiagen)

Procedure

4. Run a PCR reaction using the PABX4T fimbrin plasmid and primers 1 and 2. Run a gel and cut out the appropriate band (1007 base pairs). Purify the band with the QIAquick gel extraction kit.
5. Mix 10 μ L of oligos 1, 2, and 3 with 40 μ L of TE buffer and 30 μ L of 1 M NaCl. Anneal the oligos by placing them in a 90 °C water bath and letting it equilibrate to room temperature.

6. Phosphorylate the 5' end of the PCR product with the polynucleotide kinase kit.
7. Once phosphorylated, mix the PCR reaction product with the annealed product and ligate them using T4 ligase.
8. To form tethers, mix 100 μ L 20 pM of the annealed DNA complex (or an appropriate concentration/dilution) with 100 μ L of washed avidin beads and follow the general dsDNA protocol with the following modification:

In the final wash, use 200 μ L of Tris buffer with 1% BME, 0.1 mg/mL BSA (or casein), and 1X glucose, catalase, and glucose oxidase. Degas the solution for 30 min before using.

Single Molecule Fluorescence

(adapted from Ha et al, 2002)

This protocol presents a method for presenting fluorescent dyes on a surface at sufficiently low concentrations for single molecule fluorescence experiments. In particular, DNA oligos can be custom ordered with the appropriate dyes and motifs, making the assay geometry very flexible.

Materials

Buffers:

Tris buffer (20 mM, pH 7.5)

TE buffer (10 mM, pH 8)

Materials:

20 μ M oligo 1: [Cy3] – 5' – CCA CTC TAG G – 3' – [digoxigenin]

20 μ M oligo 2: 5' – CCT AGA GTG G – 3' – [biotin]

200 μ g/mL anti-digoxigenin antibody in PBS (Cat # 1333089, Roche Applied Science)

1.2 μ M (100X) catalase in PBT (Cat # 219261, Calbiochem)

2.5 M (100X) β -D(+) glucose in PBT (Cat # 34635, Calbiochem)

180 μ M (100X) glucose oxidase in PBT (Cat # 345386, Calbiochem)

β (2)-mercaptoethanol (Cat # EM-6010, VWR)

Procedure

1. Mix 100 μ L of oligo 1 with 100 μ L of oligo 2 and anneal by placing the mixture in water bath at 90 °C and letting it equilibrate to room temperature in the dark. At this point, the annealed complex can be frozen.
2. Prepare a flow cell with an etched coverslip and fill it with 20 μ L of 20 μ g/mL of the anti-dig antibody. Incubate for 20 min.
3. Wash with 100 μ L of Tris buffer and flow 40 μ L of 25 pM fluorescent annealed dsDNA complexes. Incubate for 20 min.
4. Wash with 200 μ L of Tris buffer with 1% BME, and 1X glucose, catalase, and glucose oxidase. Degas the solution for 30 min before using.

Carboxymethylation of Cysteine Residues

(adapted from Andreas T. Martin)

This protocol describes a method for carboxymethylating cysteine residues in proteins. In particular, the protocol is applied to carboxymethylate cysteine residues in the I27 domain of titin once it has been conjugated to a 1010bp of dsDNA segment such that dsDNA-SMCC-GFP-I27(V15P)-ssrA. This keeps the I27 domain of the fusion unfolded even after it has been translocated by ClpX.

Materials

Buffers:

3 M Tris, pH 8.4

Reagents:

6 M Guanidine hydrochloride in 3 M Tris (Cat # G4505, Sigma)

1 M Iodoacetic acid in 3 M Tris (Cat # I4386, Sigma)

dsDNA-GFP-I27(V17P)-ssrA fusion

Equipment:

Desalting chromatography column (Cat # Bio-Gel P-6 gel, BioRad)

Procedure

1. Mix 39 μ L of the dsDNA-GFP-I27(V17P)-ssrA fusion with 33 μ L of the Guanidine hydrochloride. Prepare the iodoacetic acid solution and immediately add 8 μ L to the 72 μ L of guanidine and DNA-protein.
2. Incubate reaction for 90 min at room temperature. Cover tube in aluminum foil to protect GFP and iodoacetate.
3. Desalt reaction twice with PBS or PD buffer to remove guanidine and excess iodoacetic acid.

Crosslinking Primary Amines (dsDNA) to Thiol Groups (cys)

This protocol describes a method for crosslinking primary amines to thiol groups. In particular, the protocol is applied to crosslink a primary amine on one of the 5' ends of a 1010bp dsDNA segment to a N-terminal cysteine on a protein, Cys-GFP-I27(V15P)-ssrA.

Materials

Buffers:

100 mM PBS, pH 7.2

Reagents:

Sulfo-SMCC, 2 mg no weight format (Cat # 22622, Pierce)

1010 bp dsDNA with biotin/amine 5' ends

Cys-GFP-I27(V15P)-ssrA (courtesy of Andreas Martin)

Equipment:

Microcon filter column (Cat # YM-100, Millipore)

Desalting chromatography column (Cat # Bio-Gel P-6 gel, BioRad)

Procedure

4. PCR 1010bp dsDNA segment with biotin and primary amine motifs on opposing 5' ends
5. Concentrate 5-10 tubes of PCR product using the Microcon YM-100 columns. Pool tubes together and spin in column at 2500 RPM (500 g) for at least 20 min. Once the total volume has been reduced to satisfaction, invert column and collect at 3500 RPM (1,000 g).
6. Check the concentration of the dsDNA. We want approximately 70 μ L of about 3 μ M dsDNA. The concentration can be determined by measuring the absorbance of the solution at 260 nm in the UV-Vis:

$$[dsDNA] = OD(Abs)_{260} \frac{50 \mu g / mL}{OD(Abs)_{260}} DR \frac{1.6037 pmole}{\mu g}$$

Typically we dilute our dsDNA by a factor of 100 before making the measurement (DR = dilution ratio). Note that for ssDNA, an extinction coefficient of 30 μ g/mL should be used.

7. Equilibrate two desalting columns with PBS and buffer exchange 70 μ L of the concentrated dsDNA. This removes the TE buffer from the PCR reaction and replaces it with PBS.

8. Dissolve 2 mg of the Sulfo-SMCC in 200 μ L of DMSO. Add 2 μ L of the dissolved SMCC to the buffer-exchanged dsDNA. Mix well.
9. Incubate the reaction in ice for 2 hr.
10. Equilibrate four desalting columns with PBS and dilute the Cys-protein to 100 μ L (we have also used 10 μ L and it seems to work OK). Remove the excess SMCC from the dsDNA reaction and the DTT from the protein dilution by running each solution through two desalting columns.
11. Mix the desalted protein and SMCC-dsDNA and incubate in ice for at least 2 hr.

Labeling Cys Residues with Cy3

This protocol presents a simple method for labeling cysteine residues with Cy3 maleimides. In particular, the method labels a N-term cys in Cys-GFP-I27(V15P)-ssrA, making the ClpX substrate easier to track and detect in single molecule fluorescence experiments.

Materials

Buffers:

Labeling buffer (25 mM HEPES, pH 7.2, 50 mM KCl, 1 mM EDTA, 10% Glycerol)

Reagents:

364 μ M Cys-GFP-I27(V15P)-ssrA (courtesy of Andreas Martin)
Cy3-maleimide (Cat # PA23031, GE Healthcare)

Equipment:

Desalting chromatography column (Cat # Bio-Gel P-6 gel, BioRad)

Procedure

1. Dilute Cy3-maleimide monoreactive pack in 50 μ L of DMF, which gives a Cy3 concentration of about 3 mM.
2. Dilute protein to 75 μ L 10 μ M in labeling buffer and buffer exchange twice to remove DTT.
3. Add 2 μ L of the Cy3-maleimide to the buffer-exchanged protein and incubate overnight. Cover tube with aluminum foil paper to avoid photobleaching. Note that optimal pH range for the cysteine-maleimide reaction is 7.0-7.5.
4. Remove excess or unreacted Cy3 by desalting the reaction mixture in three columns.

Optical Tweezers Assay for ClpX

This protocol describes a method for preparing an assay designed to probe the interaction between ClpX and its substrates at the single molecule level. The procedure is based on the inverted dsDNA tether protocol.

Materials

Buffers:

PBT (100 mM, pH 7.5)
PD (25 mM, pH 7.6)

Reagents:

1 mg/mL streptavidin in PBT (Cat # S000-01, Rockland)
10 mg/mL casein in PBT (Cat # C-8654, Sigma)
10 mg/mL casein in PD (Cat # C-8654, Sigma)
10 μ M biotinylated ClpX (courtesy of Andreas Martin)
Biotin-dsDNA-GFP-I27(V15P)-ssrA complexes
Streptavidin Beads, 800 nm, 1% w/v (Cat # SVP-08-10, Spherotech)
10 mg/mL biotin in PD (Cat # B1595, Molecular Probes)
100 mM ATP γ S in PD (Cat # 10102342001, Roche Applied Sciences)
50 μ M ethidium bromide in PD (Cat # E-8751, Sigma)

Procedure

1. Dilute streptavidin to 0.1 mg/mL in PBT and flow 20 μ L into a flow cell made with an etched coverslip. Incubate for 20 min.
2. During the streptavidin incubation, mix the following and place in ice:
 - 19 μ L PD
 - 20 μ L 10mg/mL casein in PD
 - 0.5 μ L 10 μ M bClpX
 - 0.5 μ L 100 mM ATP γ S
 - 10 μ L beads
3. Prepare a 5 mg/mL casein in PBT solution by mixing 100 μ L of PBT with 100 μ L of 10 mg/mL casein in PBT. Flow 100 μ L of 5 mg/mL casein in PBT into the flow cell and incubate for 20 min.
4. Prepare a 1 mM ATP γ S solution by mixing 292 μ L of PD with 8 μ L of 100 mM ATP γ S and 300 μ L of 10 mg/mL casein in PD.
5. Dilute the biotin-dsDNA-GFP-I27(V15P)-ssrA complexes 1:10 (or appropriate dilution) in 5 mg/mL casein in PBT. Flow 20 μ L of the diluted complexes and incubate for 20 min.

6. While the complexes incubate, wash the beads 4 times by centrifuging them at 13,000 RPM and resuspending in 100 μ L of 1 mM ATP γ S/5 mg/mL casein. Add 1 μ L of 10 mg/mL biotin to the washed beads and sonicate for 2 min at 40% power.
7. Flow 20 μ L of the washed beads into the flow cell and incubate for 20 min.
8. Wash with 150 μ L of the following PD-buffer based mix:
 - 5 mg/mL casein
 - .01 mg/mL biotin
 - 1 mM ATP γ S
 - 500 nM ethidium bromide

Single Molecule Fluorescence Assay for ClpX

This protocol describes a method for preparing an assay designed to probe the interaction between ClpX and its substrates at the single molecule level using single molecule fluorescence. The experiments take place in a PDMS chamber to facilitate the quick exchange of buffers prior to measurements taking place. All buffer exchanges, except the last one, take place with a pipetman and a vacuum manifold.

Materials

Buffers:

PBT (100 mM, pH 7.5)
PD (25 mM, pH 7.6)

Reagents:

1 mg/mL streptavidin in PBT (Cat # S000-01, Rockland)
10 mg/mL casein in PBT (Cat # C-8654, Sigma)
10 mg/mL casein in PD (Cat # C-8654, Sigma)
10 μ M biotinylated ClpX (courtesy of Andreas Martin)
Cy3-GFP-I27(V15P)-ssrA
100 mM ATPyS in PD (Cat # 10102342001, Roche Applied Sciences)
100 mM ATP in PD (Cat # 10519979, Roche Applied Sciences)
Creatine Kinase in PD (Cat # 238395, Calbiochem)
Creatine Phosphate in PD (Cat # 2380, Calbiochem)

Equipment:

PDMS Chamber
1 mL Syringe (Cat # BD309602, VWR)
Needle connector, 18GA x 1/2" long (Cat # 75165A675, McMaster-Carr)
Tubing, 0.07" OD, 0.04" ID, 0.015" thickness (Cat # 63018-088, VWR)

Procedure

1. Dilute streptavidin to 0.1 mg/mL in PBT and flow 20 μ L into a flow cell made with an etched coverslip and a PDMS chamber. Incubate for 20 min.
2. Flow 100 μ L of 1 mg/mL casein in PBT into the flow cell and incubate for 20 min.
3. Dilute ClpX to 100 nM with 1 mM ATPyS in PD buffer and flow 20 μ L into the flow chamber. Incubate for 20 min.
4. Dilute the Cy3 labeled GFP-I27(V15P)-ssrA construct 1:10 (or appropriate dilution) in 0.1 mg/mL casein and 1 mM ATPyS in PD. Flow 20 μ L of the substrate mix and incubate for 20 min. Alternatively, ClpX and the substrates can be premixed together in 0.1 mg/mL casein and 1 mM ATPyS in PD for a couple of minutes in ice and then flown into the chamber and incubated for 20 min.

5. During the substrate incubation, start preparing the tubing for the final buffer wash. Cut two pieces of tubing about 5" long per PDMS flow chamber (I usually do about 6 chambers per experiment). Connect one of the tubes to one of the McMaster Carr syringe connectors on a syringe.
6. Prepare the final washing buffer: ATP or ATP γ S. If ATP, include an ATP regeneration system in the mix:
 - 0.1 mg/mL casein
 - 1 mM ATP (or appropriate concentration)
 - 2.5 mM creatine phosphate
 - 0.05 mg/mL creatine kinase
7. Once the substrate incubation has transpired, take the flow chambers, tubing, syringes, and washing buffer to the instrument room.
8. Assemble a raft for the chambers by placing them on two microscope slides perpendicular to the long axis of the chambers. I usually use double stick tape to secure the raft.
9. Connect the tube (with no syringe attached to it) on the exit port of the flow chamber. It is important to do this first to avoid air bubbles from being trapped in the chamber.
10. Using the syringe, suck enough washing buffer to fill the other tube (about 100 μ L). Connect the tube to the entry port of the flow chamber. Before pressing it into the port, I like to dap the port with a drop of the washing buffer to push out any air in it.
11. Place the fully assembled flow chamber on the microscope stage and look for single molecule fluorescence spots using the Andor camera. Once a region of interest is identified, close all shutters immediately and switch the Andor camera to external mode and set it to acquired images every 3 s for 300 ms (or appropriate timing). Start recording a movie of 100 images. As soon as the first image comes on screen, start pushing the washing buffer through the flow chamber. Do this as quick as possible, but do not press too hard such that the flow chamber starts leaking.

Buffer Recipes

This protocol contains recipes for some of the commonly used buffers in the lab.

PBT (100 mM phosphate buffer, pH 7.5)

1860 μL 1 M NaH_2PO_4
8140 μL 1 M Na_2HPO_4
90 mL ddH₂O
100 μL Tween (0.1%)
0.2 μm filter

Labeling Buffer (25 mM, pH 7.2)

25 mM Hepes, pH 7.2
50 mM KCl
1 mM EDTA
10% Glycerol
0.2 μm filter

MES (100 mM, pH 5)

1.952 g MES-hydrate
100 mL ddH₂O
equilibrate pH with KOH
0.2 μm filter

Glycine (1 M)

0.7504 g glycine
1 mL PBT
9 mL ddH₂O
0.2 μm filter

TE

10 mM Tris buffer, pH 8
1 mM EDTA
0.2 μm filter

Tris (20 mM, pH 7.5)

20 mM Tris, pH 7.5
6 mM NaCl
1.7 mM MgCl_2
equilibrate pH with KOH
0.2 μm filter

Sodium Bicarbonate (100 mM, pH 8.3)

8.4 mg sodium bicarbonate
1 mL ddH₂O

PD (protein degradation buffer for ClpX, 25 mM, pH 7.6)

0.59575 g HEPES (25 mM)
0.7455 KCl (100 mM)
0.2033 MgCl₂ (10 mM)
90 mL ddH₂O
10 mL glycerol (10%)
100 µL Tween (0.1%) – optional, although used to tweezers experiments
0.2 µm filter

PBS (100 mM, pH 7.2)

4.3633 g/L monobasic phosphate
18.3263 g/L dibasic phosphate
0.8 g/L NaCl
0.2 µm filter

PEM80 (80 mM PIPES, pH 6.9)

1.2096 g PIPES
19.02 mg EGTA (1 mM)
40.66 mg MgCl₂ (4 mM)
40 mL ddH₂O
equilibrate pH with KOH (solution becomes clear)
add ddH₂O until 50 mL

PEM104 (104 mM PIPES, pH 6.9)

1.5665 g PIPES
24.926 mg EGTA (1.3 mM)
64.0395 mg MgCl₂ (6.3 mM)
40 mL ddH₂O
equilibrate pH with KOH (solution becomes clear)
add ddH₂O until 50 mL

Methylcellulose Solutions

This protocol describes a simple methodology for making a 1% w/v methylcellulose solution. However, the protocol can be readily adapted to make solutions with concentrations up to 4% w/v.

Materials

Reagents:

Methylcellulose, 63,000 MW (Cat # M0387, Sigma)

Procedure

1. In a water bath, warm up 100 mL of ddH₂O in an Erlenmeyer flask to 80 °C under continuous spinning. Place paraffin on the mouth of the flask to prevent the water from evaporating.
2. Add 1 g of methylcellulose powder to the 100 mL of water. Continue spinning for about 5 min, until the mixture forms a turbid homogenous white solution.
3. Kill the heat and let the water bath equilibrate to room temperature under continuous spinning. This takes about 2 hrs.
4. Transfer the flask to a stir plate in the cold room and spin overnight.

PEG Surfaces

(Adapted from Rasnik et al, J Mol Biol, 2004)

PEG is typically regarded as the gold standard in preventing nonspecific binding. This protocol describes a procedure for covalently coating etched coverslips with PEG. The PEG in turn can be functionalized with different moieties on which single molecule assays can be constructed. In particular, PEGylated surfaces resulting from this protocol will contain 1% biotin and are prepared in two steps. The first step coats etched coverslips with aminosilane and the second step attaches the PEG molecules to the primary amines in the silane.

Materials

Buffers:

100 mM Sodium Bicarbonate, pH 7.3

Reagents:

3-Aminopropyltriethoxysilane (Cat # A3684, Sigma)

mPEG-SPA, MW 5,000 (Cat # 2M4M0H01, Nektar)

Biotin-PEG-NHS, MW 3,400 (Cat # 0H4M0F02, Nektar)

Procedure

1. Remove the aminosilane from the fridge and let it equilibrate to room temperature.
2. Fill two 1 L beakers with 500 mL ddH₂O. Fill a third beaker with 500 mL acetone and a fourth beaker with 500 mL 2% aminosilane solution in acetone.
3. Dip etched coverslips in a coverslip rack for 2 min in the beaker solutions in the following order: acetone, aminosilane, ddH₂O, and ddH₂O. The last ddH₂O wash can be done in 100% ethanol if desired.
4. Dry coverslips in for at least 15 min at 100 °C. Store coverslips in racks inside sealed containers at room temperature. They last about a week.
5. Take the silane, mPEG, and biotin-PEG jars and place them on the bench top. It is important to let them equilibrate to room temperature before use because they are very moisture sensitive.
6. Make a flow cell using an aminosilane-coated etched coverslip.
7. Weigh 25 mg of the mPEG and 5 mg of the biotin-PEG (5 mg is the lowest mass reading I trust on our scale).

8. Dissolve the mPEG and the biotin-PEG in 100 μL and 20 μL of sodium bicarbonate (this created 25% w/v solutions), respectively. There might be some bubbles in the solutions, but get rid of these by doing a quick spin.
9. Add 1 μL of the biotin-PEG solution to the mPEG solution, which makes 0.25% biotin-PEG in the 25% mPEG solution.
10. Flow 20 μL of the biotin-PEG-mPEG solution into the flow cell.
11. Incubate for 30 min and wash with 200 μL of an appropriate buffer (PBT).
12. At this point, the construction of a single molecule assay can be started by adding streptavidin or casein to the flow cell.

PDMS Channels

(adapted from Winston Timp and David Quinn)

This protocol describes a procedure for making PDMS chambers that can then be used for single molecule fluorescence experiments. In theory, they can also be used for optical tweezers experiments, but the thickness of the channel needs to be reduced.

Materials

Reagents:

- TTT (Tridecafluoro-1,1,2,2-tetrahydrooctyl-1-triethoxysilane, Cat # T2494, UCT)
- Sylgard PDMS (Cat # 184 SIL ELAST KIT 0.5KG, Ellsworth Adhesives)

Equipment:

- Silicon wafer mold – 3 channels, 1.25 in long, .125 in wide, ~ 100 μm thick (Custom, made by Winston Timp)
- 1.5 mm Biopsy punch (Cat # 21909-134, VWR)

Procedure

1. Place silicon wafer mold on an aluminum foil boat (fold aluminum on itself 4 times, place wafer on it, and bend edges so that no fluids poured on the mold can escape). Make sure that the wafer sits flush on the aluminum so that no fluid can seep underneath.
2. Put 0.5 mL of the TTT on a 1.5 mL eppendorf tube. Place the silicon wafer and the TTT (open tube) in a 80 °C oven at 25 mm Hg pressure for 30 min. Repeat this step every 6 months.
3. Mix 36 mL of the PDMS base with 4 mL of the PDMS curing agent in a 50 mL Falcon tube. Briefly mix in tube with the wood part of cotton swabs (like the once used to clean oil on microscope objectives) and transfer mixture to a coffee cup or plastic glass. Mix well.
4. Place mixture in a vacuum chamber for 30 min at room temperature to remove bubbles.
5. Pour mixture over silicon mold (already on aluminum boat) and incubate for 60 min at 80 °C.
6. Peel PDMS from wafer and place it on a clean aluminum foil sheet. If some of the PDMS seeped below the wafer, it is useful to cut that portion off with a razor blade.
7. Punch holes at each end of the channel (or appropriate locations) with a clean biopsy punch.

8. Cut channels using a razor blade. Make sure to leave at least 3 mm around the channel to ensure that it seals well.
9. Place the cut channels on an etched coverslip. Bake for 30 min at 80 °C to improve the seal. If a better seal is needed, both channel and coverslip should be plasma etched and bonded.

Tubulin Polymerization (Microtubules)

(adapted from Matthew J. Lang)

This protocol describes a method for polymerizing microtubules. The same approach can be followed with fluorescently-labeled tubulin to achieve fluorescent microtubules.

Reagents

Buffers:

- 80 mM PEM80, pH 6.9
- 104 mM PEM104, pH 6.9

Reagents:

- 10 mM Paclitaxel in DMSO (Cat # P3456, Molecular Probes)
- 100 mM GTP in ddH₂O (Cat # G8877, Sigma)
- 65 g/L NaN₃ in ddH₂O (Cat # S8032, Sigma)
- 10 mg/mL Tubulin (Cytoskeleton, #T237)

Procedure

1. Spin tubulin for 30 min at 4 °C. This step is optional.
2. Mix the following to make PEM/GTP
 - 15.4 µL PEM104
 - 2.0 µL 10 mM GTP
3. Mix the following to make TUB
 - 15.2 µL PEM/GTP
 - 2.2 µL DMSO
 - 4.8 µL 10mg/mL tubulin
4. Place mixture in water bath at 37°C for 30 min.
5. Mix the following to make STAB buffer
 - 34.1 µL PEM80
 - 5 µL 10mM GTP
 - 4.7 µL 65 g/L NaN₃
 - 1.2 µL 10 mM Paclitaxel
 - 5 µL DMSO
6. Mix the following
 - 22.2 µL TUB
 - 2 µL STAB

Appendix II

MATLAB Code

Tracking Multiple Single Molecule Fluorescence Spots in Time
Passive Microrheology: Calculating Storage and Loss Moduli
Stokes

Tracking Multiple Single Molecule Fluorescence Spots in Time

```
clear all; close all;
```

```
% This code takes a stack of .tif files that have been extracted from a movie  
% taken with the Andor camera and identifies features (single molecule  
% fluorescence spots) in them. It then correlates the locations of all the spots in % time  
% (across image frames) and determines the time for which each spot was % present at a  
% particular location during the movie. Each one of those time  
% traces represents the longevity of a single fluorescent dye. In the case of  
% ClpX, the substrate was conjugated to Cy3, so the fluorescence longevity of  
% each spot represents the time which ClpX takes to unfold and translocate the %  
% labeled substrate in the presence of ATP. This mfile uses code developed by % David  
% Weitz and coworkers. The source code for bpass.m, cntrd.m, pkfnd.m,  
% and track.m can be found at  
% http://www.seas.harvard.edu/projects/weitzlab/matlab/code.html.
```

```
n=3; %This is the first image after washing with fresh buffer/ATP
```

```
% This finds the spots on the first image so that they can be later compared to the spots  
% throughout the movie. The idea is that %% we want to majority of the spots  
% throughout the movie to correspond to the spots in the original image. This ensures  
% that we did not have many "false" spots detected by the program or many labeled  
% substrates binding to ClpX throughout the movie.
```

```
A=double(imread(['ATP1_000',num2str(n),'.tif'])); % read the first file in the movie  
ns=1; B=bpass(A,ns,7); figure; imagesc(B); colorbar; hold  
pkh=175; pk=pkfnd(B,pkh,5); plot(pk(:,1),pk(:,2),'ro')  
cnt=cntrd(B,pk,7,0); cnt(:,5)=n;  
pos=cnt; clear A B pk cnt
```

```
% This portion of the code finds the spots in all the images of the same movie and  
% stores the locations of all the spots for all images.
```

```
for i=(n+1):99;  
    if i<10;  
        A=double(imread(['ATP1_000',num2str(i),'.tif']));  
        B=bpass(A,ns,5); %imagesc(B);  
        pk=pkfnd(B,pkh,5);  
        cnt=cntrd(B,pk,7,0); cnt(:,5)=i;  
        pos=cat(1,pos,cnt); clear A B pk cnt  
    elseif i>9;  
        A=double(imread(['ATP1_00',num2str(i),'.tif']));  
        B=bpass(A,ns,5); %imagesc(B);  
        pk=pkfnd(B,pkh,5);  
        cnt=cntrd(B,pk,7,0); cnt(:,5)=i;  
        pos=cat(1,pos,cnt); clear A B pk cnt  
    end  
end
```

```
end; clear i pkh
```

```
% This part correlates all spots across time and identifies which spots are the same
% across images.
```

```
param=struct('mem',10,'good',2,'dim',2,'quiet',0);
tr=track(pos,3,param); %clear pos param
```

```
A=double(imread(['ATP1_000',num2str(n),'.tif'])); figure; imagesc(A); colorbar, hold
plot(tr(:,1),tr(:,2),'or'); clear A
```

```
% This portion of the code parses out the information - the longevity - related to each
% individual spot over time. It then groups the spots into three groups: originals - spots
% present in the original image, transient - spots that bound halfway through the movie
% and disappeared before the movie finished, and binder - spots that bound halfway
% through the movie and stayed through the end. Note that there are typically very little
% binders in the movies.
```

```
for i=1:length(tr);
    tr(i,7)=tr(i,5)*3.301-n*3.301;
end; clear i
```

```
figure; hold; smfinfo=ones(1,7); ocnt=0; tcnt=0; bcnt=0;
```

```
for i=1:max(tr(:,6));
    smf=ones(1,7);
    for j=1:length(tr);
        if tr(j,6)==i;
            smf=cat(1,smf,tr(j,:));
        end
    end
    smf(1,:)=smf(1,:)*smf(2,7); smf=cat(1,smf,ones(1,7)*max(smf(:,7)));
    lifetime(i)=smf(size(smf,1),7)-smf(1,7); smfinfo(i,:)=mean(smf,1);
    if smf(1,7)==min(tr(:,7));
        ocnt=ocnt+1; olifetime(ocnt)=smf(size(smf,1),7)-smf(1,7);
    else
        [r,c]=size(smf);
        if smf(r,c)~=max(tr(:,7));
            tcnt=tcnt+1; tlifetime(tcnt)=smf(size(smf,1),7)-smf(1,7);
        else
            bcnt=bcnt+1; blifetime(bcnt)=smf(size(smf,1),7)-smf(1,7);
        end
    end
    plot(smf(:,7),smf(:,3)); clear smf
end; clear i j ocnt tcnt bcnt
```

```
% Plot histograms of the different kinds of spots: original, transient, and binder.
```

```
figure;
subplot(2,2,1); [N,X]=hist(olifetime,20); bar(X,N/length(olifetime),1,'r'); clear N X
```

```
xlabel('Spot Lifetime [sec]'); ylabel('Probability'); title(['ATP1 - Chop - Original - N = ',num2str(length(olifetime))]);
subplot(2,2,2); [N,X]=hist(tlifetime,20); bar(X,N/length(tlifetime),1,'r'); clear N X
xlabel('Spot Lifetime [sec]'); ylabel('Probability'); title(['ATP1 - Chop - Transient - N = ',num2str(length(tlifetime))]);
subplot(2,2,3); [N,X]=hist(blifetime,20); bar(X,N/length(blifetime),1,'r'); clear N X
xlabel('Spot Lifetime [sec]'); ylabel('Probability'); title(['ATP1 - Chop - Binder - N = ',num2str(length(blifetime))]);
subplot(2,2,4); [N,X]=hist(lifetime,20); bar(X,N/length(lifetime),1,'r'); clear N X
xlabel('Spot Lifetime [sec]'); ylabel('Probability'); title(['ATP1 - Chop - All Spots - N = ',num2str(length(lifetime))]);

save ATP1 lifetime smfinfo tr olifetime tlifetime blifetime
```


Passive Microrheology: Calculation of Storage and Loss Moduli

```
clear all; close all;
```

```
% This code can be used to determine the storage and loss modulus of a medium in
% which an optically trapped bead is embedded. The bead is simply held in place with the
% trap and its Brownian motion is recorded over time. Finally, the power spectral density of the
% bead position is calculated and used to determine G' and G". We usually take data
% traces at 150 kHz for about 56 s, which gives a total of 2^23 data points per channel.
```

```
kb=1.38E-23; T=298; %[J/K] %[K]
r=245E-9; h=1E-6; %[m] %[m]
```

```
fs=150375.937; %Acquisition Rate [Hz]
AODtonmx=1148.1; AODtonmy=1041.1; %[nm/MHz]
```

```
% Load Data, Convert V to nm, and PSD. Note that the number of points in the bead
% position trace should be a power of 2 to improve the speed at which the pwelch
% algorithm runs.
```

```
for i=1:10;
```

```
    cal=load(['CalCoeff-',num2str(i),'.txt']);
    calx=cal(:,1); caly=cal(:,2);
```

```
    trace=load(['Trace-',num2str(i),'.txt']);
    Vx=trace(:,1); Vy=trace(:,2);
```

```
    nmx=AODtonmx*(calx(1)+calx(2)*Vx+calx(3)*Vy+calx(4)*Vx.^2+calx(5)*Vy.^2+
        calx(6)*Vx.^3+calx(7)*Vy.^3+calx(8)*Vx.^4+calx(9)*Vy.^4+calx(10)*Vx.^5+calx(11
        )*Vy.^5+calx(12)*Vx.*Vy+calx(13)*Vx.^2.*Vy+calx(14)*Vx.*Vy.^2+
        calx(15)*Vx.^3.*Vy+calx(16)*Vx.^2.*Vy.^2+calx(17)*Vx.*Vy.^3+calx(18)*Vx.^4.*V
        y+calx(19)*Vx.^3.*Vy.^2+calx(20)*Vx.^2.*Vy.^3+calx(21)*Vx.*Vy.^4);
```

```
    nmy=AODtonmy*(caly(1)+caly(2)*Vx+caly(3)*Vy+caly(4)*Vx.^2+caly(5)*Vy.^2+
        caly(6)*Vx.^3+caly(7)*Vy.^3+caly(8)*Vx.^4+caly(9)*Vy.^4+caly(10)*Vx.^5+caly(11
        )*Vy.^5+caly(12)*Vx.*Vy+caly(13)*Vx.^2.*Vy+caly(14)*Vx.*Vy.^2+
        caly(15)*Vx.^3.*Vy+caly(16)*Vx.^2.*Vy.^2+caly(17)*Vx.*Vy.^3+caly(18)*Vx.^4.*V
        y+caly(19)*Vx.^3.*Vy.^2+caly(20)*Vx.^2.*Vy.^3+caly(21)*Vx.*Vy.^4);
```

```
    nm=(nmx-nmy)/sqrt(2);
```

```
    p=log2(length(nm))-1;
```

```
    [PSD(:,i),f(:,i)]=pwelch(nm,2^p,[],[],fs); i %PSDx [nm^2/Hz]
```

```
    clear cal calx caly trace Vx Vy nmx nmy nm p
```

```
end
```

```
% Average 10 power spectral densities to reduce noise in the measurements and
% truncate the first couple of points to remove discontinuities from the signal at low
```

```
% frequencies.
f=mean(f,2); f=f(3:length(f)); %[Hz]
PSD=mean(PSD,2); PSD=PSD(3:length(PSD)); %[nm^2/Hz]
save PSD1 f PSD

% Calculate the real ,ap, and imaginary, app, parts of the transfer function alpha.
fnm=f; clear f
appnm=pi/2/kb/T/10^21*fnm.*PSD; % [nm/pN]
apnm=sqrt(2)*dct(dst(appnm,3*length(fnm)),3*length(fnm))/sqrt(3*length(fnm));
    % [nm/pN]
j=length(fnm); %0
ap=apnm(1:j); clear apnm
app=appnm(1:j); clear appnm
f=fnm(1:j); clear j
a=ap+sqrt(-1)*app;
save Alpha1 f a ap app

% Takes a geometric average of the signals to reduce the size of the file we are
% working with.
[flog,aplog,applog,alog]=geoave(f,ap,app);

% Calculate the storage and loss modulus
G=1/6/pi/r./a/1000; Glog=1/6/pi/r./alog/1000; % [Pa]
Gp=real(G); Gplog=real(Glog);
Gpp=imag(G); Gpplog=imag(Glog);
save G1 f G Gp Gpp flog Gplog Gpplog

% Use the Cox-Mertz rule to calculate the viscosity of the medium
etalog=-1*Gpplog./flog/2/pi;
etacm=abs(sqrt(((Gplog-mean(Gplog(2:5)))./flog/2/pi).^2+(Gpplog./flog/2/pi).^2));
save eta1 flog etalog etacm

figure(1)
loglog(f,PSD,'r')
xlabel('Frequency [Hz]')
ylabel('Power Spectral Density [nm^2/Hz]')
title('1% MC - 490 nm Glass Beads - 400 mW')

figure(2)
loglog(f,ap,'k',f,app,'r')
hold on
plot(flog,aplog,'ko',flog,applog,'ro')
xlabel('Frequency [Hz]')
ylabel('Real Response Function [nm/pN]')
title('1% MC - 490 nm Glass Beads - 400 mW')
legend('a"', 'a"', 'a" Average', 'a" Average', 'Location', 'Best')
```

```

figure(3)
loglog(f,Gp,'k',f,-1*Gpp,'r')
hold on
plot(flog,Gplog,'ko',flog,-1*Gplog,'ro')
xlabel('Frequency [Hz]')
ylabel('Moduli [Pa]')
title('1% MC - 490 nm Glass Beads - 400 mW')
legend('G''', 'G'' Average', 'Location', 'Best')

figure(4)
loglog(flog,etalog,'ks',flog,etacm,'ro')
xlabel('Frequency [Hz]')
ylabel('Viscosity [Pa sec]')
title('1% MC - 490 nm Glass Beads - 400 mW')
legend('G''', 'Cox-Merz', 'Location', 'Best')
clear

%%%%%%%%%%%%%%%%%%%%%%%%%%%%%%%%%%%%%%%%%%%%%%%%%%%%%%%%%%%%%%%%%%%%%%%%%%
%%%%%%%%%%%%%%%%%%%%%%%%%%%%%%%%%%%%%%%%%%%%%%%%%%%%%%%%%%%%%%%%%%%%%%%%%%
function [ylog]=geoave(f,y);
Navg=21;
favg=logspace(log10(f(1)),log10(f(length(f))),Navg);
% Determine bin width and parameters for geometric series
for q=1:length(favg)-1
    bin(q)=favg(q+1)-favg(q);
end
a0=bin(1); % Initial bin width
ratio=bin(2)/bin(1); % ratio for geometric series

% Find the indices for each bin
sum(1)=0;
for j=1:length(bin)
    sum(j+1)=a0*(ratio^(j-1)) + sum(j);
    for m=1:length(f)
        if f(m)<=f(1)+sum(j+1),
            upper=m;
        else
            break
        end
    end
end

```

```
for q=1:length(f)
    if f(q) > f(1) + sum(j)
        break
    else
        lower=q;
    end
end
% flog(j)=mean(f(lower:upper)); % [Hz]
% ylog(j)=mean(y(lower:upper)); % [nm/pN]
end
clear Navg favg q bin a0 ratio sum j m upper q lower
```

Stokes

```
clear all; close all;
```

```
% This program takes a .txt data file resulting from the moving a trapped back and forth
% at constant speed for a fixed distance using the Back and Forth vi. This can be done
% at different trap powers (controlled with waveplate). The resulting bead
% displacements can be used to determine the stiffness of the trap if the viscosity of the
% surrounding medium is known (water). Alternatively, the stiffness of the trap can be
% calculated using the equipartition method and used to determine the viscosity of the
% surrounding medium if this is not known ethylcellulose solutions or glycerol mixtures).
```

```
kb=1.38E-2; T=298; % [pN nm/K] [K]
```

```
h=1E-6; %Bead Height [m]
r=500E-9; %Bead Radius [m]
```

```
f=50000; %Acquisition Rate [Hz]
AODtonmx=1148.1; AODtonmy=1041.1; %[nm/MHz]
```

```
deg=[180 210 240 220]; % Waveplate setting (180 is max power) [ ]
power=[425 100 95 15.5]; % Trapping laser power [mW]
speed=[1000 500 250 100]; %Stage speed [um/sec]
dist=[30 10]; %Sweeping Distance [um]
save Param25 deg power speed dist
```

```
% Load the stiffness calibration files for the different trapping power settings.
```

```
for i=1:length(deg);
    stiffness=load(['VarStiff',num2str(deg(i)),'.deg.txt']);
    QPDYvarstiff(i)=stiffness(length(stiffness));
    clear stiffness
```

```
end
clear i
save QPPYStiffvsPower25 QPDYvarstiff power
```

```
figure(1)
hold
subplot(2,2,1)
plot(power,QPDYvarstiff,'s')
xlabel('Trapping Power [mW]')
ylabel('Trap Stiffness [pN/nm]')
title('Trap Stiffness vs Power for 25% Glycerol')
grid
```

```
% This portion of the code analyzes the data. First, it checks for the existence of the a
% file, as defined by sweeping speed and distance and trapping power
```

% (deg). Then it converts the data from volts to nm and calculates the stiffness of the % trap using the equipartition thermo, to corroborate the section above. Finally, it % analyzes the displacements of the bead as the stage sweeps in the plus (p) and % minus (m) directions. Note that the code already knows when these steps occur in % time and any modifications in the settings of the vi will require an alteration of the % code. In addition, the code accounts for discrepancies between the set stage velocity % and the actual stage velocity, which is 40% slower. Finally, the code uses the bead % displacements to calculate the drag coefficient beta and the viscosity of the % surrounding medium.

```

cnt=0
for i=1:length(deg);
    for j=1:length(speed);
        for k=1:length(dist);
            if exist([num2str(speed(j)), 'umpersec-', num2str(dist(k)), 'um-',
                    num2str(deg(i)), 'deg.txt'])==0;
            else
                cnt=cnt+1
                cal=load(['CalCoeff', num2str(deg(i)), 'deg.txt']);
                calx=cal(:,1);
                caly=cal(:,2);

                VT=load(['VarTrace', num2str(deg(i)), 'deg.txt']);
                VTx=VT(:,1);
                VTavex=mean(VTx);
                VTy=VT(:,2);
                VTavey=mean(VTy);

                trace=load([([num2str(speed(j)), 'umpersec-', num2str(dist(k)), 'um-',
                    num2str(deg(i)), 'deg.txt'])]);
                Vx=trace(:,1);
                Vx=Vx-mean(Vx((length(Vx)-4*f):length(Vx)))+VTavex;
                Vy=trace(:,2);
                Vy=Vy-mean(Vy((length(Vy)-4*f):length(Vy)))+VTavey;;

                nmx=AODtonmx*(calx(1)+calx(2)*Vx+calx(3)*Vy+calx(4)*Vx.^2+calx(5)
                    *Vy.^2+calx(6)*Vx.^3+calx(7)*Vy.^3+calx(8)*Vx.^4+calx(9)*Vy.^4+
                    calx(10)*Vx.^5+calx(11)*Vy.^5+calx(12)*Vx.*Vy+calx(13)*Vx.^2.*Vy+calx(
                    14)*Vx.*Vy.^2+calx(15)*Vx.^3.*Vy+calx(16)*Vx.^2.*Vy.^2+
                    calx(17)*Vx.*Vy.^3+calx(18)*Vx.^4.*Vy+calx(19)*Vx.^3.*Vy.^2+
                    calx(20)*Vx.^2.*Vy.^3+calx(21)*Vx.*Vy.^4);
                nmy=AODtonmy*(caly(1)+caly(2)*Vx+caly(3)*Vy+caly(4)*Vx.^2+caly(5)
                    *Vy.^2+caly(6)*Vx.^3+caly(7)*Vy.^3+caly(8)*Vx.^4+caly(9)*Vy.^4+
                    caly(10)*Vx.^5+caly(11)*Vy.^5+caly(12)*Vx.*Vy+caly(13)*Vx.^2.*Vy+caly(
                    14)*Vx.*Vy.^2+caly(15)*Vx.^3.*Vy+caly(16)*Vx.^2.*Vy.^2+

```

```

    caly(17)*Vx.*Vy.^3+caly(18)*Vx.^4.*Vy+caly(19)*Vx.^3.*Vy.^2+
    caly(20)*Vx.^2.*Vy.^3+caly(21)*Vx.*Vy.^4);
nm=(nmx-nmy)/sqrt(2);
nm=nm-mean(nm((length(nm)-4*f):length(nm)));
time=[0:1/f:1/f*(length(nm)-1)];

varstiff1(cnt,1)=power(i);
varstiff1(cnt,2)=kb*T./mean((nm((length(nm)-4*f):length(nm))).^2);

varstiff2(cnt,1)=power(i);
for h=0:7;
    var(h+1)=mean((nm((length(nm)-4*f+h/2*f):(length(nm)-
        3.5*f+h/2*f))).^2);
end
varstiff2(cnt,2)=mean(kb*T./var);
varstiff2(cnt,3)=std(kb*T./var);

figure
plot(time,nm)
xlabel('Time [sec]'); ylabel('Bead Position [nm]');
title([num2str(speed(j)), 'umpersec-', num2str(dist(k)), 'um-',
    ', num2str(power(i)), 'mW'])
grid

for m=1:4;
    msteps(m)=mean(nm(f*(m^2+1.0275+m*.005):f*(m^2+1.0275+m*
        .005+ dist(k)/speed(j)/.4/2)))-mean([mean(nm(f*(m^2+1-.1):f*
        (m^2+1))),mean(nm(f*(m^2+1+.4):f*(m^2+1+.5)))]);
    psteps(m)=mean(nm(f*(m^2+2.03+m*.005):f*(m^2+2.03+m*
        .005+dist(k)/speed(j)/.4/2)))-mean([mean(nm(f*(m^2+2.1):
        f*(m^2+2))),mean(nm(f*(m^2+2+.4):f*(m^2+2+.5)))]);
end
mstepave(j,i)=mean(msteps);
mstepstd(j,i)=std(msteps);
pstepave(j,i)=mean(psteps);
pstepstd(j,i)=std(psteps);

beta=6*pi*r*speed(j)*.4E-6/(1-9/16*r/h+1/8*(r/h)^3-45/256*(r/h)^4-
    1/16*(r/h)^5);
eta(cnt,1)=speed(j)*.4E-6;
eta(cnt,2)=abs(mstepave(j,i))*varstiff2(cnt,2)*1E-12/beta;
eta(cnt,3)=mstepstd(j,i)*varstiff2(cnt,2)*1E-12/beta;
eta(cnt,4)=-1*speed(j)*.4E-6;
eta(cnt,5)=abs(pstepave(j,i))*varstiff2(cnt,2)*1E-12/beta;
eta(cnt,6)=pstepstd(j,i)*varstiff2(cnt,2)*1E-12/beta;

```

```
clear cal calx caly VT VTx VTavex VTy VTavey trace Vx Vy nmx nmy
nm time var m msteps psteps beta
end
end
end
end
clear kb T h r f AODtonmx AODtonmy i j k cnt
save steps25 pstepave pstepstd mstepave mstepstd
save eta25 eta
save varstiff25 varstiff1 varstiff2

figure
hold
errorbar(eta(:,1),eta(:,2),eta(:,3),eta(:,3),'sk')
errorbar(eta(:,4),eta(:,5),eta(:,6),eta(:,6),'sr')
xlabel('Stage Speed [m/sec]')
ylabel('Viscosity [Pa sec]')
title('25% Glycerol')
grid

figure(1)
subplot(2,2,3)
plot(varstiff1(:,1),varstiff1(:,2),'sk')
xlabel('Trapping Power [mW]')
ylabel('Trap Stiffness [pN/nm]')
grid

figure(1)
subplot(2,2,4)
errorbar(varstiff2(:,1),varstiff2(:,2),varstiff2(:,3),varstiff2(:,3),'sk')
xlabel('Trapping Power [mW]')
ylabel('Trap Stiffness [pN/nm]')
grid
```

References

- Abbondanzieri EA, Greenleaf WJ, Shaevitz JW, Landick R, and Block SM. 2005a. Direct observation of base-pair stepping by RNA polymerase. *Nature* 438:460-465.
- Abbondanzieri EA, Shaevitz JW, and Block SM. 2005b. Picocalorimetry of transcription by RNA polymerase. *Biophysical Journal* 89:L61-L63.
- Addas KM, Schmidt CF, and Tang JX. 2004. Microrheology of solutions of semiflexible biopolymer filaments using laser tweezers interferometry. *Physical Review E* 70:-
- Alberts B. 1998. The cell as a collection of protein machines: preparing the next generation of molecular biologists. *Cell* 92:291-294.
- Alberts B. 2002. *Molecular biology of the cell*. Garland Science, New York. xxxiv, 1463, [1486] p.
- Asbury CL, Fehr AN, and Block SM. 2003. Kinesin moves by an asymmetric hand-over-hand mechanism. *Science* 302:2130-2134.
- Ashkin A. 1970. Acceleration and Trapping of Particles by Radiation Pressure. *Physical Review Letters* 24:156-159.
- Ashkin A. 1992. Forces of a Single-Beam Gradient Laser Trap on a Dielectric Sphere in the Ray Optics Regime. *Biophysical Journal* 61:569-582.
- Ashkin A, and Dziedzic JM. 1971. Optical Levitation by Radiation Pressure. *Applied Physics Letters* 19:283-285.
- Ashkin A, and Dziedzic JM. 1987. Optical Trapping and Manipulation of Viruses and Bacteria. *Science* 235:1517-1520.
- Ashkin A, Dziedzic JM, and Yamane T. 1987. Optical Trapping and Manipulation of Single Cells Using Infrared-Laser Beams. *Nature* 330:769-771.

- Atakhorrami M, and Schmidt CF. 2006. High-bandwidth one- and two-particle microrheology in solutions of wormlike micelles. *Rheologica Acta* 45:449-456.
- Barbas CF. 2001. Phage display : a laboratory manual. Cold Spring Harbor Laboratory Press, Cold Spring Harbor, NY. 1 v. in various pagings.
- Bell GI. 1978. Models for Specific Adhesion of Cells to Cells. *Science* 200:618-627.
- Berg HC, and Turner L. 1979. Movement of Microorganisms in Viscous Environments. *Nature* 278:349-351.
- Berg-Sorensen K, and Flyvbjerg H. 2004. Power spectrum analysis for optical tweezers. *Review of Scientific Instruments* 75:594-612.
- Bernath PF. 2005. Spectra of atoms and molecules. Oxford University Press, Oxford ; New York. xiv, 439 p.
- Bishop AI, Nieminen TA, Heckenberg NR, and Rubinsztein-Dunlop H. 2004. Optical microrheology using rotating laser-trapped particles. *Physical Review Letters* 92:-
- Blainey PC, van Oijent AM, Banerjee A, Verdine GL, and Xie XS. 2006. A base-excision DNA-repair protein finds intrahelical lesion bases by fast sliding in contact with DNA. *Proceedings of the National Academy of Sciences of the United States of America* 103:5752-5757.
- Blanchard SC, Kim HD, Gonzalez RL, Puglisi JD, and Chu S. 2004. tRNA dynamics on the ribosome during translation. *Proceedings of the National Academy of Sciences of the United States of America* 101:12893-12898.
- Block SM. 2007. Kinesin motor mechanics: Binding, stepping, tracking, gating, and limping. *Biophysical Journal* 92:2986-2995.
- Block SM, Asbury CL, Shaevitz JW, and Lang MJ. 2003. Probing the kinesin reaction cycle with a 2D optical force clamp. *Proc Natl Acad Sci U S A* 100:2351-2356.
- Brau RR, Tarsa PB, Ferrer JM, Lee P, and Lang MJ. 2006. Interlaced optical force-fluorescence measurements for single molecule biophysics. *Biophysical Journal* 91:1069-1077.
- Brau RR, Ferrer MJ, Lee H, Castro CE, Tam BK, Tarsa PB, Matsudaira P, Moyce MC, Kamm, RD and Lang MJ. 2007. Passive and active microrheology with optical tweezers. *Journal of Optics A: Pure and Applied Optics* 9: S103-S112.

- Brown GG, and Humphreys WJ. 1971. Sperm-egg interactions of *Limulus polyphemus* with scanning electron microscopy. *Journal of Cell Biology* 51:904-907.
- Burghardt TP, and Axelrod D. 1981. Total Internal Reflection-Fluorescence Photobleaching Recovery Study of Serum-Albumin Adsorption Dynamics. *Biophysical Journal* 33:455-467.
- Burton RE, Baker TA, and Sauer RT. 2003. Energy-dependent degradation: Linkage between ClpX-catalyzed nucleotide hydrolysis and protein-substrate processing. *Protein Sci* 12:893-902.
- Burton RE, Siddiqui SM, Kim YI, Baker TA, and Sauer RT. 2001. Effects of protein stability and structure on substrate processing by the ClpXP unfolding and degradation machine. *Embo J* 20:3092-3100.
- Bustamante C, Bryant Z, and Smith SB. 2003. Ten years of tension: single-molecule DNA mechanics. *Nature* 421:423-427.
- Cecconi C, Shank EA, Bustamante C, and Marqusee S. 2005. Direct observation of the three-state folding of a single protein molecule. *Science* 309:2057-2060.
- Chae BS, and Furst EM. 2005. Probe surface chemistry dependence and local polymer network structure in F-actin microrheology. *Langmuir* 21:3084-3089.
- Chen Y, Hu DH, Vorpapel ER, and Lu HP. 2003. Probing single-molecule T4 lysozyme conformational dynamics by intramolecular fluorescence energy transfer. *Journal of Physical Chemistry B* 107:7947-7956.
- Cheng Z, and Mason TG. 2003. Rotational diffusion microrheology. *Physical Review Letters* 90:-.
- Chigaev A, Buranda T, Dwyer DC, Prossnitz ER, and Sklar LA. 2003. FRET detection of cellular alpha 4-integrin conformational activation. *Biophysical Journal* 85:3951-3962.
- Claudet C, and Bednar J. 2005. Magneto-optical tweezers built around an inverted microscope. *Applied Optics* 44:3454-3457.
- Cornish PV, and Ha T. 2007. A survey of single-molecule techniques in chemical biology. *Acs Chemical Biology* 2:53-61.
- Cramer LP, Briggs LJ, and Dawe HR. 2002. Use of fluorescently labelled deoxyribonuclease I to spatially measure G-actin levels in migrating and non-migrating cells. *Cell Motility and the Cytoskeleton* 51:27-38.

- Curtis JE, Koss BA, and Grier DG. 2002. Dynamic holographic optical tweezers. *Optics Communications* 207:169-175.
- Derosier D, Tilney L, and Flicker P. 1980. Change in the Twist of the Actin-Containing-Filaments Occurs During the Extension of the Acrosomal Process in *Limulus* Sperm. *Journal of Molecular Biology* 137:375-389.
- Desbrieres J, Hirrien M, and Ross-Murphy SB. 2000. Thermogelation of methylcellulose: rheological considerations. *Polymer* 41:2451-2461.
- Dietz H, and Rief M. 2004. Exploring the energy landscape of GFP by single-molecule mechanical experiments. *Proceedings of the National Academy of Sciences of the United States of America* 101:16192-16197.
- Doi M, and Edwards SF. 1986. *The theory of polymer dynamics*. Clarendon Press ; Oxford University Press, Oxford [Oxfordshire] New York. xiii, 391.
- Dougan DA, Mogk A, Zeth K, Turgay K, and Bukau B. 2002. AAA+ proteins and substrate recognition, it all depends on their partner in crime. *FEBS Lett* 529:6-10.
- Dumont S, Cheng W, Serebrov V, Beran RK, Tinoco I, Pyle AM, and Bustamante C. 2006. RNA translocation and unwinding mechanism of HCVNS3 helicase and its coordination by ATP. *Nature* 439:105-108.
- Elf J, Li GW, and Xie XS. 2007. Probing transcription factor dynamics at the single-molecule level in a living cell. *Science* 316:1191-1194.
- Evans E, and Ritchie K. 1997. Dynamic strength of molecular adhesion bonds. *Biophysical Journal* 72:1541-1555.
- Farrell CM, Baker TA, and Sauer RT. 2007. Altered specificity of a AAA plus protease. *Molecular Cell* 25:161-166.
- Feng HP, and Gierasch LM. 1998. Molecular chaperones: clamps for the Clps? *Curr Biol* 8:R464-467.
- Flynn JM, Neher SB, Kim YI, Sauer RT, and Baker TA. 2003. Proteomic discovery of cellular substrates of the ClpXP protease reveals five classes of ClpX-recognition signals. *Mol Cell* 11:671-683.
- Fowler SB, Best RB, Toca Herrera JL, Rutherford TJ, Steward A, Paci E, Karplus M, and Clarke J. 2002. Mechanical unfolding of a titin Ig domain: structure of unfolding intermediate revealed by combining AFM, molecular dynamics simulations, NMR and protein engineering. *J Mol Biol* 322:841-849.

- Freyman TM, Yannas IV, Yokoo R, and Gibson LJ. 2001. Fibroblast contraction of a collagen-GAG matrix. *Biomaterials* 22:2883-2891.
- Funatsu T, Harada Y, Tokunaga M, Saito K, and Yanagida T. 1995. Imaging of Single Fluorescent Molecules and Individual Atp Turnovers by Single Myosin Molecules in Aqueous-Solution. *Nature* 374:555-559.
- Furst EM. 2005. Applications of laser tweezers in complex fluid rheology. *Current Opinion in Colloid & Interface Science* 10:79-86.
- Furst EM, and Gast AP. 1999. Micromechanics of dipolar chains using optical tweezers. *Physical Review Letters* 82:4130-4133.
- Galbraith CG, Yamada KM, and Sheetz MP. 2002. The relationship between force and focal complex development. *Journal of Cell Biology* 159:695-705.
- Gilad R, Porat A, and Trachtenberg S. 2003. Motility modes of *Spiroplasma melliferum* BC3: a helical, wall-less bacterium driven by a linear motor. *Molecular Microbiology* 47:657-669.
- Gittes F, and Schmidt CF. 1998. Back-focal-plane detection of force and motion in optical traps. *Biophysical Journal* 74:A183-A183.
- Gittes F, Schnurr B, Olmsted PD, MacKintosh FC, and Schmidt CF. 1997. Microscopic viscoelasticity: Shear moduli of soft materials determined from thermal fluctuations. *Physical Review Letters* 79:3286-3289.
- Gordon MP, Ha T, and Selvin PR. 2004. Single-molecule high-resolution imaging with photobleaching. *Proceedings of the National Academy of Sciences of the United States of America* 101:6462-6465.
- Gottesman S. 1996. Proteases and their targets in *Escherichia coli*. *Annu Rev Genet* 30:465-506.
- Gottesman S. 2003. Proteolysis in bacterial regulatory circuits. *Annual Review of Cell and Developmental Biology* 19:565-587.
- Gottesman S, Clark WP, de Crecy-Lagard V, and Maurizi MR. 1993. ClpX, an alternative subunit for the ATP-dependent Clp protease of *Escherichia coli*. Sequence and in vivo activities. *J Biol Chem* 268:22618-22626.
- Gottesman S, Maurizi MR, and Wickner S. 1997. Regulatory subunits of energy-dependent proteases. *Cell* 91:435-438.

- Gottesman S, Roche E, Zhou Y, and Sauer RT. 1998. The ClpXP and ClpAP proteases degrade proteins with carboxy-terminal peptide tails added by the SsrA-tagging system. *Genes Dev* 12:1338-1347.
- Greenleaf WJ, Woodside MT, Abbondanzieri EA, and Block SM. 2005. Passive all-optical force clamp for high-resolution laser trapping. *Physical Review Letters* 95:-.
- Grier DG. 2003. A revolution in optical manipulation. *Nature* 424:810-816.
- Guo B, and Guilford WH. 2006. Mechanics of actomyosin bonds in different nucleotide states are tuned to muscle contraction. *Proceedings of the National Academy of Sciences of the United States of America* 103:9844-9849.
- Ha T. 2001. Single-molecule fluorescence methods for the study of nucleic acids. *Curr Opin Struct Biol* 11:287-292.
- Ha T, Enderle T, Ogletree DF, Chemla DS, Selvin PR, and Weiss S. 1996. Probing the interaction between two single molecules: Fluorescence resonance energy transfer between a single donor and a single acceptor. *Proceedings of the National Academy of Sciences of the United States of America* 93:6264-6268.
- Ha T, Rasnik I, Cheng W, Babcock HP, Gauss GH, Lohman TM, and Chu S. 2002. Initiation and re-initiation of DNA unwinding by the Escherichia coli Rep helicase. *Nature* 419:638-641.
- Haga H, Sasaki S, Kawabata K, Ito E, Ushiki T, and Sambongi T. 2000. Elasticity mapping of living fibroblasts by AFM and immunofluorescence observation of the cytoskeleton. *Ultramicroscopy* 82:253-258.
- Harada Y, Funatsu T, Murakami K, Nonoyama Y, Ishihama A, and Yanagida T. 1999. Single-molecule imaging of RNA polymerase-DNA interactions in real time. *Biophysical Journal* 76:709-715.
- Hecht E. 2002. *Optics*. Addison-Wesley, Reading, Mass. vi, 698 p.
- Heidemann SR, and Wirtz D. 2004. Towards a regional approach to cell mechanics. *Trends in Cell Biology* 14:160-166.
- Hersch GL, Burton RE, Bolon DN, Baker TA, and Sauer RT. 2005. Asymmetric interactions of ATP with the AAA+ ClpX(6) unfoldase: Allosteric control of a protein machine. *Cell* 121:1017-1027.
- Hidrovo CH, Brau RR, and Hart DP. 2004. Excitation nonlinearities in emission reabsorption laser-induced fluorescence techniques. *Applied Optics* 43:894-913.

- Hohng S, and Ha T. 2004. Near-complete suppression of quantum dot blinking in ambient conditions. *Journal of the American Chemical Society* 126:1324-1325.
- Hoogenboom JP, van Dijk EMHP, Hernando J, van Hulst NF, and Garcia-Parajo MF. 2005. Power-law-distributed dark states are the main pathway for photobleaching of single organic molecules. *Physical Review Letters* 95:-.
- Huang H, Dong CY, Kwon HS, Sutin JD, Kamm RD, and So PTC. 2002. Three-dimensional cellular deformation analysis with a two-photon magnetic manipulator workstation. *Biophysical Journal* 82:2211-2223.
- Hummer G, and Szabo A. 2001. Free energy reconstruction from nonequilibrium single-molecule pulling experiments. *Proceedings of the National Academy of Sciences of the United States of America* 98:3658-3661.
- Hummer G, and Szabo A. 2003. Kinetics from nonequilibrium single-molecule pulling experiments. *Biophysical Journal* 85:5-15.
- Ishijima A, Kojima H, Funatsu T, Tokunaga M, Higuchi H, Tanaka H, and Yanagida T. 1998. Simultaneous observation of individual ATPase and mechanical events by a single myosin molecule during interaction with actin. *Cell* 92:161-171.
- Ishijima A, and Yanagida T. 2001. Single molecule nanobioscience. *Trends in Biochemical Sciences* 26:438-444.
- Jackson JD. 1999. *Classical electrodynamics*. Wiley, New York. xxi, 808 p.
- Jiang XY, Bruzewicz DA, Wong AP, Piel M, and Whitesides GM. 2005. Directing cell migration with asymmetric micropatterns. *Proceedings of the National Academy of Sciences of the United States of America* 102:975-978.
- Joo C, McKinney SA, Nakamura M, Rasnik I, Myong S, and Ha T. 2006. Real-time observation of RecA filament dynamics with single monomer resolution. *Cell* 126:515-527.
- Joshi SA, Hersch GL, Baker TA, and Sauer RT. 2004. Communication between ClpX and ClpP during substrate processing and degradation. *Nature Structural & Molecular Biology* 11:404-411.
- Kapanidis AN, Laurence TA, Lee NK, Margeat E, Kong XX, and Weiss S. 2005. Alternating-laser excitation of single molecules. *Accounts of Chemical Research* 38:523-533.
- Kapanidis AN, Lee NK, Laurence TA, Doose S, Margeat E, and Weiss S. 2004. Fluorescence-aided molecule sorting: analysis of structure and interactions by

- alternating-laser excitation of single molecules. *Proc Natl Acad Sci U S A* 101:8936-8941.
- Kapanidis AN, and Weiss S. 2002. Fluorescent probes and bioconjugation chemistries for single-molecule fluorescence analysis of biomolecules. *Journal of Chemical Physics* 117:10953-10964.
- Keiler KC, Waller PR, and Sauer RT. 1996. Role of a peptide tagging system in degradation of proteins synthesized from damaged messenger RNA. *Science* 271:990-993.
- Kellermayer MSZ, Smith SB, Granzier HL, and Bustamante C. 1997. Folding-unfolding transitions in single titin molecules characterized with laser tweezers. *Science* 276:1112-1116.
- Kenniston JA, Baker TA, Fernandez JM, and Sauer RT. 2003. Linkage between ATP consumption and mechanical unfolding during the protein processing reactions of an AAA+ degradation machine. *Cell* 114:511-520.
- Kenniston JA, Burton RE, Siddiqui SM, Baker TA, and Sauer RT. 2004. Effects of local protein stability and the geometric position of the substrate degradation tag on the efficiency of ClpXP denaturation and degradation. *J Struct Biol* 146:130-140.
- Khalil AS, Ferrer JM, Brau RR, Kottmann ST, Noren CJ, Lang MJ, and Belcher AM. 2007. Single M13 bacteriophage tethering and stretching. *Proceedings of the National Academy of Sciences of the United States of America* 104:4892-4897.
- Kim DY, and Kim KK. 2003. Crystal structure of ClpX molecular chaperone from *Helicobacter pylori*. *J Biol Chem* 278:50664-50670.
- Kim M, Carman CV, and Springer TA. 2003. Bidirectional transmembrane signaling by cytoplasmic domain separation in integrins. *Science* 301:1720-1725.
- Kim YI, Burton RE, Burton BM, Sauer RT, and Baker TA. 2000. Dynamics of substrate denaturation and translocation by the ClpXP degradation machine. *Mol Cell* 5:639-648.
- Kim YI, Levchenko I, Fraczkowska K, Woodruff RV, Sauer RT, and Baker TA. 2001. Molecular determinants of complex formation between Clp/Hsp100 ATPases and the ClpP peptidase. *Nat Struct Biol* 8:230-233.
- Kobayashi K, Huang CI, and Lodge TP. 1999. Thermoreversible gelation of aqueous methylcellulose solutions. *Macromolecules* 32:7070-7077.
- Koch SJ, and Wang MD. 2003. Dynamic force spectroscopy of protein-DNA interactions by unzipping DNA. *Physical Review Letters* 91:-.

- Kole TP, Tseng Y, Jiang I, Katz JL, and Wirtz D. 2005. Intracellular mechanics of migrating fibroblasts. *Molecular Biology of the Cell* 16:328-338.
- Kotar J, Vilfan M, Osterman N, Babic D, Copic M, and Poberaj I. 2006. Interparticle potential and drag coefficient in nematic colloids. *Physical Review Letters* 96:-.
- Lakadamyali M, Rust MJ, Babcock HP, and Zhuang XW. 2003. Visualizing infection of individual influenza viruses. *Proceedings of the National Academy of Sciences of the United States of America* 100:9280-9285.
- Lakowicz JR. 2006. *Principles of fluorescence spectroscopy*. Springer, New York. xxvi, 954 p.
- Lammerding J, Kazarov AR, Huang H, Lee RT, and Hemler ME. 2003. Tetraspanin CD151 regulates alpha 6 beta 1 integrin adhesion strengthening. *Proceedings of the National Academy of Sciences of the United States of America* 100:7616-7621.
- Landau LD, Lifshitz EM, and Pitaevskii LP. 1980. *Statistical physics*. Landau LD, editor. Pergamon Press, Oxford ; New York. 2 v.
- Lang MJ, Asbury CL, Shaevitz JW, and Block SM. 2002. An automated two-dimensional optical force clamp for single molecule studies. *Biophys J* 83:491-501.
- Lang MJ, Fordyce PM, and Block SM. 2003. Combined optical trapping and single-molecule fluorescence. *J Biol* 2:6.
- Lang MJ, Fordyce PM, Engh AE, Neuman KC, and Block SM. 2004. Simultaneous, coincident optical trapping and single-molecule fluorescence. *Nature Methods* 1:133-139.
- Langer T. 2000. AAA proteases: cellular machines for degrading membrane proteins. *Trends in Biochemical Sciences* 25:247-251.
- Larkin JM, Donaldson WR, Knox RS, and Foster TH. 2002. Reverse intersystem crossing in rose bengal. II. Fluence dependence of fluorescence following 532 nm laser excitation. *Photochemistry and Photobiology* 75:221-228.
- Larson RG. 1999. *The structure and rheology of complex fluids*. Oxford University Press, New York. xxi, 663.
- Lau AWC, Lin KH, and Yodh AG. 2002. Entropic interactions in suspensions of semiflexible rods: Short-range effects of flexibility. *Physical Review E* 66:-.

- Lauffenburger DA, and Horwitz AF. 1996. Cell migration: A physically integrated molecular process. *Cell* 84:359-369.
- Lee SH, Ladavac K, Polin M, and Grier DG. 2005. Observation of flux reversal in a symmetric optical thermal ratchet. *Physical Review Letters* 94:-.
- Li L, Shan H, Yue CY, Lam YC, Tam KC, and Hu X. 2002. Thermally induced association and dissociation of methylcellulose in aqueous solutions. *Langmuir* 18:7291-7298.
- Liphardt J, Onoa B, Smith SB, Tinoco I, and Bustamante C. 2001. Reversible unfolding of single RNA molecules by mechanical force. *Science* 292:733-737.
- Litvinov RI, Bennett JS, Weisel JW, and Shuman H. 2005. Multi-step fibrinogen binding to the integrin alpha IIb beta 3 detected using force spectroscopy. *Biophysical Journal* 89:2824-2834.
- Maier B, Potter L, So M, Seifert HS, and Sheetz MP. 2002. Single pilus motor forces exceed 100 pN. *Proceedings of the National Academy of Sciences of the United States of America* 99:16012-16017.
- Manero O, Bautista F, Soltero JFA, and Puig JE. 2002. Dynamics of worm-like micelles: the Cox-Merz rule. *Journal of Non-Newtonian Fluid Mechanics* 106:1-15.
- Mao CB, Flynn CE, Hayhurst A, Sweeney R, Qi JF, Georgiou G, Iverson B, and Belcher AM. 2003. Viral assembly of oriented quantum dot nanowires. *Proceedings of the National Academy of Sciences of the United States of America* 100:6946-6951.
- Mao CB, Solis DJ, Reiss BD, Kottmann ST, Sweeney RY, Hayhurst A, Georgiou G, Iverson B, and Belcher AM. 2004. Virus-based toolkit for the directed synthesis of magnetic and semiconducting nanowires. *Science* 303:213-217.
- Martin A, Baker TA, and Sauer RT. 2005. Rebuilt AAA plus motors reveal operating principles for ATP-fuelled machines. *Nature* 437:1115-1120.
- Martin A, Baker TA, and Sauer RT. 2007. Distinct Static and Dynamic Interactions Control ATPase-Peptidase Communication in a AAA+ Protease. *Molecular Cell* 27:41-52.
- Mason TG. 2000. Estimating the viscoelastic moduli of complex fluids using the generalized Stokes-Einstein equation. *Rheologica Acta* 39:371-378.
- Mason TG, Ganesan K, vanZanten JH, Wirtz D, and Kuo SC. 1997. Particle tracking microrheology of complex fluids. *Physical Review Letters* 79:3282-3285.

- McGrath JL, Eungdamrong NJ, Fisher CI, Peng F, Mahadevan L, Mitchison TJ, and Kuo SC. 2003. The force-velocity relationship for the actin-based motility of *Listeria monocytogenes*. *Current Biology* 13:329-332.
- Mehta AD, Rief M, Spudich JA, Smith DA, and Simmons RM. 1999. Single-molecule biomechanics with optical methods. *Science* 283:1689-1695.
- Mills JP, Qie L, Dao M, Lim CT, and Suresh S. 2004. Nonlinear Elastic and Viscoelastic Deformation of the Human Red Blood Cell with Optical Tweezers. *Mechanics and Chemistry of Biosystems* 1:169-180.
- Mitchison TJ, and Cramer LP. 1996. Actin-based cell motility and cell locomotion. *Cell* 84:371-379.
- Miyata H, Yasuda R, and Kinosita K. 1996. Strength and lifetime of the bond between actin and skeletal muscle alpha-actinin studied with an optical trapping technique. *Biochimica Et Biophysica Acta-General Subjects* 1290:83-88.
- Nam KT, Kim DW, Yoo PJ, Chiang CY, Meethong N, Hammond PT, Chiang YM, and Belcher AM. 2006. Virus-enabled synthesis and assembly of nanowires for lithium ion battery electrodes. *Science* 312:885-888.
- Neuert G, Albrecht C, Pamir E, and Gaub HE. 2006. Dynamic force spectroscopy of the digoxigenin-antibody complex. *Febs Letters* 580:505-509.
- Neuman KC, Abbondanzieri EA, Landick R, Gelles J, and Block SM. 2003. Ubiquitous transcriptional pausing is independent of RNA polymerase backtracking. *Cell* 115:437-447.
- Neuman KC, and Block SM. 2004. Optical trapping. *Review of Scientific Instruments* 75:2787-2809.
- Neuwald AF, Aravind L, Spouge JL, and Koonin EV. 1999. AAA+: A class of chaperone-like ATPases associated with the assembly, operation, and disassembly of protein complexes. *Genome Res* 9:27-43.
- Nishiyama M, Higuchi H, and Yanagida T. 2002. Chemomechanical coupling of the forward and backward steps of single kinesin molecules. *Nat Cell Biol* 4:790-797.
- Norby JG. 1988. Coupled Assay of Na⁺,K⁺-Atpase Activity. *Methods in Enzymology* 156:116-119.
- Oberhauser AF, Marszalek PE, Carrion-Vazquez M, and Fernandez JM. 1999. Single protein misfolding events captured by atomic force microscopy. *Nature Structural Biology* 6:1025-1028.

- Ogura T, and Wilkinson AJ. 2001. AAA+ superfamily ATPases: common structure--diverse function. *Genes Cells* 6:575-597.
- Oh BK, and Apirion D. 1991. 10Sa RNA, a small stable RNA of *Escherichia coli*, is functional. *Mol Gen Genet* 229:52-56.
- Ohta K, and Ishida H. 1988. Comparison among Several Numerical-Integration Methods for Kramers-Kronig Transformation. *Applied Spectroscopy* 42:952-957.
- Ortega J, Lee HS, Maurizi MR, and Steven AC. 2002. Alternating translocation of protein substrates from both ends of ClpXP protease. *Embo J* 21:4938-4949.
- Ortega J, Lee HS, Maurizi MR, and Steven AC. 2004. ClpA and ClpX ATPases bind simultaneously to opposite ends of ClpP peptidase to form active hybrid complexes. *J Struct Biol* 146:217-226.
- Ortega J, Singh SK, Ishikawa T, Maurizi MR, and Steven AC. 2000. Visualization of substrate binding and translocation by the ATP-dependent protease, ClpXP. *Mol Cell* 6:1515-1521.
- Panchuk-Voloshina N, Haugland RP, Bishop-Stewart J, Bhargat MK, Millard PJ, Mao F, Leung WY, and Haugland RP. 1999. Alexa dyes, a series of new fluorescent dyes that yield exceptionally bright, photostable conjugates. *Journal of Histochemistry & Cytochemistry* 47:1179-1188.
- Pant K, Karpel RL, Rouzina I, and Williams MC. 2005. Salt dependent binding of T4 gene 32 protein to single and double-stranded DNA: Single molecule force spectroscopy measurements. *Journal of Molecular Biology* 349:317-330.
- Pantina JP, and Furst EM. 2004. Directed assembly and rupture mechanics of colloidal aggregates. *Langmuir* 20:3940-3946.
- Peterman EJG, Gittes F, and Schmidt CF. 2003. Laser-induced heating in optical traps. *Biophysical Journal* 84:1308-1316.
- Peterman EJG, Sosa H, and Moerner WE. 2004. Single-molecule fluorescence spectroscopy and microscopy of biomolecular motors. *Annual Review of Physical Chemistry* 55:79-96.
- Pierce DW, HomBooher N, and Vale RD. 1997. Imaging individual green fluorescent proteins. *Nature* 388:338-338.
- Pollard TD, and Borisy GG. 2003. Cellular motility driven by assembly and disassembly of actin filaments. *Cell* 112:453-465.

- Porankiewicz J, Wang J, and Clarke AK. 1999. New insights into the ATP-dependent Clp protease: *Escherichia coli* and beyond. *Mol Microbiol* 32:449-458.
- Rasnik I, McKinney SA, and Ha TJ. 2007. Nonblinking and long-lasting single molecule fluorescence imaging. *Biophysical Journal*:656a-656a.
- Raucher D, and Sheetz MP. 2000. Cell spreading and lamellipodial extension rate is regulated by membrane tension. *Journal of Cell Biology* 148:127-136.
- Ray C, Brown JR, and Akhremitchev BB. 2007. Correction of systematic errors in single-molecule force spectroscopy with polymeric tethers by atomic force microscopy. *Journal of Physical Chemistry B* 111:1963-1974.
- Reck-Peterson SL, and Vale RD. 2004. Molecular dissection of the roles of nucleotide binding and hydrolysis in dynein's AAA domains in *Saccharomyces cerevisiae*. *Proceedings of the National Academy of Sciences of the United States of America* 101:1491-1495.
- Renaud M, Belgacem MN, and Rinaudo M. 2005. Rheological behaviour of polysaccharide aqueous solutions. *Polymer* 46:12348-12358.
- Resnick A. 2003. Use of optical tweezers for colloid science. *Journal of Colloid and Interface Science* 262:55-59.
- Rief M, Gautel M, Oesterhelt F, Fernandez JM, and Gaub HE. 1997. Reversible unfolding of individual titin immunoglobulin domains by AFM. *Science* 276:1109-1112.
- Rief M, Rock RS, Mehta AD, Mooseker MS, Cheney RE, and Spudich JA. 2000. Myosin-V stepping kinetics: a molecular model for processivity. *Proc Natl Acad Sci U S A* 97:9482-9486.
- Romano G, Sacconi L, Capitanio M, and Pavone FS. 2003. Force and torque measurements using magnetic micro beads for single molecule biophysics. *Optics Communications* 215:323-331.
- Rust MJ, Bates M, and Zhuang XW. 2006. Sub-diffraction-limit imaging by stochastic optical reconstruction microscopy (STORM). *Nature Methods* 3:793-795.
- Sacconi L, Romano G, Ballerini R, Capitanio M, De Pas M, Giuntini M, Dunlap D, Finzi L, and Pavone FS. 2001. Three-dimensional magneto-optic trap for micro-object manipulation. *Optics Letters* 26:1359-1361.
- Sanders MC, Way M, Sakai J, and Matsudaira P. 1996. Characterization of the actin cross-linking properties of the scruin-calmodulin complex from the acrosomal process of *Limulus* sperm. *Journal of Biological Chemistry* 271:2651-2657.

- Sauer RT, Bolon DN, Burton BM, Burton RE, Flynn JM, Grant RA, Hersch GL, Joshi SA, Kenniston JA, Levchenko I, Neher SB, Oakes ESC, Siddiqui SM, Wah DA, and Baker TA. 2004. Sculpting the proteome with AAA+ proteases and disassembly machines. *Cell* 119:9-18.
- Schirmer EC, Glover JR, Singer MA, and Lindquist S. 1996. HSP100/Cip proteins: a common mechanism explains diverse functions. *Trends Biochem Sci* 21:289-296.
- Schmid MF, Sherman MB, Matsudaira P, and Chiu W. 2004. Structure of the acrosomal bundle. *Nature* 431:104-107.
- Schmidt J, Burchard W, and Richtering W. 2003. Rheological and rheo-optical investigation of cellulose ethers in aqueous solution. *Cellulose* 10:13-26.
- Schnitzer MJ, and Block SM. 1995. Statistical kinetics of processive enzymes. *Cold Spring Harbor Symposia on Quantitative Biology* 60:793-802.
- Schnurr B, Gittes F, MacKintosh FC, and Schmidt CF. 1997. Determining microscopic viscoelasticity in flexible and semiflexible polymer networks from thermal fluctuations. *Macromolecules* 30:7781-7792.
- Schuler B. 2005. Single-molecule fluorescence spectroscopy of protein folding. *Chemphyschem* 6:1206-1220.
- Shaevitz JW, Abbondanzieri EA, Landick R, and Block SM. 2003. Backtracking by single RNA polymerase molecules observed at near-base-pair resolution. *Nature* 426:684-687.
- Shaevitz JW, Lee JY, and Fletcher DA. 2005. Spiroplasma swim by a processive change in body helicity. *Cell* 122:941-945.
- Shin JH, Mahadevan L, So PT, and Matsudaira P. 2004. Bending stiffness of a crystalline actin bundle. *Journal of Molecular Biology* 337:255-261.
- Shin JH, Mahadevan L, Waller GS, Langsetmo K, and Matsudaira P. 2003. Stored elastic energy powers the 60- μ m extension of the *Limulus polyphemus* sperm actin bundle. *Journal of Cell Biology* 162:1183-1188.
- Shin JH, Tam BK, Brau RR, Lang MJ, Mahadevan L, and Matsudaira P. 2007. Force of an actin spring. *Biophysical Journal* 92:3729-3733.
- Shroff H, Reinhard BM, Siu M, Agarwal H, Spakowitz A, and Liphardt J. 2005. Biocompatible force sensor with optical readout and dimensions of 6 nm(3). *Nano Letters* 5:1509-1514.

- Siddiqui SM, Sauer RT, and Baker TA. 2004. Role of the processing pore of the ClpX AAA+ ATPase in the recognition and engagement of specific protein substrates. *Genes Dev* 18:369-374.
- Singh SK, Grimaud R, Hoskins JR, Wickner S, and Maurizi MR. 2000. Unfolding and internalization of proteins by the ATP-dependent proteases ClpXP and ClpAP. *Proc Natl Acad Sci U S A* 97:8898-8903.
- Singh SK, Rozycki J, Ortega J, Ishikawa T, Lo J, Steven AC, and Maurizi MR. 2001. Functional domains of the ClpA and ClpX molecular chaperones identified by limited proteolysis and deletion analysis. *J Biol Chem* 276:29420-29429.
- Smith DE, Tans SJ, Smith SB, Grimes S, Anderson DL, and Bustamante C. 2001. The bacteriophage phi 29 portal motor can package DNA against a large internal force. *Nature* 413:748-752.
- Smith SB, Cui YJ, and Bustamante C. 1996. Overstretching B-DNA: The elastic response of individual double-stranded and single-stranded DNA molecules. *Science* 271:795-799.
- So PTC, Dong CY, Masters BR, and Berland KM. 2000. Two-photon excitation fluorescence microscopy. *Annual Review of Biomedical Engineering* 2:399-429.
- Squires C, and Squires CL. 1992. The Clp proteins: proteolysis regulators or molecular chaperones? *J Bacteriol* 174:1081-1085.
- Starrs L, and Bartlett P. 2003. One- and two-point micro-rheology of viscoelastic media. *Journal of Physics-Condensed Matter* 15:S251-S256.
- Stone MD, Mihalusova M, O'Connor CM, Prathapam R, Collins K, and Zhuang XW. 2007. Stepwise protein-mediated RNA folding directs assembly of telomerase ribonucleoprotein. *Nature* 446:458-461.
- Su J, Jiang X, Welsch R, Whistlesides GM, and So PTC. 2007. Geometric Confinement Influences Cellular Mechanical Properties I - Adhesion Area Dependence. *Molecular and Cellular Biomechanics* 4:87-104.
- Svoboda K, and Block SM. 1994a. Biological applications of optical forces. *Annu Rev Biophys Biomol Struct* 23:247-285.
- Svoboda K, and Block SM. 1994b. Optical Trapping of Metallic Rayleigh Particles. *Optics Letters* 19:930-932.

- Svoboda K, Mitra PP, and Block SM. 1994. Fluctuation analysis of motor protein movement and single enzyme kinetics. *Proc Natl Acad Sci U S A* 91:11782-11786.
- Tarsa PB, Brau RR, Barch M, Ferrer JM, Freyzon Y, Matsudaira P, and Lang MJ. 2007. Detecting force-induced molecular transitions with fluorescence resonant energy transfer. *Angewandte Chemie-International Edition* 46:1999-2001.
- Tilney LG. 1975. Actin-Filaments in Acrosomal Reaction of Limulus Sperm - Motion Generated by Alterations in Packing of Filaments. *Journal of Cell Biology* 64:289-310.
- Tirado MM, and Garcíadelatorre J. 1979. Translational Friction Coefficients of Rigid, Symmetric Top Macromolecules - Application to Circular-Cylinders. *Journal of Chemical Physics* 71:2581-2587.
- Tokunaga M, Kitamura K, Saito K, Iwane AH, and Yanagida T. 1997. Single molecule imaging of fluorophores and enzymatic reactions achieved by objective-type total internal reflection fluorescence microscopy. *Biochemical and Biophysical Research Communications* 235:47-53.
- Tolic-Norrelykke SF, Engh AM, Landick R, and Gelles J. 2004. Diversity in the rates of transcript elongation by single RNA polymerase molecules. *J Biol Chem* 279:3292-3299.
- Tu GF, Reid GE, Zhang JG, Moritz RL, and Simpson RJ. 1995. C-terminal extension of truncated recombinant proteins in *Escherichia coli* with a 10Sa RNA decapeptide. *J Biol Chem* 270:9322-9326.
- Tzima E, del Pozo MA, Shattil SJ, Chien S, and Schwartz MA. 2001. Activation of integrins in endothelial cells by fluid shear stress mediates Rho-dependent cytoskeletal alignment. *Embo Journal* 20:4639-4647.
- Vale RD. 2000. AAA proteins. Lords of the ring. *J Cell Biol* 150:F13-19.
- Vale RD, Funatsu T, Pierce DW, Romberg L, Harada Y, and Yanagida T. 1996. Direct observation of single kinesin molecules moving along microtubules. *Nature* 380:451-453.
- Vale RD, and Milligan RA. 2000. The way things move: Looking under the hood of molecular motor proteins. *Science* 288:88-95.
- Valentine MT, Dewalt LE, and OuYang HD. 1996. Forces on a colloidal particle in a polymer solution: A study using optical tweezers. *Journal of Physics-Condensed Matter* 8:9477-9482.

- Valeur B. 2002. *Molecular fluorescence : principles and applications*. Wiley-VCH, Weinheim ; New York. xiv, 387 p.
- van Dijk MA, Kapitein LC, van Mameren J, Schmidt CF, and Peterman EJG. 2004. Combining optical trapping and single-molecule fluorescence spectroscopy: Enhanced photobleaching of fluorophores. *Journal of Physical Chemistry B* 108:6479-6484.
- Veigel C, Schmitz S, Wang F, and Sellers JR. 2005. Load-dependent kinetics of myosin-V can explain its high processivity. *Nature Cell Biology* 7:861-869.
- Visscher K, Gross SP, and Block SM. 1996. Construction of multiple-beam optical traps with nanometer-resolution position sensing. *IEEE Journal of Selected Topics in Quantum Electronics* 2:1066-1076.
- Visscher K, Schnitzer MJ, and Block SM. 1999. Single kinesin molecules studied with a molecular force clamp. *Nature* 400:184-189.
- Vladescu ID, McCauley MJ, Nunez ME, Rouzina I, and Williams MC. 2007. Quantifying force-dependent and zero-force DNA intercalation by single-molecule stretching. *Nature Methods* 4:517-522.
- Waigh TA. 2005. Microrheology of complex fluids. *Reports on Progress in Physics* 68:685-742.
- Walker JE, Saraste M, Runswick MJ, and Gay NJ. 1982. Distantly related sequences in the alpha- and beta-subunits of ATP synthase, myosin, kinases and other ATP-requiring enzymes and a common nucleotide binding fold. *Embo J* 1:945-951.
- Wallace MI, Molloy JE, and Trentham DR. 2003. Combined single-molecule force and fluorescence measurements for biology. *J Biol* 2:4.
- Wang MD, Yin H, Landick R, Gelles J, and Block SM. 1997. Stretching DNA with optical tweezers. *Biophysical Journal* 72:1335-1346.
- Wang YX, Botvinick EL, Zhao YH, Berns MW, Usami S, Tsien RY, and Chien S. 2005. Visualizing the mechanical activation of Src. *Nature* 434:1040-1045.
- Ward IM, and Sweeney J. 2004. *An introduction to the mechanical properties of solid polymers*. Wiley, Hoboken, NJ. x, 382.
- Warshaw DM, Kennedy GG, Work SS, Krementsova EB, Beck S, and Trybus KM. 2005. Differential Labeling of myosin V heads with quantum dots allows direct visualization of hand-over-hand processivity. *Biophysical Journal* 88:L30-L32.

- Weibezahn J, Bukau B, and Mogk A. 2004. Unscrambling an egg: protein disaggregation by AAA+ proteins. *Microb Cell Fact* 3:1.
- Weiss S. 1999. Fluorescence spectroscopy of single biomolecules. *Science* 283:1676-1683.
- Weitzman JB. 2003. A marriage of techniques. *J Biol* 2:2.
- Wennmalm S, and Rigler R. 1999. On death numbers and survival times of single dye molecules. *Journal of Physical Chemistry B* 103:2516-2519.
- Whaley SR, English DS, Hu EL, Barbara PF, and Belcher AM. 2000. Selection of peptides with semiconductor binding specificity for directed nanocrystal assembly. *Nature* 405:665-668.
- Wojtkowiak D, Georgopoulos C, and Zylicz M. 1993. Isolation and characterization of ClpX, a new ATP-dependent specificity component of the Clp protease of *Escherichia coli*. *J Biol Chem* 268:22609-22617.
- Woo KM, Chung WJ, Ha DB, Goldberg AL, and Chung CH. 1989. Protease Ti from *Escherichia coli* requires ATP hydrolysis for protein breakdown but not for hydrolysis of small peptides. *J Biol Chem* 264:2088-2091.
- Woodside MT, Behnke-Parks WM, Larizadeh K, Travers K, Herschlag D, and Block SM. 2006. Nanomechanical measurements of the sequence-dependent folding landscapes of single nucleic acid hairpins. *Proceedings of the National Academy of Sciences of the United States of America* 103:6190-6195.
- Yamada S, Wirtz D, and Kuo SC. 2000. Mechanics of living cells measured by laser tracking microrheology. *Biophysical Journal* 78:1736-1747.
- Yamaguchi N, Chae BS, Zhang L, Kiick KL, and Furst EM. 2005. Rheological characterization of polysaccharide-poly(ethylene glycol) star copolymer hydrogels. *Biomacromolecules* 6:1931-1940.
- Yildiz A, Forkey JN, McKinney SA, Ha T, Goldman YE, and Selvin PR. 2003. Myosin V walks hand-over-hand: Single fluorophore imaging with 1.5-nm localization. *Science* 300:2061-2065.
- Yildiz A, Park H, Safer D, Yang ZH, Chen LQ, Selvin PR, and Sweeney HL. 2004. Myosin VI steps via a hand-over-hand mechanism with its lever arm undergoing fluctuations when attached to actin. *Journal of Biological Chemistry* 279:37223-37226.

Zheng PJ, Li L, Hu X, and Zhao XY. 2004. Sol-gel transition of methylcellulose in phosphate buffer saline solutions. *Journal of Polymer Science Part B-Polymer Physics* 42:1849-1860.

Zhuang XW, Bartley LE, Babcock HP, Russell R, Ha TJ, Herschlag D, and Chu S. 2000. A single-molecule study of RNA catalysis and folding. *Science* 288:2048-+.